

Efficient Geometric Markov Chain Monte Carlo for Nonlinear Bayesian Inversion Enabled by Derivative-Informed Neural Operators

Lianghao Cao^{1a,*}, Thomas O’Leary-Roseberry^b, Omar Ghattas^{b,c}

^a*Department of Computing and Mathematical Sciences, California Institute of Technology, 1200 E. California Blvd., MC 305-16, Pasadena, CA 91125, USA*

^b*Oden Institute for Computational Engineering and Sciences, The University of Texas at Austin, 201 E. 24th St., C0200, Austin, TX 78712, USA.*

^c*Walker Department of Mechanical Engineering, The University of Texas at Austin, 204 E. Dean Keaton St., Austin, TX 78712, USA.*

Abstract

We propose an operator learning approach to accelerate geometric Markov chain Monte Carlo (MCMC) for solving infinite-dimensional nonlinear Bayesian inverse problems. While geometric MCMC employs high-quality proposals that adapt to posterior local geometry, it requires computing local gradient and Hessian information of the log-likelihood, incurring a high cost when the parameter-to-observable (PtO) map is defined through expensive model simulations. We consider a delayed-acceptance geometric MCMC method driven by a neural operator surrogate of the PtO map, where the proposal is designed to exploit fast surrogate approximations of the log-likelihood and, simultaneously, its gradient and Hessian. To achieve a substantial speedup, the surrogate needs to be accurate in predicting both the observable and its parametric derivative (the derivative of the observable with respect to the parameter). Training such a surrogate via conventional operator learning using input-output samples often demands a prohibitively large number of model simulations. In this work, we present an extension of derivative-informed operator learning [O’Leary-Roseberry et al., *J. Comput. Phys.*, 496 (2024)] using input–output–derivative training samples. Such a learning method leads to derivative-informed neural operator (DINO) surrogates that accurately predict the observable and its parametric derivative at a significantly lower training cost than the conventional method. Cost and error analysis for reduced basis DINO surrogates are provided. Numerical studies on PDE-constrained Bayesian inversion demonstrate that DINO-driven MCMC generates effective posterior samples 3–9 times faster than geometric MCMC and 60–97 times faster than prior geometry-based MCMC. Furthermore, the training cost of DINO surrogates breaks even after collecting merely 10–25 effective posterior samples compared to geometric MCMC.

Contents

1	Introduction	3
1.1	Quality–cost trade-off in Markov chain Monte Carlo for Bayesian inversion	3
1.2	Accelerate geometric MCMC using derivative-informed neural operator	4
1.3	Literature review	4
1.3.1	Neural operator surrogate	5
1.3.2	MCMC for Bayesian inversion	5

¹The majority of this work was completed when the author was at Oden Institute for Computational Engineering and Sciences, The University of Texas at Austin.

*Corresponding authors

Email addresses: lianghao@caltech.edu (Lianghao Cao), tom.olearyroseberry@utexas.edu (Thomas O’Leary-Roseberry), omar@oden.utexas.edu (Omar Ghattas)

1.4	Contributions	6
1.5	Layout of the paper	6
2	Preliminaries: Nonlinear Bayesian inversion and MCMC	7
2.1	Notations	7
2.2	Nonlinear Bayesian inverse problem	7
2.3	Cameron–Martin space and differentiability	8
2.4	Local Gaussian approximation of the posterior using parametric derivative	9
2.5	The Metropolis–Hasting algorithm	9
2.6	Dimension-independent MCMC	10
2.7	Geometric MCMC	11
2.8	Delayed acceptance MCMC	12
3	Operator learning in H_μ^1 Sobolev space with Gaussian measure	13
3.1	Operator learning in L_μ^2 Bochner space	13
3.2	Operator learning in H_μ^1 Sobolev space with Gaussian measure	14
3.3	Matrix representation of derivative	15
4	Reduced basis derivative-informed neural operator	15
4.1	A brief recap	17
4.2	Derivative and prior-based reduced bases	17
4.3	Training sample generation and cost analysis for PDE models	18
4.4	Neural operator approximation error	19
5	Geometric MCMC via reduced basis neural operator	22
5.1	Surrogate approximation	22
5.2	Surrogate prediction of posterior local geometry	22
5.3	Sampling from the surrogate mMALA proposal	23
5.4	Evaluating acceptance probabilities	24
6	Numerical examples: Baseline, chain diagnostics, efficiency metrics, and software	25
6.1	Baseline and reference MCMC methods	26
6.2	Markov chain diagnostics	27
6.2.1	Wasserstein multivariate potential scale reduction factor	27
6.2.2	Effective sample size percentage distribution	27
6.3	Comparing efficiency of MCMC methods	28
6.3.1	Effective sampling speedup	28
6.3.2	Total effective sampling speedup	28
6.4	Software	28
7	Numerical example: Coefficient inversion for nonlinear diffusion–reaction PDE	29
7.1	The prior distribution	29
7.2	The parameter-to-observable map	29
7.3	Bayesian inversion settings	30
7.4	Neural operator surrogates	30
7.5	MCMC Results	32
7.5.1	The baseline MCMC methods	32
7.5.2	Geometric MCMC with operator surrogate proposal	33
7.5.3	Delayed acceptance geometric MCMC with operator surrogate proposal	34

8 Numerical example: Hyperelastic material property discovery	36
8.1 The neo-Hookean model for hyperelastic material deformation	36
8.2 The prior distribution	37
8.3 The parameter-to-observable map	38
8.4 Bayesian inversion settings	38
8.5 Neural operator surrogate	39
8.6 MCMC results	40
8.6.1 The baseline MCMC methods	40
8.6.2 Delayed acceptance geometric MCMC with operator surrogate proposal	41
9 Conclusion	43
Appendix A Stochastic Gâteaux differentiability	46
Appendix B The gradient and the Gauss–Newton Hessian of the data misfit	47
Appendix C Bounding constant and proofs of Propositions 4.1 and 4.2	47
Appendix D Proofs of Lemma 5.1 and Proposition 5.2	50
Appendix E Step size tuning and chain initialization	51
Appendix F Supplementary materials for the numerical examples	51

1. Introduction

1.1. Quality–cost trade-off in Markov chain Monte Carlo for Bayesian inversion

Computational models of continuum physical systems arising from scientific and engineering applications, such as those governed by partial differential equations (PDEs), often contain unspecified or uncertain parameters in the form of spatially and temporally varying functions. Given sparse and noisy observations of the system, infinite-dimensional inverse problems aim to infer the parameter at which model-predicted observations (i.e., the *observable*) best explain the observed data. A Bayesian formulation of the inverse problem is often adopted to rigorously accommodate various uncertainties in the system, where solutions are represented as probability distributions of parameters (i.e., the *posterior*). Bayesian inverse problems are of enormous practical importance due to their ability to enhance the predictability and reliability of computational models for better design, control, and more general risk-aware decision-making [1–5].

Markov chain Monte Carlo (MCMC) methods based on the Metropolis–Hastings (MH) algorithm [6, 7] construct Markov chains whose stationary distributions are the Bayesian posterior [8, 9]. These methods are often regarded as the gold standard for rigorous solutions of Bayesian inversion due to their algorithmic simplicity and posterior sampling consistency. A fundamental challenge in designing an efficient MCMC method for nonlinear Bayesian inversion is to optimize the balance between the quality of generated Markov chains for posterior sampling and the associated computational cost. The quality of a Markov chain can be quantified by its effective sample size and mixing time. The computational cost consists of proposal sampling and acceptance probability computation at each chain position; the latter often involves evaluating the nonlinear parameter-to-observable map (PtO) map via expensive model simulation.

To generate high-quality Markov chains for posterior sampling, an MCMC method must be capable of agile transversal of the posterior landscape. This often requires intelligent MCMC proposal designs using either (i) the local curvature of the posterior landscape, or (ii) a surrogate PtO map. These two approaches represent two major but mostly separated developments of MCMC method for infinite-dimensional Bayesian inversion: (i) *geometric MCMC* methods with proposals that adapt to posterior local geometry [10–16] and (ii) *delayed-acceptance (DA) MCMC* methods with proposals utilizing MCMC methods targeting the surrogate posterior [17–19]. However, high quality comes with a high cost. For geometric MCMC, extracting

posterior local geometry requires computing the derivative of the observable with respect to the parameter (i.e., the *parametric derivative* of the PtO map) through repetitively solving linear sensitivity or adjoint problems of the computational model at each chain position. In practice, the accumulated cost of these linear solves often overwhelms their benefit. For DA MCMC, constructing a data-driven surrogate of the nonlinear PtO map with infinite-dimensional input space may necessitate a large number of offline (prior to MCMC) model simulations to achieve a meaningful online (during MCMC) acceleration.

1.2. Accelerate geometric MCMC using derivative-informed neural operator

We consider using neural operator surrogates of the PtO map to design MCMC methods based on the following observation: an ideal quality–cost trade-off in an MCMC method can be achieved by a surrogate PtO map that is fast and accurate in both parameter-to-observable predictions (for DA MCMC) and parameter-to-parametric derivative predictions (for geometric MCMC). Neural operators [20, 21], i.e., nonlinear mapping between function spaces constructed using neural networks, have the potential to provide a good approximation of both the PtO map and its parametric derivative when the parameter space has infinite dimensions. Notably, the surrogate parametric derivative can be extracted through automatic differentiation at a low cost. On the other hand, conventional operator learning using input–output samples generated via model simulations does not enforce error control in approximating the derivative of the output with respect to the input; thus, the training cost for constructing an operator surrogate of large-scale model simulations that accurately predicts the derivative across the input space can be prohibitively high. As a result, neural operator surrogates often struggle to achieve meaningful speedups in gradient-based model-constrained optimization in high or infinite dimensions, where the surrogate-predicted gradient of the objective function substitutes the model-predicted gradient estimated via adjoint solves; see, e.g., [22, Section 4.2.2]. Similarly, we expect the neural operator surrogate constructed via conventional operator learning to struggle in accelerating geometric MCMC.

In this work, we propose an efficient geometric MCMC method leveraging derivative-informed neural operator (DINO) [23]. Unlike conventional operator learning with error control in input-to-output predictions, derivative-informed operator learning enforces error control in both input-to-output and input-to-derivative predictions. During the offline phase, we generate parameter–observable–parametric derivative samples to train a DINO surrogate of the PtO map. The DINO surrogate can achieve significantly higher accuracy in both the observable and its parametric derivative at a similar training cost as conventional training using parameter–observable samples. During the online phase, we deploy the trained DINO surrogate in a delayed-acceptance geometric MCMC method, where both the DINO surrogate prediction of posterior local geometry and the DINO surrogate PtO map contribute to generating high-quality Markov chains for posterior sampling at a considerably lower cost than conventional geometric MCMC methods.

We provide rigorous comparisons of our method with various baseline MCMC methods for solving challenging Bayesian inverse problems, such as coefficient inversion in nonlinear diffusion–reaction PDE and hyperelastic material property discovery. Our numerical results show that

1. DINO-driven MCMC generates effective posterior samples 60–97 times faster than MCMC based on prior geometry (preconditioned Crank–Nicolson [24]), 3–9 times faster than geometric MCMC, and 18–40 times faster than using a conventionally trained neural operator surrogate. When accounting for training sample generation cost, the training cost of DINO surrogates breaks even after collecting merely 10–25 effective posterior samples compared to geometric MCMC.
2. Derivative-informed operator learning achieves similar generalization accuracy in predicting the observable and its parametric derivative with at least 16–25 times less training sample generation cost than the conventional operator learning method. In our numerical examples of nonlinear diffusion–reaction, we observe an estimated 166 times difference in training sample generation cost between the two operator learning methods for reaching a meaningful speedup of geometric MCMC.

1.3. Literature review

In this subsection, we cover literature relevant to our work on neural operator surrogates and MCMC for Bayesian inversion.

1.3.1. Neural operator surrogate

Constructing neural operator surrogates involves (i) using neural networks to design an architecture that maps between function spaces and allows for sufficient expressivity, and (ii) approximating a target nonlinear mapping by training the neural networks via supervised or semi-supervised learning [20, 21]. The key feature of a neural operator is that its architecture and learning scheme are independent of any particular discretization of the input and output space. We utilize the term neural operator in the context that at least one of the input and output is a function space, as it necessitates a neural operator architecture and learning scheme. In this subsection, we briefly overview concepts related to neural operator surrogates relevant to our work.

1. **Neural operator architectures:** The architecture more relevant to this work is reduced basis neural operators that use neural networks to learn the reduced nonlinear mapping between coefficients of input and output reduced bases [25–29]. Choices of reduced bases include but are not limited to (i) proper orthogonal decomposition (POD-NN) or principal component analysis (PCA-Net)[25, 27], (ii) active subspace or derivative-informed subspace (DIP-Net)[28, 29], (iii) learned neural network representation of output reduced bases (DeepONet)) [30], and (iv) variational autoencoders (VAE) [31]. Other architectures include the Fourier neural operator (FNO) [32] and its variants [33, 34], the graph neural operator [35], and the multipole graph neural operator [36]. See empirical comparisons of neural operator architectures for learning solution operators of PDEs in [37, 38]
2. **Operator learning objective:** The operator learning objective is typically defined as approximation error control in the Bochner norm of nonlinear mappings between function spaces [20]. It can be interpreted as an expected risk minimization problem. When the loss is approximated using samples, it leads to an empirical risk minimization problem, which is covered in [Section 3.1](#). There are efforts dedicated to enhancing the loss function using spatial quarries of PDE residual, notably for FNO (PINO) [39] and DeepONet (PI-DeepONet) [40] architectures. DINO is the focus of this work and is at its core a design of operator learning objective that enforces approximation error control in high-dimensional Sobolev spaces of nonlinear mappings [23]. Such an objective design leads to neural operator surrogates that are accurate in not only the input-to-output mapping but also input-to-derivative mapping. In several recent works, DINOs have successfully been deployed in applications such as optimization under uncertainty [22] and optimal experimental design [41], demonstrating notable improvements compared to conventional operator learning methods.
3. **Parametric derivative vs. spatial derivative:** We emphasize the important distinction between parametric derivative and spatial derivative. Evaluating the parametric derivative requires differentiating the nonlinear mappings from a parameter to the model prediction. It often requires repetitively solving the forward sensitivity or adjoint problem of the model with different right-hand side vectors [4, 23]. Controlling approximation error in the parametric derivative is highly nontrivial in the operator learning setting. On the other hand, controlling approximation error in the spatial derivatives of spatially varying output functions can be straightforwardly implemented using a Sobolev norm over the spatial domain (e.g., $H^1(\Omega)$) for output error measure.

1.3.2. MCMC for Bayesian inversion

We briefly overview three aspects of MCMC methods for infinite-dimensional Bayesian inversion relevant to this work. Technical descriptions of some of these methods can be found in [Section 2](#).

1. **Scalability:** During computation, the posterior is approximated on a discretized finite-dimensional subspace of the parameter function space via, e.g., the Galerkin method. Many popular MCMC methods, such as random walk Metropolis, targeting the discretized posterior suffer from deteriorated sampling performance as the discretization dimension increases. A class of *dimension-independent MCMC methods* has emerged [12, 24, 42–45] that seek first to design MCMC methods that are well-posed on function spaces and then discretize for computation.

2. **Exploiting posterior geometry:** A class of *geometric MCMC* methods gained attention in the last decade due to their information geometric approaches to proposal design [10–13, 15, 16, 46–48]. Relevant developments in this area include but are not limited to (i) proposals utilizing fixed or averaged posterior geometry, such as likelihood-informed subspace [43], active subspace [49], variational and Laplace approximation [45–47, 50], and adaptive dimension reduction [16]; (ii) proposals that adapt to posterior local geometry, such as Riemannian manifold MCMC utilizing the parametric derivative and Hessian of the PtO map [10, 13], stochastic Newton MCMC utilizing a parametric derivative and low-rank approximation of parametric Hessian [11], Gaussian process emulation of geometric quantities [14], and dimension-independent geometric MCMC utilizing parametric derivative (i.e., using a simplified manifold)[12, 15, 16]. Other notable developments include proposal designs using local likelihood approximations [51] and transport maps constructed by low-fidelity simulations [52].
3. **Multifidelity acceleration:** Cheap-to-evaluate low-fidelity model simulations can help alleviate the cost of MCMC due to model simulations via *delayed acceptance (DA) MCMC* [17–19]. The key idea is to use a proposal given by the Markov chain transition rule of an MCMC method targeting the surrogate-approximated posterior, leading to a two-stage [17] procedure for a single surrogate model or multi-stage [19] procedure for multiple surrogate models. *Multilevel MCMC* methods [53–56] leverages a hierarchy of the same model with different discretization to reduce the overall computational cost of MCMC.

1.4. Contributions

The main contributions of this work are summarized as follows.

1. We propose an efficient MCMC method ([Algorithm 1](#)) for infinite-dimensional nonlinear Bayesian inversion via synergizing reduced basis DINO surrogate [23], DA MCMC [17], and dimension-independent geometric MCMC [15]. The method employs a proposal that adapts to DINO-predicted posterior local geometry within a delayed acceptance procedure. Compared to conventional geometric MCMC, our method leads to significant cost reduction due to (i) no online forward or adjoint sensitivity solves, (ii) fewer online model quarries necessary for posterior consistency, and (iii) fewer online instances of prior sampling. At the same time, our numerical examples show that the method produces high-quality Markov chains typical for a geometric MCMC method, leading to substantial speedups in posterior sample generation.
2. We present an extended formulation of the derivative-informed operator learning introduced in [23]. In particular, we establish suitable function space settings, i.e., the H_μ^1 Sobolev space with Gaussian measure ([Section 3.2](#)), for derivative-informed operator learning that can be extended beyond the confines of inverse problems and particular choices of neural operator architecture. We additionally provide (i) a cost analysis for training data generation based on PDE models ([Section 4.3](#)) and (ii) theoretical results on the neural operator approximation error of reduced basis DINO surrogate based on a Poincaré inequality for nonlinear mappings between function spaces ([Section 4.4](#)).
3. We provide rigorous numerical studies of our methods and other baseline MCMC methods using two infinite-dimensional Bayesian inverse problems: coefficient inverse for nonlinear diffusion-reaction PDE and hyperelastic material property discovery. The implementation and the data are available for sharing upon request³.

1.5. Layout of the paper

The layout of the paper is as follows. In [Section 2](#), we introduce concepts in nonlinear Bayesian inversion and MCMC, including parametric derivative, posterior local approximation, dimension-independent

³Public release of code and data is contingent on acceptance for journal publication.

geometric MCMC, and delayed acceptance MCMC. In Section 3, we present a derivative-informed operator learning method with error control in the H_μ^1 Sobolev space with Gaussian measure. In Section 4, we formulate derivative-informed training of reduced basis DINO, discuss its computational cost, and provide error analysis for different choices of reduced bases. In Section 5, we detail the process of generating proposals that adapt to posterior local geometry with a trained neural operator surrogate and the resulting MCMC acceptance probability computation. In Section 6, we explain the setup for our numerical examples, including an extensive list of baseline and reference MCMC methods, Markov chain diagnostics, efficiency metrics, and software. In Sections 7 and 8, we showcase and analyze results for the numerical examples on coefficient inversion in nonlinear diffusion–reaction PDE and hyperelastic material property discovery.

2. Preliminaries: Nonlinear Bayesian inversion and MCMC

2.1. Notations

- $\langle \cdot, \cdot \rangle_{\mathcal{X}}$ denotes the inner-product on a Hilbert space \mathcal{X} and $\|\cdot\|_{\mathcal{X}}$ denotes the inner-product induced norm. The subscript is omitted when \mathcal{X} is an Euclidean space.
- $\langle x_1, x_2 \rangle_{\mathcal{T}} := \langle \mathcal{T}x_1, x_2 \rangle_{\mathcal{X}}$ and $\|x\|_{\mathcal{T}} := \sqrt{\langle \mathcal{T}x, x \rangle_{\mathcal{X}}}$ denote the inner-product and norm weighted by a positive and self-adjoint operator $\mathcal{T} : \mathcal{X} \rightarrow \mathcal{X}$.
- $B(\mathcal{X}_1, \mathcal{X}_2)$ denotes the Banach space of bounded and linear operators between two Hilbert spaces \mathcal{X}_1 and \mathcal{X}_2 equipped with the operator norm. We use $B(\mathcal{X})$ for $B(\mathcal{X}, \mathcal{X})$.
- $HS(\mathcal{X}_1, \mathcal{X}_2) \subseteq B(\mathcal{X}_1, \mathcal{X}_2)$ denotes the Banach space of Hilbert–Schmidt operators. $\|\cdot\|_{HS}$ denotes the Hilbert–Schmidt norm. We use $HS(\mathcal{X})$ for $HS(\mathcal{X}, \mathcal{X})$.
- $B_1^+(\mathcal{X}) \subseteq HS(\mathcal{X})$ denotes the set of positive, self-adjoint, and trace class operators on a Hilbert space \mathcal{X} .
- $(\mathcal{X}, \mathcal{B}(\mathcal{X}))$ denotes a measurable space with $\mathcal{B}(\cdot)$ being the Borel σ -algebra generated by open sets. $\mathcal{P}(\mathcal{X})$ denotes the set of probability measures defined on $(\mathcal{X}, \mathcal{B}(\mathcal{X}))$.
- $\nu(dx)$ denotes a measure on $(\mathcal{X}, \mathcal{B}(\mathcal{X}))$ in the sense that $\nu(\mathcal{A}) = \int_{\mathcal{A}} \nu(dx)$, where $\mathcal{A} \in \mathcal{B}(\mathcal{X})$ and x is a dummy variable for integration. The expression $\nu_1(dx)/\nu_2(dx)$ denotes the Radon–Nikodym derivative between two measures $\nu_1, \nu_2 \in \mathcal{P}(\mathcal{X})$ at $x \in \mathcal{X}$.
- We use capital letters to denote random variables, i.e., $X \sim \nu \in \mathcal{P}(\mathcal{X})$. Both matrices and random vectors are denoted using bold and capitalized letters; they can be distinguished based on the context.

2.2. Nonlinear Bayesian inverse problem

Let \mathcal{M} be a separable Hilbert space. We refer to \mathcal{M} as the *parameter space*. Let $\mathcal{G} : \mathcal{M} \rightarrow \mathbb{R}^{d_y}$ be a nonlinear *parameter-to-observable (PtO) map* that represents model predictions of the *observables*. We refer to the \mathbb{R}^{d_y} , $d_y \in \mathbb{N}$, as the *observable space*. Let $\mathbf{y} \in \mathbb{R}^{d_y}$ denote a set of observed data. We assume that \mathbf{y} is given by the model-predicted observable at unknown parameter $m \in \mathcal{M}$ corrupted with unknown additive noise $\mathbf{n} \in \mathbb{R}^{d_y}$:

$$\mathbf{y} = \mathcal{G}(m) + \mathbf{n}, \quad \mathbf{n} \stackrel{\text{i.i.d.}}{\sim} \pi_n, \quad (\text{Data model}) \quad (1)$$

where $\pi_n \in \mathcal{P}(\mathbb{R}^{d_y})$ is the noise probability density⁴. The inverse problem is to recover m given data \mathbf{y} .

Under the Bayesian approach to inverse problems, we assume prior knowledge of the parameter represented by a *prior distribution* $\mu \in \mathcal{P}(\mathcal{M})$. We are interested in characterizing the *posterior distributions*

⁴For finite-dimensional distributions, we assume their probability densities exist and do not distinguish between densities and measures.

$\mu^y \in \mathcal{P}(\mathcal{M})$ representing our updated knowledge of the parameter after acquiring data y . The posterior is defined by Bayes' rule using a Radon–Nikodym (RN) derivative:

$$\frac{\mu^y(dm)}{\mu(dm)} \propto \pi_n(y - \mathcal{G}(m)). \quad (\text{Bayes' rule}) \quad (2)$$

We adopt the following assumptions, often employed for infinite-dimensional Bayesian inverse problems, e.g., when \mathcal{M} consists of spatially or temporally varying functions.

Assumption 1 (Gaussian noise). *The noise distribution is given by $\pi_n := \mathcal{N}(\mathbf{0}, \mathbf{C}_n)$ with covariance matrix $\mathbf{C}_n \in B_1^+(\mathbb{R}^{d_y})$. This leads to the following form of the Bayes' rule:*

$$\frac{\mu^y(dm)}{\mu(dm)} := \frac{1}{z(y)} \exp(-\Phi^y(m)), \quad \Phi^y(m) := \frac{1}{2} \|y - \mathcal{G}(m)\|_{\mathbf{C}_n^{-1}}^2 \quad \mu\text{-a.e.}, \quad (3)$$

where $\Phi^y : \mathcal{M} \rightarrow \mathbb{R}$ is the data misfit and $z(y) := \mathbb{E}_{M \sim \mu} [\Phi^y(M)]$ is the normalization constant.

Assumption 2 (Gaussian prior). *The prior distribution is given by $\mu := \mathcal{N}(\mathbf{0}, \mathcal{C}_{\text{pr}})$ with covariance operator $\mathcal{C}_{\text{pr}} \in B_1^+(\mathcal{M})$.*

Assumption 3 (Well-posedness [57, Corollary 4.4]). *The PtO map \mathcal{G} is μ -a.e. well-defined, sufficiently bounded, and locally Lipschitz continuous, which implies that the Bayesian inversion is well-posed.*

2.3. Cameron–Martin space and differentiability

We consider two Hilbert spaces with prior and noise covariance inverse-weighted inner products on the observable and parameter space. These spaces are known as the Cameron–Martin (CM) space of μ and π_n .

$$\begin{aligned} \text{Parameter CM space } \mathcal{H}_\mu : & \quad \left(\left\{ m \in \mathcal{M} \mid \|m\|_{\mathcal{C}_{\text{pr}}^{-1}} < \infty \right\}, \langle \cdot, \cdot \rangle_{\mathcal{C}_{\text{pr}}^{-1}} \right), \\ \text{Observable CM space } \mathcal{Y} : & \quad \left(\mathbb{R}^{d_y}, \langle \cdot, \cdot \rangle_{\mathbf{C}_n^{-1}} \right). \end{aligned}$$

We have the continuous embedding $\mathcal{H}_\mu \hookrightarrow \mathcal{M}$, i.e., there exists $c > 0$ such that $\|m\|_{\mathcal{M}} \leq c \|m\|_{\mathcal{C}_{\text{pr}}^{-1}}$ for all $m \in \mathcal{H}_\mu$. However, the converse is not true when \mathcal{M} has infinite dimensions, e.g., $\|M\|_{\mathcal{C}_{\text{pr}}^{-1}} = \infty$ and $\|M\|_{\mathcal{M}} < \infty$ a.s. for $M \sim \mu$. The observable CM space \mathcal{Y} is isomorphic to \mathbb{R}^{d_y} under the identity map, yet the weighted inner product of \mathcal{Y} is often preferred in the context of inverse problems as it reflects our confidence in the observed data.

The CM space plays a major role in understanding the equivalence of measures due to the linear transformations of infinite-dimensional Gaussian random functions, and it will be applied extensively in this work. We refer to [58, Section 2.7] and [57, 59] for detailed references on Gaussian measures and the Cameron–Martin space.

In addition to [Assumptions 1](#) to [3](#), we assume the directional differentiability of the PtO map along the parameter CM space \mathcal{H}_μ .

Assumption 4 (stochastic Gâteaux differentiability [59, 5.2.3]). *There exists a mapping $D_{\mathcal{H}_\mu} \mathcal{G} : \mathcal{M} \rightarrow \text{HS}(\mathcal{H}_\mu, \mathcal{Y})$ such that for any $\delta m \in \mathcal{H}_\mu$,*

$$\lim_{t \rightarrow 0} \|t^{-1} (\mathcal{G}(m + t\delta m) - \mathcal{G}(m)) - D_{\mathcal{H}_\mu} \mathcal{G}(m)\delta m\|_{\mathbf{C}_n^{-1}} = 0 \quad \mu\text{-a.e.}$$

The mapping $D_{\mathcal{H}_\mu} \mathcal{G}$ is called the stochastic derivative of \mathcal{G} .

It is worth mentioning that [Assumption 4](#) is weaker than the typical Gâteaux differentiability assumption that requires directional differentiability along the whole parameter space \mathcal{M} .

Definition 1 (μ -a.e. Gâteaux differentiability). *There exists a mapping $D\mathcal{G} : \mathcal{M} \rightarrow \text{HS}(\mathcal{M}, \mathbb{R}^{d_y})$ such that for any $\delta m \in \mathcal{M}$,*

$$\lim_{t \rightarrow 0} \|t^{-1}(\mathcal{G}(m + t\delta m) - \mathcal{G}(m)) - D\mathcal{G}(m)\delta m\| = 0 \quad \mu\text{-a.e.}$$

The mapping $D\mathcal{G}$ is called the Gâteaux derivative of \mathcal{G} .

First, notice that if the Gâteaux derivative of \mathcal{G} exists, then stochastic derivative exists and we have $D\mathcal{G}(m)|_{\mathcal{H}_\mu} = D_{\mathcal{H}_\mu}\mathcal{G}(m)$ μ -a.e. Additionally, the stochastic derivative carries over the parameter regularity given by the prior distribution μ , which makes it the more natural derivative definition for Bayesian inverse problems; see [Appendix A](#). Stochastic differentiability is an important part of our derivative-informed operator learning formulation; see [Section 3.2](#). We note that the stochastic derivative is often called the Malliavin derivative [60] or the H-derivative [61] in different contexts.

2.4. Local Gaussian approximation of the posterior using parametric derivative

Based on the differentiability assumption, we consider a linear expansion of the nonlinear PtO map \mathcal{G} at a given $m \in \mathcal{M}$:

$$\mathcal{G}(\cdot) \approx \mathcal{G}(m) + D_{\mathcal{H}_\mu}\mathcal{G}(m)(\cdot - m).$$

Replacing the PtO map in [\(3\)](#) using the linear expansion, we obtain a local Gaussian approximation to the posterior in closed form; see [57, Section 6.4]. It is a conditional probability distribution $\mathcal{Q}_{\text{local}} : \mathcal{M} \times \mathcal{B}(\mathcal{M}) \rightarrow [0, 1]$ given by:

$$\mu^y \approx \mathcal{Q}_{\text{local}}(m, \cdot) = \mathcal{N}(-D_{\mathcal{H}_\mu}\Phi^y(m), \mathcal{C}_{\text{post}}(m)), \quad (4)$$

where the negative mean $D_{\mathcal{H}_\mu}\Phi^y : \mathcal{M} \rightarrow \mathcal{H}_\mu$ is the \mathcal{H}_μ -Riesz representation of the stochastic derivative of the data misfit,

$$D_{\mathcal{H}_\mu}\Phi^y(m) := D_{\mathcal{H}_\mu}\mathcal{G}(m)^* (\mathcal{G}(m) - y), \quad (5)$$

and the covariance $\mathcal{C}_{\text{post}} : \mathcal{M} \rightarrow B_1^+(\mathcal{M})$ is given by

$$\mathcal{C}_{\text{post}}(m) := (\mathcal{I}_{\mathcal{H}_\mu} + \mathcal{H}(m))^{-1}\mathcal{C}_{\text{pr}}, \quad \mathcal{H}(m) := D_{\mathcal{H}_\mu}\mathcal{G}(m)^* D_{\mathcal{H}_\mu}\mathcal{G}(m), \quad (6)$$

where $\mathcal{I}_{\mathcal{H}_\mu}$ is the identity map on \mathcal{H}_μ , and $\mathcal{H} : \mathcal{M} \rightarrow B_1^+(\mathcal{H}_\mu)$ is a Gauss–Newton approximation to the stochastic Hessian of the data misfit in [\(B.2\)](#). The mappings $D_{\mathcal{H}_\mu}\Phi^y$ and \mathcal{H} are often known as the *prior-preconditioned gradient (ppg)* and the *prior-preconditioned Gauss–Newton Hessian (ppGNH)* in the context of inverse problems. We demonstrate their connections to the conventional definition in [Appendix B](#).

2.5. The Metropolis–Hasting algorithm

We use an MCMC method, the *Metropolis–Hasting (MH) algorithm*, to sample from the posterior distribution μ^y defined over infinite-dimensional \mathcal{M} . The MH algorithm is a procedure for generating reversible Markov chains $\{m_j\}_{j=1}^\infty$ on \mathcal{M} with a stationary distribution of μ^y . The algorithm prescribes a Markov chain transition rule (i.e., the law of $m_j \mapsto m_{j+1}$) based on an accept-reject move and a proposal distribution. The proposal, denoted by $\mathcal{Q} : \mathcal{M} \times \mathcal{B}(\mathcal{M}) \rightarrow [0, 1]$, is a conditional probability distribution. The proposal and the posterior jointly define a set of transition rates⁵ between two positions in \mathcal{M} as measures (unnormalized) on the product space $\mathcal{M} \times \mathcal{M}$:

$$\nu(\mathrm{d}m, \mathrm{d}m^\dagger) := \mathcal{Q}(m, \mathrm{d}m^\dagger)\mu^y(\mathrm{d}m), \quad \nu^T(\mathrm{d}m, \mathrm{d}m^\dagger) := \mathcal{Q}(m^\dagger, \mathrm{d}m)\mu^y(\mathrm{d}m^\dagger).$$

The MH algorithm is centered around the ratio of transition rates, $\rho : \mathcal{M} \times \mathcal{M} \rightarrow [0, \infty)$, defined as an RN derivative:

$$\rho(m, m^\dagger) := \frac{\nu^T(\mathrm{d}m, \mathrm{d}m^\dagger)}{\nu(\mathrm{d}m, \mathrm{d}m^\dagger)} = \frac{\mathcal{Q}(m^\dagger, \mathrm{d}m)\exp(-\Phi^y(m^\dagger))\mu(\mathrm{d}m^\dagger)}{\mathcal{Q}(m, \mathrm{d}m^\dagger)\exp(-\Phi^y(m))\mu(\mathrm{d}m)}, \quad (7)$$

⁵These transition rates should not be confused with the Markov chain transition rule of the MH algorithm.

where we use a change of measure in (2) to represent μ^y .

The accept-reject move is executed as follows. At a Markov chain position $m_j \in \mathcal{M}$, we sample a proposed move $m^\dagger \stackrel{\text{i.i.d.}}{\sim} \mathcal{Q}(m_j, \cdot)$. The next position is set to $m_{j+1} = m^\dagger$, i.e., acceptance, with probability $\alpha(m_j, m^\dagger) \in [0, 1]$ given by

$$\alpha(m_j, m^\dagger) := \min\{1, \rho(m_j, m^\dagger)\}.$$

Alternatively, we set $m_{j+1} = m_j$, i.e., rejection, with probability $1 - \alpha(m_j, m^\dagger)$. See Figure 1 (left) for a schematic of the MH algorithm.

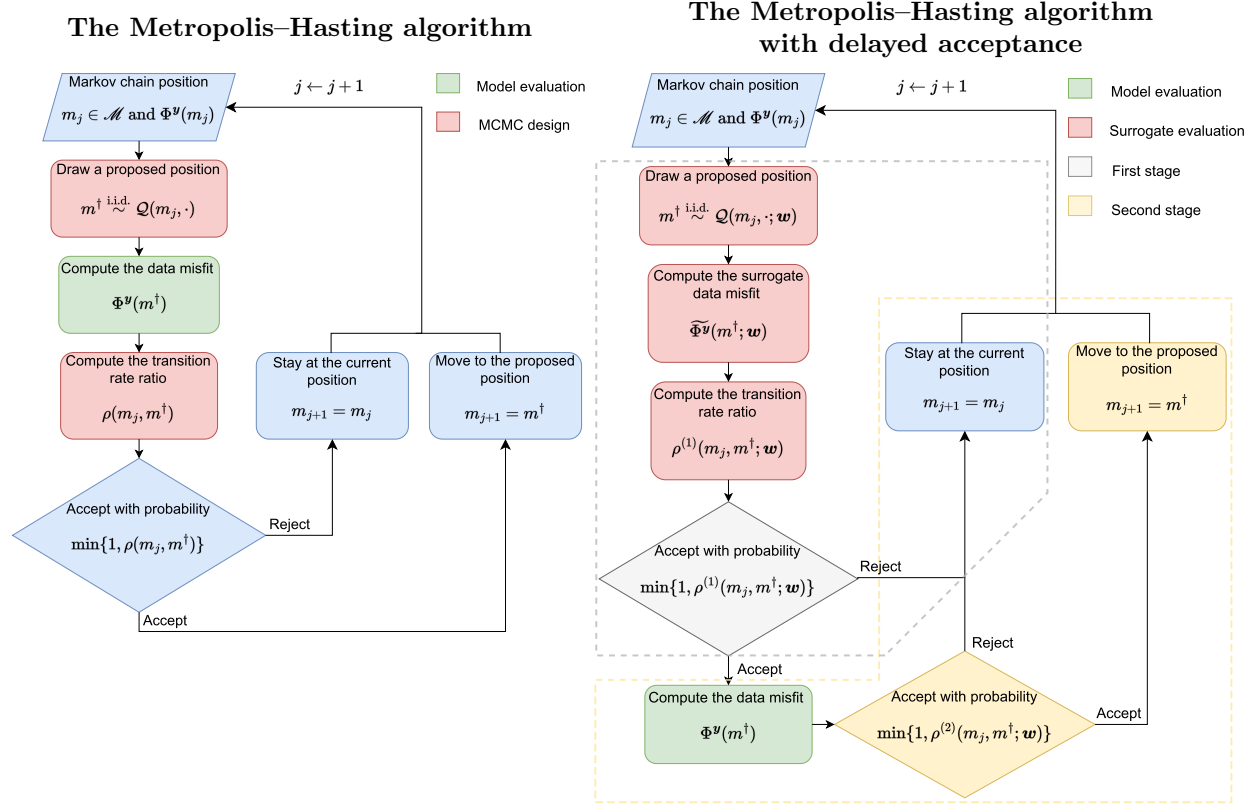


Figure 1: (left) A schematic of the Metropolis–Hasting algorithm for sampling from the posterior distribution μ^y as described in Section 2.5. (right) A schematic of the Metropolis–Hasting algorithm with delayed acceptance enabled by a surrogate PtO map $\tilde{\mathcal{G}}(\cdot; \mathbf{w})$ parameterized by \mathbf{w} . See Section 2.8 for a detailed description of the components of this algorithm.

2.6. Dimension-independent MCMC

This subsection briefly overviews the basics for designing dimension-independent MCMC methods. We refer to [24, 43, 45, 62] and references therein for more detailed discussions.

The main ingredient of designing a dimension-independent MCMC method using the MH algorithm is to design a proposal $\mathcal{Q}(m, \cdot)$ that ensures the transition rate ratio ρ in (7), is well-defined. According to the RN theorem [58, Theorem 2.29], ρ is well-defined if $\nu^T \ll \nu$, where \ll denotes the absolute continuity of measures. In particular, Tierney [62] proves that the MH algorithm does not accept any proposed move if ν^T and ν are mutually singular (i.e., disjoint probability concentrations). In finite dimensions, $\nu^T \ll \nu$ holds for most proposal choices (i.e., Gaussian random walk), and one typically expresses ν and ν^T in the form of probability densities. However, measures on infinite dimensional space tend to be mutually singular (see, e.g., Feldman–Hájek [58, Theorem 2.51]), and their probability densities do not exist [58, Theorem 2.38]. As a result of these unique properties of infinite dimensional probability distributions, a finite-dimensional MH

algorithm targeting a discretized infinite-dimensional sampling problem often leads to deteriorating sampling performance when the discretization is refined [42]. For example, the conventional Gaussian random walk proposal given by $\mathcal{Q}_{\text{RW}}(m, \cdot) := \mathcal{N}(m, s\mathcal{C}_{\text{pr}})$, $s > 0$, fails to be dimension-independent because it leads to an ill-defined ρ in (7); see [57, Example 5.3], [42, Section 2.4], and [45, Section 3.3].

The building block for a dimension-independent MCMC is the preconditioned Crank–Nicolson (pCN) proposal [24, 42] that is reversible with respect to the prior:

$$\mathcal{Q}_{\text{pCN}}(m, \cdot) := \mathcal{N}(sm, (1 - s^2)\mathcal{C}_{\text{pr}}), \quad s \leq 1, \quad (\text{The pCN proposal}) \quad (8a)$$

$$\mathcal{Q}_{\text{pCN}}(m^\dagger, dm)\mu(dm^\dagger) = \mathcal{Q}_{\text{pCN}}(m, dm^\dagger)\mu(dm). \quad (\text{Prior reversibility}) \quad (8b)$$

The equivalence of measure in (8b) leads to a well-defined transition rate ratio of the form:

$$\rho_{\text{pCN}}(m, m^\dagger) = \exp(\Phi^y(m) - \Phi^y(m^\dagger)).$$

The pCN proposal is used as a reference measure to derive the acceptance probability for proposals designed to include local geometry information of the posterior distribution [15, 16, 45]. In particular, these geometry-informed proposals are designed to possess well-defined and close-formed RN derivatives with respect to the pCN proposal. The existence of these derivatives leads to a well-defined MH algorithm in infinite-dimensional sample spaces. The closed forms of these RN derivatives allow us to numerically evaluate the acceptance probability.

2.7. Goemetric MCMC

We consider the simplified manifold Metropolis-adjusted Langevin algorithm, or mMALA, introduced in [15]. It originates from the following Langevin stochastic differential equation (SDE) on \mathcal{M} , preconditioned by a position-dependent trace class operator, $\mathcal{K} : \mathcal{M} \rightarrow B_1^+(\mathcal{M})$:

$$dM_t = -\frac{1}{2}\mathcal{K}(M_t)\mathcal{C}_{\text{pr}}^{-1}(M_t + D_{\mathcal{H}_\mu}\Phi^y(M_t)) dt + \mathcal{K}(M_t)^{1/2} dW_t, \quad t \geq 0, \quad (9)$$

where $\mathcal{K}(m)^{1/2}$ denotes the self-adjoint square root of $\mathcal{K}(m)$, W is a cylindrical Wiener process defined on \mathcal{M} . Such a Langevin SDE can be derived using a local reference measure of the form:

$$\mathcal{Q}_{\text{local}}(m, \cdot) = \mathcal{N}(\mathcal{M}(m), \mathcal{K}(m)), \quad (10)$$

where $\mathcal{M} : \mathcal{M} \rightarrow \mathcal{H}_\mu$ outputs the mean of the reference which does not appear in the SDE; see [15, Section 3.1]. We assume $\mathcal{K}(m)$ leads to the equivalence of measure between μ and $\mathcal{N}(0, \mathcal{K}(m))$ μ -a.e., following the Feldman–Hájek theorem [58, Theorem 2.5.1]. Discretizing the above SDE in time using a semi-implicit Euler scheme with a step size $\Delta t \in \mathbb{R}_+$ leads to the following proposal:

$$\mathcal{Q}_{\text{mMALA}}(m, \cdot) := \mathcal{N}(sm + (1 - s)\mathcal{A}(m), (1 - s^2)\mathcal{K}(m)), \quad (11a)$$

$$\mathcal{A}(m) := m - \mathcal{K}(m)\mathcal{C}_{\text{pr}}^{-1}(m + D_{\mathcal{H}_\mu}\Phi^y(m)), \quad s = \frac{4 - \Delta t}{4 + \Delta t}. \quad (11b)$$

Beskos et al. [15, Theorem 3.5] shows that the mMALA and pCN proposals are equivalent as probability measures μ -a.e., and the mMALA proposal leads to a well-defined transition rate ratio $\rho_{\text{mMALA}} : \mathcal{M} \times \mathcal{M} \rightarrow \mathbb{R}_+$ with a closed form given as follows:

$$\begin{aligned} \rho_{\text{mMALA}}(m_1, m_2) &:= \exp(\Phi^y(m_1) - \Phi^y(m_2)) \frac{\mathcal{Q}_{\text{mMALA}}(m_2, dm_1)\mu(dm_2)}{\mathcal{Q}_{\text{mMALA}}(m_1, dm_2)\mu(dm_1)} \\ &= \exp(\Phi^y(m_1) - \Phi^y(m_2)) \frac{\rho_0(m_2, m_1)}{\rho_0(m_1, m_2)}, \end{aligned}$$

where $\rho_0 : \mathcal{M} \times \mathcal{M} \rightarrow \mathbb{R}_+$ is the RN derivative between the mMALA and pCN proposals:

$$\begin{aligned}\rho_0(m_1, m_2) &:= \frac{\mathcal{Q}_{\text{mMALA}}(m_1, dm_2)}{\mathcal{Q}_{\text{pCN}}(m_1, dm_2)} \\ &= \exp\left(-\frac{\Delta t}{8} \|\mathcal{A}(m_1)\|_{\mathcal{K}(m_1)^{-1}}^2 + \frac{\sqrt{\Delta t}}{2} \langle \mathcal{A}(m_1), \hat{m} \rangle_{\mathcal{K}(m_1)^{-1}}\right) \\ &\quad \times \det_{\mathcal{M}} \left(\mathcal{C}_{\text{pr}}^{1/2} \mathcal{K}(m_1)^{-1} \mathcal{C}_{\text{pr}}^{1/2} \right)^{1/2} \exp\left(-\frac{1}{2} \|\hat{m}\|_{(\mathcal{K}(m_1)^{-1} - \mathcal{C}_{\text{pr}}^{-1})}^2\right),\end{aligned}\tag{12}$$

where $\hat{m} = (m_2 - sm_1)/\sqrt{1-s^2}$ and $\det_{\mathcal{M}} : B_1^+(\mathcal{M}) \rightarrow \mathbb{R}$ is the operator determinant given by eigenvalue product [63, Theorem 6.1].

The mMALA proposal allows for flexibility in (i) designing $\mathcal{K}(m)$, the covariance operator of the local reference measure in (10), and (ii) removing or reducing the ppg $D_{\mathcal{H}_\mu} \Phi^y$. For example, the mMALA proposal reduces to the pCN proposal in (8a) when $\mathcal{K}(m) = \mathcal{C}_{\text{pr}}$ and the ppg is removed. We may choose $\mathcal{K}(m)$ such that the local reference measure adapts to the local geometry of the posterior at each Markov chain position, such as $\mathcal{K}(m) \approx \mathcal{C}_{\text{post}}(m)$ using the local Gaussian approximation in (4). These proposals that incorporate posterior local geometry lead to a class of MCMC methods referred to as *dimension-independent geometric MCMC methods*.

2.8. Delayed acceptance MCMC

The DA MCMC method follows the MH algorithm targeting μ^y with a special choice of the proposal distribution: the Markov chain transition rule (i.e., the law of $m_j \rightarrow m_{j+1}$) of the MH algorithm targeting the surrogate posterior $\widetilde{\mu}^y \in \mathcal{P}(\mathcal{M})$ using a surrogate $\widetilde{\mathcal{G}} \approx \mathcal{G}$. The surrogate data misfit and posterior are given by

$$\widetilde{\Phi}^y(m) := \frac{1}{2} \left\| \mathbf{y} - \widetilde{\mathcal{G}}(m) \right\|_{\mathcal{C}_n^{-1}}^2, \quad (\text{Surrogate data misfit}) \tag{13a}$$

$$\frac{\widetilde{\mu}^y(dm)}{\mu(dm)} \propto \exp(-\widetilde{\Phi}^y(m)). \quad (\text{Surrogate posterior}) \tag{13b}$$

The DA procedure can be broken down into two stages at each Markov chain position m_j with a proposed move $m^\dagger \stackrel{\text{i.i.d.}}{\sim} \mathcal{Q}(m, \cdot)$.

1. We perform a pass-reject move based on the transition rate ratio in (7) using surrogate data misfit evaluations:

$$\rho^{(1)}(m_j, m^\dagger) = \frac{\mathcal{Q}(m^\dagger, dm_j) \exp(-\widetilde{\Phi}^y(m^\dagger)) \mu(dm^\dagger)}{\mathcal{Q}(m_j, dm^\dagger) \exp(-\widetilde{\Phi}^y(m_j)) \mu(dm_j)}.$$

We pass m^\dagger to the second stage with probability $\alpha^{(1)}(m_j, m^\dagger) := \min\{1, \rho^{(1)}(m_j, m^\dagger)\}$. Alternatively, we skip the second stage and set the next position to $m_{j+1} = m_j$ (i.e., rejection) with probability $1 - \alpha^{(1)}(m_j, m^\dagger)$.

2. We perform an accept-reject move of the MH algorithm based on a proposal $\mathcal{Q}_{\text{DA}}(m, dm^\dagger)$ prescribed by the first stage pass-reject move:

$$\mathcal{Q}_{\text{DA}}(m, dm^\dagger) = \alpha^{(1)}(m_j, m^\dagger) \mathcal{Q}(m, dm^\dagger) + (1 - \alpha^{(1)}(m_j, m^\dagger)) \delta_{m_j}(dm^\dagger),$$

where δ_{m_j} is the Dirac mass concentrated on m_j . Since \mathcal{Q}_{DA} is reversible with respect to $\widetilde{\mu}^y$ (i.e., the detailed balance condition [9]), we have

$$\mathcal{Q}_{\text{DA}}(m, dm^\dagger) \widetilde{\mu}^y(dm) = \mathcal{Q}_{\text{DA}}(m^\dagger, dm) \widetilde{\mu}^y(dm^\dagger).$$

As a result, the transition rate ratio of the DA procedure based on \mathcal{Q}_{DA} is given by

$$\rho^{(2)}(m_j, m^\dagger) = \frac{\exp(-\widetilde{\Phi}^y(m_j)) \exp(-\Phi^y(m^\dagger))}{\exp(-\widetilde{\Phi}^y(m^\dagger)) \exp(-\Phi^y(m_j))}. \quad (14)$$

See [Figure 1](#) (right) for a schematic of the DA MCMC algorithm.

An important feature of the DA procedure is that it allows proposed moves to be rejected in the first stage solely based on operator surrogate evaluations. Such a feature potentially leads to a significant reduction in the query counts of the true PtO map during posterior sampling. On the other hand, the efficiency of DA MCMC relies heavily on the quality of surrogate approximation. When the operator surrogate predictions of the observable are accurate, most rejections occur during the first stage without PtO map evaluations, and most proposed moves passed to the second stage are accepted. Higher surrogate approximation error leads to more frequent second-stage rejection, thus increases average computational cost per Markov chain sample and deteriorates posterior sampling efficiency. See [Section 4.4](#) for more discussion on surrogate approximation in DA.

3. Operator learning in H_μ^1 Sobolev space with Gaussian measure

We consider an operator learning problem of optimizing the weight $\mathbf{w} \in \mathbb{R}^{d_w}$ of an operator surrogate $\widetilde{\mathcal{G}}(\cdot; \mathbf{w}) : \mathcal{M} \rightarrow \mathcal{Y}$ so that $\widetilde{\mathcal{G}}$ is close to the true PtO map \mathcal{G} measured by certain metric. When the operator surrogate $\widetilde{\mathcal{G}}$ is represented using a neural network, the weight \mathbf{w} consists of the tunable parameters of neural networks. In [Section 3.1](#), we introduce the conventional operator learning method using input–output samples. In [Section 3.2](#), we present our derivative-informed operator learning method. In [Section 3.3](#), we discuss the matrix representation of the parametric derivative for efficient operator learning.

3.1. Operator learning in L_μ^2 Bochner space

The typical operator learning method approximates the PtO map in the $L_\mu^2(\mathcal{M}; \mathcal{Y})$ Bochner space, or L_μ^2 for short. It is defined by:

$$\begin{aligned} L_\mu^2(\mathcal{M}; \mathcal{Y}) &:= \left\{ \mathcal{T} : \mathcal{M} \rightarrow \mathcal{Y} \mid \|\mathcal{T}\|_{L_\mu^2} < \infty \right\}, & (L_\mu^2 \text{ Definition}) \\ \|\mathcal{T}\|_{L_\mu^2(\mathcal{M}; \mathcal{Y})} &:= \left(\mathbb{E}_{M \sim \mu} \left[\|\mathcal{T}(M)\|_{C_n^{-1}}^2 \right] \right)^{1/2}. & (L_\mu^2 \text{ norm}) \end{aligned}$$

The operator learning objective can be formulated by controlling the approximation error in $L_\mu^2(\mathcal{M}; \mathcal{Y})$:

$$\mathbf{w}^\dagger = \arg \min_{\mathbf{w} \in \mathbb{R}^{d_w}} \mathcal{L}_{L_\mu^2}^\infty(\mathbf{w}), \quad (\text{Operator learning objective}) \quad (15a)$$

$$\mathcal{L}_{L_\mu^2}^\infty(\mathbf{w}) := \frac{1}{2} \left\| \mathcal{G} - \widetilde{\mathcal{G}}(\cdot; \mathbf{w}) \right\|_{L_\mu^2(\mathcal{M}; \mathcal{Y})}^2. \quad (\text{Error control in } L_\mu^2(\mathcal{M}; \mathcal{Y})) \quad (15b)$$

The objective $\mathcal{L}_{L_\mu^2}^\infty$ can be estimated via inout–output pairs $\{m_j, \mathcal{G}(m_j)\}_{j=1}^{n_t}$ with $m_j \stackrel{\text{i.i.d.}}{\sim} \mu$, which leads to a loss function $\mathcal{L}_{L_\mu^2}^{n_t}$ defined as follows:

$$\mathcal{L}_{L_\mu^2}^\infty(\mathbf{w}) \approx \mathcal{L}_{L_\mu^2}^{n_t}(\mathbf{w}; \{m_j\}_{j=1}^{n_t}) := \frac{1}{2n_t} \sum_{j=1}^{n_t} \left\| \mathcal{G}(m_j) - \widetilde{\mathcal{G}}(m_j; \mathbf{w}) \right\|_{C_n^{-1}}^2. \quad (16)$$

The operator surrogate can be constructed via finding \mathbf{w}^\dagger that minimizes $\mathcal{L}_{L_\mu^2}^{n_t}$.

3.2. Operator learning in H_μ^1 Sobolev space with Gaussian measure

In this work, we are interested in designing MCMC methods using operator surrogate that requires small approximation errors in both operator evaluations (for approximating ppg in (5) and efficient DA procedure) and its derivative evaluations (for approximating the ppg and ppGNH in (5) and (6)). Therefore, we consider controlling the operator surrogate error in the *H^1 Sobolev space with Gaussian measure*, or H_μ^1 for short. It is a Hilbert space of nonlinear mappings with an inner product-induced norm that measures the distance between nonlinear mappings using *the discrepancy in their stochastic derivative evaluations* in addition to the discrepancy in their evaluations:

$$H_\mu^1(\mathcal{M}; \mathcal{Y}) := \left\{ \mathcal{T} \in L_\mu^2(\mathcal{M}; \mathcal{Y}) \mid \|D_{\mathcal{H}_\mu} \mathcal{T}(M)\|_{L_\mu^2(\mathcal{M}; \text{HS}(\mathcal{H}_\mu, \mathcal{Y}))} < \infty \right\}, \quad (H_\mu^1 \text{ Definition})$$

$$\|\mathcal{T}\|_{H_\mu^1(\mathcal{M}; \mathcal{Y})} := \left(\| \mathcal{T} \|^2_{L_\mu^2(\mathcal{M}; \mathcal{Y})} + \| D_{\mathcal{H}_\mu} \mathcal{T} \|^2_{L_\mu^2(\mathcal{M}; \text{HS}(\mathcal{H}_\mu, \mathcal{Y}))} \right)^{1/2}, \quad (H_\mu^1 \text{ norm})$$

$$\|D_{\mathcal{H}_\mu} \mathcal{T}\|_{L_\mu^2(\mathcal{M}; \text{HS}(\mathcal{H}_\mu, \mathcal{Y}))} := \left(\mathbb{E}_{M \sim \mu} \left[\|D_{\mathcal{H}_\mu} \mathcal{T}(M)\|_{\text{HS}(\mathcal{H}_\mu, \mathcal{Y})}^2 \right] \right)^{1/2}. \quad (\text{Derivative norm})$$

See [59] and references therein for a detailed discussion on the definition and properties of $H_\mu^1(\mathcal{M}; \mathcal{Y})$. The following logarithmic Sobolev (Theorem 3.1) and Poincaré (Theorem 3.2) inequalities hold on $H_\mu^1(\mathcal{M}; \mathcal{Y})$, which are essential for establishing approximation error bounds on operator surrogate and Bayesian inversion. In particular, we are able to obtain a Poincaré constant of 1 on $H_\mu^1(\mathcal{M}; \mathcal{Y})$.

Theorem 3.1 (Logarithmic Sobolev inequality). [59, 5.5.1] If $\mathcal{S} \in H_\mu^1(\mathcal{M}) := H_\mu^1(\mathcal{M}; \mathbb{R})$, then the following inequality holds

$$\mathbb{E}_{M \sim \mu} [\mathcal{S}(M)^2 \ln(|\mathcal{S}(M)|)] \leq \mathbb{E}_{M \sim \mu} \left[\|D_{\mathcal{H}_\mu} \mathcal{S}(M)\|_{\mathcal{H}_\mu}^2 \right] + \frac{1}{2} \mathbb{E}_{M \sim \mu} [\mathcal{S}(M)^2] \ln(\mathbb{E}_{M \sim \mu} [\ln(\mathcal{S}(M)^2)]).$$

where $D_{\mathcal{H}_\mu} \mathcal{S}$ is the \mathcal{H}_μ -Riesz representation of the stochastic derivative of \mathcal{S} .

Theorem 3.2 (Poincaré inequality). [59, 5.5.6] If $\mathcal{T} \in H_\mu^1(\mathcal{M}; \mathcal{Y})$, then

$$\|\mathcal{T} - \mathbb{E}_{M \sim \mu} [\mathcal{T}(M)]\|_{L_\mu^2(\mathcal{M}; \mathcal{Y})}^2 \leq \|D_{\mathcal{H}_\mu} \mathcal{T}\|_{L_\mu^2(\mathcal{M}; \text{HS}(\mathcal{H}_\mu, \mathcal{Y}))}^2.$$

The operator learning problem with error control in $H_\mu^1(\mathcal{M}; \mathcal{Y})$ is formulated as

$$\mathbf{w}^\dagger = \arg \min_{\mathbf{w} \in \mathbb{R}^{d_w}} \mathcal{L}_{H_\mu^1}^\infty(\mathbf{w}), \quad (\text{Operator learning objective}) \quad (17a)$$

$$\mathcal{L}_{H_\mu^1}^\infty := \frac{1}{2} \left\| \mathcal{G} - \tilde{\mathcal{G}}(\cdot; \mathbf{w}) \right\|_{H_\mu^1(\mathcal{M}; \mathcal{Y})}^2. \quad (\text{Error control in } H_\mu^1(\mathcal{M}; \mathcal{Y})) \quad (17b)$$

The operator learning objective $\mathcal{L}_{H_\mu^1}^\infty$ can be estimated via samples of the input–output–stochastic derivative tuple $\{m_j, \mathcal{G}(m_j), D_{\mathcal{H}_\mu} \mathcal{G}(m_j)\}_{j=1}^{n_t}$ with $m_j \stackrel{\text{i.i.d.}}{\sim} \mu$, which leads to a loss function $\mathcal{L}_{H_\mu^1}^{n_t}$ defined as follows:

$$\begin{aligned} \mathcal{L}_{H_\mu^1}^\infty(\mathbf{w}) &\approx \mathcal{L}_{H_\mu^1}^{n_t}(\mathbf{w}; \{m_j\}_{j=1}^{n_t}) \\ &:= \frac{1}{2n_t} \sum_{j=1}^{n_t} \left(\left\| \mathcal{G}(m_j) - \tilde{\mathcal{G}}(m_j; \mathbf{w}) \right\|_{\mathbf{C}_n^{-1}}^2 + \left\| D_{\mathcal{H}_\mu} \mathcal{G}(m_j) - D_{\mathcal{H}_\mu} \tilde{\mathcal{G}}(m_j; \mathbf{w}) \right\|_{\text{HS}(\mathcal{H}_\mu, \mathcal{Y})}^2 \right). \end{aligned} \quad (18)$$

We refer to the operator surrogates constructed using error control in H_μ^1 as derivative-informed operator surrogates. In the context of neural network-based operator learning, we refer to the resulting operator surrogates as *derivative-informed neural operators* (DINOs) [23].

3.3. Matrix representation of derivative

We consider a matrix representation of the stochastic derivative for the purpose of generating training samples, which are used to numerically estimate the H_μ^1 loss function and its gradient with respect to the weight \mathbf{w} . For an arbitrary pair of orthonormal basis (ONB) on the parameter and observable CM spaces

$$\mathcal{H}_\mu\text{-ONB} : \{\psi_k\}_{k=1}^\infty, \quad \mathcal{Y}\text{-ONB} : \{\mathbf{v}_j\}_{j=1}^{d_y},$$

we define a *Jacobian*, denoted by $\mathbf{J} : \mathcal{M} \rightarrow \text{HS}(l^2, \mathbb{R}^{d_y})$ where l^2 denotes the Hilbert space of squared-summable sequences, using an isometric isomorphism between $\text{HS}(l^2, \mathbb{R}^{d_y})$ and $\text{HS}(\mathcal{H}_\mu, \mathcal{Y})$ defined by the bases:

$$(\mathbf{J}(m))_{jk} := \mathbf{v}_j^T \mathbf{C}_n^{-1} D_{\mathcal{H}_\mu} \mathbf{G}(m) \psi_k, \quad (\text{Bijective linear mapping}) \quad (19a)$$

$$(\mathbf{J}(m)^T)_{jk} := \langle \psi_j, D_{\mathcal{H}_\mu} \mathbf{G}(m)^* \mathbf{v}_k \rangle_{\mathcal{C}_{\text{pr}}^{-1}}, \quad (\text{Jacobian matrix transpose}) \quad (19b)$$

$$\|\mathbf{J}(m)\|_F = \|D_{\mathcal{H}_\mu} \mathbf{G}(m)\|_{\text{HS}(\mathcal{H}_\mu; \mathcal{Y})}, \quad (\text{Isometry}) \quad (19c)$$

where $\|\cdot\|_F$ is the Frobenius norm. We note that the Frobenius and HS inner products are the same on $\text{HS}(l^2, \mathbb{R}^{d_y})$ and we may interpret $\mathbf{J}(m)$ as a matrix via its components as in (19a) and (19b). Importantly, the isometry in (19c) is independent of the choice of basis, while the mapping between \mathbf{J} and $D_{\mathcal{H}_\mu} \mathbf{G}$ in (19a) depends on the choice of basis.

With matrix representations, training samples can be generated as Jacobian matrices via actions or adjoint actions of the derivative at each parameter sample. Furthermore, we can estimate the derivative approximation error at each parameter sample via the Frobenius norm of the error in the Jacobian matrices. However, the size of Jacobian matrices can be problematic in numerical computation. Assume that numerical computation is performed in a discretized parameter space $\mathcal{M}^h \subset \mathcal{M}$ using the Galerkin method, where \mathcal{M}^h is isomorphic to \mathbb{R}^{d_m} . Then, the discretized Jacobian \mathbf{J}^h outputs $\mathbb{R}^{d_y \times d_m}$ matrices, i.e., $\mathbf{J}^h : \mathcal{M}^h \rightarrow \mathbb{R}^{d_y \times d_m}$; thus, storing and learning the Jacobian matrices generated at a large number of parameter samples can be intractable for large-scale problems. As a result, dimension reduction of the parameter space is essential for derivative-informed H_μ^1 operator learning.

The authors in [23] argue that restricting the derivative-informed operator learning using a pre-determined rank- r reduced basis $\{\psi_j\}_{j=1}^r$ with $r \ll d_m$ leads to tractable and accurate learning of the derivative for a wide-range of PDE models. We adopt this strategy in this work. The following section describes DINO with error control in H_μ^1 that extends the framework in [23] to our setting.

4. Reduced basis derivative-informed neural operator

Assume for now that we have a set of reduced \mathcal{H}_μ -ONBs of rank r denoted by $\{\psi_j\}_{j=1}^r$. They define a pair of linear encoders $\Psi_r^* \in \text{HS}(\mathcal{H}_\mu, \mathbb{R}^r)$ and decoders $\Psi_r \in \text{HS}(\mathbb{R}^r, \mathcal{H}_\mu)$ on \mathcal{H}_μ with $\Psi_r^* \Psi_r = \mathbf{I}_r \in \mathbb{R}^{r \times r}$, where \mathbf{I}_r is the identity matrix:

$$\Psi_r^* : \mathcal{H}_\mu \ni m \mapsto \sum_{j=1}^r \langle m, \psi_j \rangle_{\mathcal{C}_{\text{pr}}^{-1}} \mathbf{e}_j \in \mathbb{R}^r, \quad (\text{Parameter encoder}) \quad (20a)$$

$$\Psi_r : \mathbb{R}^r \ni \mathbf{m}_r \mapsto \sum_{j=1}^r (\mathbf{m}_r)_j \psi_j \in \mathcal{H}_\mu, \quad (\text{Parameter decoder}) \quad (20b)$$

where Ψ_r^* is the adjoint of Ψ_r and \mathbf{e}_j is the unit vector along the j th coordinate. Using the matrix representation of the HS operator introduced in Section 3.3, the linear encoder and decoder may be represented as

$$\Psi_r = \begin{bmatrix} | & | & & | \\ \psi_1 & \psi_2 & \cdots & \psi_r \\ | & | & & | \end{bmatrix}, \quad \Psi_r^* = \begin{bmatrix} \cdots & \langle \psi_1, \cdot \rangle_{\mathcal{C}_{\text{pr}}^{-1}} & \cdots \\ \cdots & \langle \psi_2, \cdot \rangle_{\mathcal{C}_{\text{pr}}^{-1}} & \cdots \\ \vdots & & \\ \cdots & \langle \psi_r, \cdot \rangle_{\mathcal{C}_{\text{pr}}^{-1}} & \cdots \end{bmatrix}.$$

We extend the range and domain of the encoder and decoder from \mathcal{H}_μ to \mathcal{M} and define a projection operator \mathcal{P}_r on \mathcal{M} using the encoder and decoder as follows:

$$\mathcal{P}_r := \Psi_r \Psi_r^* : \mathcal{M} \rightarrow \text{span}(\{\psi_j\}_{j=1}^r).$$

We emphasize that the \mathcal{M} -adjoint of Ψ_r is $\Psi_r^* \mathcal{C}_{\text{pr}}$, and the \mathcal{M} -adjoint of Ψ_r^* is $\mathcal{C}_{\text{pr}}^{-1} \Psi_r$.

Similarly, let $\mathbf{V} \in \text{HS}(\mathbb{R}^{d_y}, \mathcal{Y})$ be a matrix with columns consist of \mathcal{Y} -ONB vectors $\{\mathbf{v}_j\}_{j=1}^{d_y}$:

$$\mathbf{V} = \begin{bmatrix} & & & \\ \mathbf{v}_1 & \mathbf{v}_2 & \cdots & \mathbf{v}_r \\ & & & \end{bmatrix}.$$

We note that $\mathbf{V}^* = \mathbf{V}^T \mathbf{C}_n^{-1}$, where \mathbf{V}^T is the matrix transpose of \mathbf{V} .

Following [23], we parameterize the operator surrogate using a neural network $\mathbf{f}_{\text{NN}} : \mathbb{R}^r \times \mathbb{R}^{d_w} \rightarrow \mathbb{R}^{d_y}$:

$$\tilde{\mathcal{G}}(m; \mathbf{w}) := \mathbf{V} \mathbf{f}_{\text{NN}}(\Psi_r^* m, \mathbf{w}), \quad (\text{Reduced basis neural operator}) \quad (21)$$

The neural network represents the nonlinear mapping from the coefficients in the parameter reduced basis $\{\psi_j\}_{j=1}^r$ and the coefficients in the observable basis $\{\mathbf{v}_j\}_{j=1}^{d_y}$.

Remark 1. *In this work, we restrict our attention to parameter dimension reduction only. We acknowledge that observable dimension reduction is essential for many Bayesian inverse problems, such as those with high-resolution image data and time-evolving data. Recent theoretical works by Baptista et. al [64] studied optimal joint parameter and data dimension reduction in the context of Bayesian inversion based on logarithmic Sobolev inequality, which can be readily applied to our setting due to Theorem 3.1. However, there are many more practical considerations when jointly reducing the input and output dimensions for efficient DINO training. For this reason, we reserve observable dimension reduction for future work.*

The stochastic derivative of the operator surrogate and its adjoint can be expressed using the operator surrogate reduced Jacobian $\tilde{\mathbf{J}}_r(\cdot; \mathbf{w}) : \mathcal{M} \rightarrow \mathbb{R}^{d_y \times r}$ through the neural network Jacobian $\partial_{\mathbf{m}_r} \mathbf{f}_{\text{NN}}(\cdot, \mathbf{w}) : \mathbb{R}^r \rightarrow \mathbb{R}^{d_y \times r}$:

$$\tilde{\mathbf{J}}_r(m; \mathbf{w}) := \partial_{\mathbf{m}_r} \mathbf{f}_{\text{NN}}(\Psi_r^* m, \mathbf{w}), \quad \begin{cases} D_{\mathcal{H}_\mu} \tilde{\mathcal{G}}(m; \mathbf{w}) = \mathbf{V} \tilde{\mathbf{J}}_r(m; \mathbf{w}) \Psi_r^*, \\ D_{\mathcal{H}_\mu} \tilde{\mathcal{G}}(m; \mathbf{w})^* = \Psi_r \tilde{\mathbf{J}}_r(m; \mathbf{w})^T \mathbf{V}^*. \end{cases}$$

Using the reduced basis architecture in (21) with \mathcal{H}_μ and \mathcal{Y} -ONBs and the isometric isomorphism in (19a), the derivative-informed H^1_μ operator learning objective in (17) can be reduced:

$$\begin{aligned} \mathcal{L}_{H_\mu}^\infty(\mathbf{w}) &:= \frac{1}{2} \mathbb{E}_{M \sim \mu} \left[\left\| \underbrace{\mathcal{G}(M) - \mathbf{V} \mathbf{f}_{\text{NN}}(\Psi_r^* M, \mathbf{w})}_{\in \mathbb{R}^{d_y}} \right\|_{\mathbf{C}_n^{-1}}^2 + \left\| \underbrace{D_{\mathcal{H}_\mu} \mathcal{G}(M) - \mathbf{V} \partial_{\mathbf{m}_r} \mathbf{f}_{\text{NN}}(\Psi_r^* M, \mathbf{w}) \Psi_r^*}_{\mathbf{J}(M) - \tilde{\mathbf{J}}(M; \mathbf{w}) \in \mathbb{R}^{d_y \times \infty}} \right\|_{\text{HS}(\mathcal{H}_\mu, \mathcal{Y})}^2 \right] \\ &\propto \frac{1}{2} \mathbb{E}_{M \sim \mu} \left[\left\| \underbrace{\mathbf{V}^* \mathcal{G}(M) - \mathbf{f}_{\text{NN}}(\Psi_r^* M, \mathbf{w})}_{\in \mathbb{R}^{d_y}} \right\|^2 + \left\| \underbrace{\mathbf{V}^* D_{\mathcal{H}_\mu} \mathcal{G}(M) \Psi_r - \partial_{\mathbf{m}_r} \mathbf{f}_{\text{NN}}(\Psi_r^* M, \mathbf{w})}_{\mathbf{J}_r(M) - \tilde{\mathbf{J}}_r(M; \mathbf{w}) \in \mathbb{R}^{d_y \times r}} \right\|_F^2 \right], \end{aligned}$$

where constant terms independent of \mathbf{w} are eliminated from the second line and the reduced Jacobian $\mathbf{J}_r : \mathcal{M} \rightarrow \mathbb{R}^{d_y \times r}$ of the PtO map is given by

$$\mathbf{J}_r(m) := \mathbf{V}^* D_{\mathcal{H}_\mu} \mathcal{G}(m) \Psi_r. \quad (\text{Reduced Jacobian matrix})$$

The reduced loss function can now be estimated via samples of $\{m_j, \mathbf{V}^* \mathcal{G}(m_j), \mathbf{J}_r(m_j)\}_{j=1}^{n_t}$ with $m_j \stackrel{\text{i.i.d.}}{\sim} \mu$.

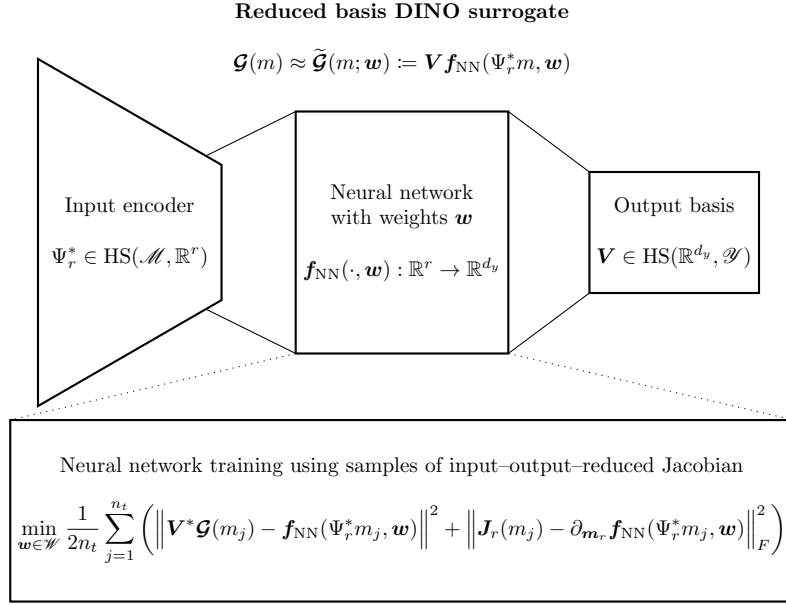


Figure 2: A schematic of reduced basis DINO architecture and learning for surrogate approximation $\tilde{\mathcal{G}} \approx \mathcal{G}$ in $H_\mu^1(\mathcal{M}; \mathcal{Y})$.

4.1. A brief recap

We emphasize the following important points about our derivative-informed operator learning formulation:

1. The derivative-informed operator learning $\mathcal{G} \approx \tilde{\mathcal{G}}(\cdot; \mathbf{w})$ is formulated as an approximation problem in $H_\mu^1(\mathcal{M}; \mathcal{Y})$, a Sobolev space of nonlinear mappings between two separable Hilbert spaces \mathcal{M} and \mathcal{Y} . While the parameter space \mathcal{M} has infinite dimensions and the observable CM space \mathcal{Y} has finite dimensions in our setting, the learning formulation is general and can be applied to infinite-dimensional output spaces. However, the stochastic derivative must remain an HS operator when the output space becomes a separable Hilbert.
2. The neural network of the reduced basis DINO learns the nonlinear mapping from the reduced parameter $\Psi_r^* m$ to the model-predicted coefficients in the observable basis vectors $\mathbf{V}^* \mathcal{G}(m)$:

$$\mathbf{f}_{\text{NN}}(\cdot, \mathbf{w}) \approx \Psi_r^* m \mapsto \mathbf{V}^* \mathcal{G}(m). \quad (\text{Neural network approximation})$$

3. The neural network Jacobian of the reduced basis DINO learns the nonlinear mapping from the reduced parameter $\Psi_r^* m$ to the model-predicted reduced Jacobian matrix $\mathbf{J}_r(m)$:

$$\partial_{\mathbf{m}_r} \mathbf{f}_{\text{NN}}(\cdot, \mathbf{w}) \approx \Psi_r^* m \mapsto \mathbf{J}_r(m). \quad (\text{Neural network Jacobian approximation})$$

4. As a result of this reduced basis architecture, the training sample storage and training cost is independent of the discretization dimension of the parameter space.

Remark 2. *In the following presentation, we often omit the notation for dependency on the neural network parameter \mathbf{w} and use the tilde symbol $\tilde{\cdot}$ when referring to the quantities computed via surrogate evaluations.*

4.2. Derivative and prior-based reduced bases

This subsection describes two popular types of reduced bases that can be used to construct DINO. The first type is based on the derivative-informed subspace (DIS) [29, 48, 65, 66]. The reduced bases for the

derivative-informed subspace can be found by the following eigenvalue problem in \mathcal{H}_μ for the ppGNH (6):

$$\begin{aligned} \text{Find } \{(\lambda_j^{\text{DIS}}, \psi_j^{\text{DIS}}) \in \mathbb{R}_+ \times \mathcal{H}_\mu\}_{j=1}^\infty \text{ with decreasing } \lambda_j^{\text{DIS}} \text{ such that} \\ \begin{cases} (\mathbb{E}_{M \sim \mu} [\mathcal{H}(M)] - \lambda_j^{\text{DIS}} \mathcal{I}_{\mathcal{H}_\mu}) \psi_j^{\text{DIS}} = 0, & j \in \mathbb{N}; \\ \langle \psi_j^{\text{DIS}}, \psi_k^{\text{DIS}} \rangle_{\mathcal{C}_{\text{pr}}^{-1}} = \delta_{jk} & j, k \in \mathbb{N}. \end{cases} \end{aligned} \quad (22)$$

We select the first r bases that correspond to the r largest eigenvalues to form encoders and decoders. During numerical computation, a Monte Carlo estimate of the expected ppGNH $\mathbb{E}_{M \sim \mu} [\mathcal{H}(M)]$ is computed at a set of prior samples $m_j \stackrel{\text{i.i.d.}}{\sim} \mu$, $j = 1, \dots, n_{\text{DIS}}$:

$$\widehat{\mathcal{H}}(\{m_j\}_{j=1}^{n_{\text{DIS}}}) := \frac{1}{n_{\text{DIS}}} \sum_{j=1}^{n_{\text{DIS}}} \mathcal{H}(m_j) \approx \mathbb{E}_{M \sim \mu} [\mathcal{H}(M)]. \quad (23)$$

We then solve the eigenvalue problem in (22) for the eigenpairs $\{(\widehat{\lambda}_j^{\text{DIS}}, \widehat{\psi}_j^{\text{DIS}})\}_{j=1}^r$ of $\widehat{\mathcal{H}}$, which gives the following DIS approximation of the expected ppGNH:

$$\mathbb{E}_{M \sim \mu} [\mathcal{H}(M)] \approx \widehat{\Psi}_r^{\text{DIS}} \widehat{\Lambda}_r^{\text{DIS}} \widehat{\Psi}_r^{\text{DIS}}^*, \quad (24)$$

where the linear encoder and decoder are defined as in (20) and $\widehat{\Lambda}_r^{\text{DIS}} \in \mathbb{R}^{r \times r}$ is a diagonal matrix consists of the eigenvalues.

The second type of reduced bases is based on the Karhunen–Loève expansion (KLE) of the prior distribution:

$$M = \sum_{j=1}^{\infty} \sqrt{\lambda_j^{\text{KLE}}} \Xi_j \eta_j \sim \mu, \quad \Xi_j \stackrel{\text{i.i.d.}}{\sim} \mathcal{N}(0, 1), \quad \langle \eta_j, \eta_k \rangle_{\mathcal{M}} = \delta_{jk},$$

where $\{(\lambda_j^{\text{KLE}}, \eta_j) \in \mathbb{R}_+ \times \mathcal{M}\}_{j=1}^\infty$ are eigenpairs of the prior covariance \mathcal{C}_{pr} with \mathcal{M} -orthonormal eigenbases and decreasing eigenvalues. We refer to the r -dimensional subspace spanned by $\{\eta_j\}_{j=1}^r$ as the rank- r KLE subspace or simply the KLE subspace. A set of reduced \mathcal{H}_μ -ONBs of the KLE subspace $\{\psi_j^{\text{KLE}}\}_{j=1}^r$ can be found by

$$\psi_j^{\text{KLE}} = \sqrt{\lambda_j^{\text{KLE}}} \eta_j, \quad 0 \leq j \leq r.$$

The KLE reduced bases $\{\psi_j^{\text{KLE}}\}_{j=1}^r$ can be computed with high precision for some representations of the \mathcal{C}_{pr} , notably Laplacian inverse or bi-Laplacian inverse Matérn covariances for Gaussian random functions [67, 68]. More generally, the KLE reduced bases can be approximated from samples.

4.3. Training sample generation and cost analysis for PDE models

We describe a training sample generation procedure and its cost analysis when the PtO map \mathcal{G} is defined through a PDE model. In particular, we consider an abstract variational residual form of the PDE as follows:

$$\text{Given } m \in \mathcal{M} \text{ find } u \in \mathcal{U} \text{ such that } \mathcal{R}(u, m) = 0 \in \mathcal{V},$$

where \mathcal{U} and \mathcal{V} are Hilbert spaces corresponding to the spaces of PDE state and residual, and $\mathcal{R} : \mathcal{U} \times \mathcal{M} \rightarrow \mathcal{V}$ is the PDE residual operator. The residual space \mathcal{V} is the dual space of the *space of adjoint variable* in the context of PDE-constrained optimization [69, 70] and the two spaces are identical when \mathcal{V} is a Hilbert space. While the numerical examples in this work focus on steady-state problems where \mathcal{U} is a Sobolev space defined over a spatial domain, our methodology is general and also applies to e.g., time-evolving problems where \mathcal{U} is a time-evolving Sobolev space.

A PDE solution operator $\mathcal{F} : \mathcal{M} \rightarrow \mathcal{U}$ is then composed with a linear observation operator $\mathcal{O} \in \text{HS}(\mathcal{U}, \mathcal{Y})$ to define the PtO map \mathcal{G} :

$$\mathcal{G} := \mathcal{O} \circ \mathcal{F}, \quad \mathcal{R}(\mathcal{F}(m), m) = 0 \quad \mu\text{-a.e.}$$

Each evaluation of the PtO map requires solving a PDE. The action of the stochastic derivative of the forward problem and its adjoint can be explicitly defined using the stochastic derivative of the PDE solution operator $D_{\mathcal{H}_\mu} \mathcal{F}(m) \in B(\mathcal{H}_\mu, \mathcal{U})$:

$$D_{\mathcal{H}_\mu} \mathcal{G}(m) \delta m = (\mathcal{O} \circ D_{\mathcal{H}_\mu} \mathcal{F}(m)) \delta m, \quad D_{\mathcal{H}_\mu} \mathcal{G}(m)^* \delta \mathbf{y} = (D_{\mathcal{H}_\mu} \mathcal{F}(m)^* \circ \mathcal{O}^*) \delta \mathbf{y},$$

where the action of the derivative is given by the partial Gâteaux derivatives of the residual with respect to the PDE state and the parameter (in the direction of \mathcal{H}_μ), denoted by $\partial_{\mathcal{U}} \mathcal{R}(\mathcal{F}(m), m) \in B(\mathcal{U}, \mathcal{V})$ and $\partial_{\mathcal{H}_\mu} \mathcal{R}(\mathcal{F}(m), m) \in B(\mathcal{H}_\mu, \mathcal{V})$ respectively. In particular, the implicit function theorem [71] implies the following relations:

$$\begin{aligned} D_{\mathcal{H}_\mu} \mathcal{F}(m) \delta m &= - \underbrace{(\partial_{\mathcal{U}} \mathcal{R}(\mathcal{F}(m), m))^{-1}}_{\delta v \mapsto \delta u} \underbrace{\partial_{\mathcal{H}_\mu} \mathcal{R}(\mathcal{F}(m), m) \delta m}_{\delta m \mapsto \delta v}, & \text{(Linearized forward sensitivity)} \\ D_{\mathcal{H}_\mu} \mathcal{F}(m)^* \delta u &= - \underbrace{\partial_{\mathcal{H}_\mu} \mathcal{R}(\mathcal{F}(m), m)^*}_{\delta v \mapsto \delta m} \underbrace{(\partial_{\mathcal{U}} \mathcal{R}(\mathcal{F}(m), m)^*)^{-1}}_{\delta u \mapsto \delta v} \delta u, & \text{(Adjoint sensitivity)} \end{aligned}$$

where $\delta v \in \mathcal{V}$ indicates a variation in the PDE residual or, equivalently, an adjoint variable. Evaluating the action of $D_{\mathcal{H}_\mu} \mathcal{F}(m)$ requires solving the linearized PDE problem for $\delta v \mapsto \delta u$, and evaluating its adjoint action $D_{\mathcal{H}_\mu} \mathcal{F}(m)^*$ requires solving the linear adjoint problem for $\delta u \mapsto \delta v$.

The associated computational cost for generating n_t training samples at parameter samples $m_j \stackrel{\text{i.i.d.}}{\sim} \mu$, $j = 1 \dots n_t$, can be decomposed as follows:

1 × Cost of reduced bases estimation
+ $n_t \times$ Cost of a PDE solve
+ $n_t \times$ Cost of evaluating the reduced Jacobian \mathbf{J}_r
= Cost of sample generation for DINO training

When compared to L_μ^2 training of an operator surrogate, DINO training requires additionally forming reduced Jacobian matrices $\mathbf{J}_r(m_j) \in \mathbb{R}^{d_y \times r}$ at each parameter sample m_j via rows or columns. In [Table 1](#) and the following paragraph, we provide a simple cost analysis for this task when the parameter and the state space are discretized.

For time-evolving problems, we assume the state space \mathcal{U} is discretized such that \mathcal{U}^h is isomorphic to $\mathbb{R}^{d_t \times d_u}$, where d_t is the dimension of the temporal discretization and d_u is the dimension of the spatial discretization. We assume such discretization leads to d_t systems of equations (linear PDE) or d_t iterative systems of equations (nonlinear PDE) of size $d_u \times d_u$. For steady-state problems, we simply take $d_t = 1$. When a direct solver is used, the cost of factorizing systems of equations for a typical PDE problem is $O(d_t d_u^{3/2})$ and $O(d_t d_u^2)$ for 2D and 3D spatial domains, while back-substitution has a cost of $O(d_t d_u \ln d_u)$ [72]. The factorization used for solving a linear PDE can be reused to form $\mathbf{J}_r(m_j)$ via back-substitution, making the additional cost of H_μ^1 training sample generation scale much slowly with d_u compared to the cost of L_μ^2 training. When an iterative solver is used, one can reuse preconditioners for a linear PDE to form $\mathbf{J}_r(m_j)$, but their cost analysis should be performed on a case-by-case basis. For nonlinear PDEs, one needs to solve one linear system of equations with $\min\{r, d_y\}$ different right-hand side vectors to form $\mathbf{J}_r(m_j)$, which is potentially much cheaper than solving a highly nonlinear PDE problem via iterative methods such as the Newton–Rapshon method.

4.4. Neural operator approximation error

This subsection briefly discusses approximation error for reduced basis DINO surrogates. To the best of our knowledge, there are no existing theoretical studies on H_μ^1 approximation error with input dimension reduction. We focus on theoretical results that isolate various sources of L_μ^2 approximation error under the

Forming a reduced Jacobian matrix $\mathbf{J}_r(m_j) \in \mathbb{R}^{d_y \times r}$		
Linearized forward sensitivity:		$\text{column}_l(\mathbf{J}_r(m_j)) = \mathbf{V}^* D_{\mathcal{H}_\mu} \mathbf{G}(m_j) \psi_l, \quad l = 1 \dots r.$
Adjoint sensitivity:		$\text{row}_k(\mathbf{J}_r(m_j)) = \Psi_r^* D_{\mathcal{H}_\mu} \mathbf{G}(m_j)^* \mathbf{v}_k, \quad k = 1 \dots d_y.$
Linear	Solver	Operation ($d_t = 1$ for steady-state problems)
✓	Direct	$d_t \times \min\{d_y, r\} \times$ Back-substitution (note: significant cost saving from reusing factorization)
	Iterative	$d_t \times \min\{d_y, r\} \times$ Iterative solve (note: significant cost saving from reusing preconditioner)
✗	Direct	$d_t \times$ Factorization + $d_t \times \min\{d_y, r\} \times$ Back-substitution
	Iterative	$d_t \times$ Preconditioner build + $d_t \times \min\{d_y, r\} \times$ Iterative solve

Table 1: The cost analysis of forming reduced Jacobian matrix $\mathbf{J}_r(m)$ at a parameter sample m_j given parameter reduced bases $\{\psi_j\}_{j=1}^\infty$ and observable basis $\{\mathbf{v}_j\}_{j=1}^{d_y}$.

assumption that the true mapping lives in H_μ^1 and comment on the relation between neural network size and the L_μ^2 approximation error.

Understanding the L_μ^2 approximation error of the operator surrogate is important as it dictates the efficiency of the DA procedure. Recall from [Section 2.8](#) that the proposal acceptance rate in the second stage of the DA MCMC reflects the quality of the generated Markov chain and the second stage acceptance probability is closely related to the error in surrogate data misfit evaluation, denoted by $\mathcal{E}_{\text{misfit}} : \mathcal{M} \rightarrow \mathbb{R}$:

$$\ln \rho^{(2)}(m_j, m^\dagger) = \mathcal{E}_{\text{misfit}}(m_j) - \mathcal{E}_{\text{misfit}}(m^\dagger), \quad \mathcal{E}_{\text{misfit}}(m) := \Phi^y(m) - \widetilde{\Phi^y}(m) \quad \mu\text{-a.e.}$$

where $\rho^{(2)}$ is the transition rate ratio of DA MCMC defined in [\(14\)](#). The arguments of $\rho^{(2)}$, namely m_j and m^\dagger , are coupled through the proposal and the first stage of DA MCMC, thus analyzing $\rho^{(2)}$ is not straightforward and is not the focus of this work. However, the error analysis for surrogate data misfit evaluation provides insights into the behavior of $\rho^{(2)}$ and the efficiency of DA MCMC related to the operator surrogate approximation error. In particular, the $L_{\mu^y}^1(\mathcal{M})$ approximation error of the surrogate data misfit (averaged over the true posterior) is controlled by the surrogate approximation error (averaged over the prior):

$$\|\mathcal{E}_{\text{misfit}}\|_{L_{\mu^y}^1(\mathcal{M})} := \mathbb{E}_{M \sim \mu^y} |\Phi^y(M) - \widetilde{\Phi^y}(M)| \leq c_{\text{misfit}}(\mathbf{G}, \widetilde{\mathbf{G}}, \mathbf{y}, \mathbf{C}_n^{-1} \mu) \|\mathbf{G} - \widetilde{\mathbf{G}}\|_{L_\mu^2(\mathcal{M}; \mathcal{Y})}, \quad (25)$$

where $c_{\text{misfit}} > 0$ is a constant. See proof in [\[73, Theorem 1\]](#) and the form of c_{misfit} in [Appendix C](#).

Here, we provide results on the $L_\mu^2(\mathcal{M}; \mathcal{Y})$ approximation error of the DIS and KLE reduced basis neural operators. Our results show that a reduced basis architecture leads to approximation error contributions due to truncation and neural network approximation of the optimal reduced mapping. Such a mapping, denoted by \mathbf{G}_r , can be defined explicitly [\[65, Proposition 2.3\]](#) for a given set of linear encoders Ψ_r^* and decoder Ψ_r constructed as in [\(20\)](#).

$$\mathbf{G}_r(m) := \mathbb{E}_{M \sim \mu} [\mathbf{G}(\Psi_r \Psi_r^* m + (\mathcal{I}_{\mathcal{M}} - \Psi_r \Psi_r^*) M)], \quad (\text{Subspace } L_\mu^2 \text{ projection}) \quad (26a)$$

$$\|\mathbf{G} - \mathbf{G}_r\|_{L_\mu^2(\mathcal{M}; \mathcal{Y})} = \inf_{\substack{\mathcal{T} : \mathcal{M} \rightarrow \mathcal{Y} \\ \text{Borel function}}} \|\mathbf{G} - \mathcal{T} \circ \Psi_r \Psi_r^*\|_{L_\mu^2(\mathcal{M}; \mathcal{Y})}. \quad (\text{Optimal reduced mapping}) \quad (26b)$$

The following propositions extend the results on DIS and KLE subspace by Zahm et. al [\[65, Proposition 2.6 and 3.1\]](#) to a function space setting using the Poincaré inequality in [Theorem 3.2](#). The proofs are provided in [Appendix C](#).

Proposition 4.1 (L^2_μ approximation error: Derivative-informed subspace). Assume $\mathcal{G} \in H^1_\mu(\mathcal{M}; \mathcal{Y})$. Let $\{(\lambda_j^{\text{DIS}}, \psi_j^{\text{DIS}})\}_{j=1}^\infty$ and $\{(\widehat{\lambda}_j^{\text{DIS}}, \widehat{\psi}_j^{\text{DIS}})\}_{j=1}^\infty$ be the \mathcal{H}_μ -orthonormal eigenpairs of the expected ppGNH $\mathbb{E}_{M \sim \mu}[\mathcal{H}(M)]$ in (22) and its estimator $\widehat{\mathcal{H}}$ in (23) with decreasing eigenvalues. Following (21), we design a reduced basis neural operator architecture using a linear encoder $\widehat{\Psi}_r^{\text{DIS}^*} \in \text{HS}(\mathcal{M}, \mathbb{R}^{d_y})$ based on $\{\widehat{\psi}_j^{\text{DIS}}\}_{j=1}^r$ as in (20) and any \mathcal{Y} -orthonormal basis $\mathbf{V} \in \text{HS}(\mathbb{R}^{d_y}, \mathcal{Y})$:

$$\tilde{\mathcal{G}}(\cdot; \mathbf{w}) := \mathbf{V} \circ \mathbf{f}_{\text{NN}}(\cdot, \mathbf{w}) \circ \widehat{\Psi}_r^{\text{DIS}^*}.$$

The following decomposed upper bound hold for $L^2_\mu(\mathcal{M}; \mathcal{Y})$ approximation error between such a reduced basis operator surrogate and the target mapping \mathcal{G} :

$$\begin{aligned} \|\mathcal{G} - \tilde{\mathcal{G}}(\cdot; \mathbf{w})\|_{L^2_\mu(\mathcal{M}; \mathcal{Y})} &\leq \overbrace{\left\| \mathbf{f}_{\text{NN}}(\cdot, \mathbf{w}) - \mathbf{V}^* \circ \mathcal{G}_r \circ \widehat{\Psi}_r^{\text{DIS}} \right\|_{L^2_{\mathcal{N}(\mathbf{0}, \mathbf{I}_r)}(\mathbb{R}^r; \mathbb{R}^{d_y})}}^{\text{Neural network error}} \\ &\quad + \underbrace{\left(\sum_{j=r+1}^\infty \lambda_j^{\text{DIS}} \right)}_{\text{Basis truncation error}} \underbrace{\left(2r \left\| \mathbb{E}_{M \sim \mu}[\mathcal{H}(M)] - \widehat{\mathcal{H}} \right\|_{B(\mathcal{H}_\mu)} \right)^{1/2}}_{\text{Sampling error}}, \end{aligned}$$

where $\widehat{\Psi}_r^{\text{DIS}} \in \text{HS}(\mathbb{R}^r, \mathcal{M})$ is the linear decoder based on $\{\widehat{\psi}_j^{\text{DIS}}\}_{j=1}^r$ as in (20), and \mathcal{G}_r is the optimal reduced mapping of \mathcal{G} in (26).

Proposition 4.2 (L^2_μ approximation error: Karhunen–Loéve expansion subspace). Assume that $\mathcal{G} \in H^1(\mathcal{M}; \mathcal{Y})$ is Lipschitz continuous with a Lipschitz constant $c_{\mathcal{G}} \geq 0$, i.e.,

$$\|\mathcal{G}(m_1) - \mathcal{G}(m_2)\|_{C_n^{-1}} \leq c_{\mathcal{G}} \|m_1 - m_2\|_{\mathcal{M}} \quad \forall m_1, m_2 \in \mathcal{M}.$$

Let $\{(\lambda_j^{\text{KLE}}, \eta_j)\}_{j=1}^\infty$ be the \mathcal{M} -orthonormal eigenpairs of \mathcal{C}_{pr} with decreasing eigenvalues. Following (21), we design a reduced basis neural operator architecture using a linear encoder $\widehat{\Psi}_r^{\text{KLE}^*} \in \text{HS}(\mathcal{M}, \mathbb{R}^{d_y})$ based on $\{\psi_j^{\text{KLE}} := \sqrt{\lambda_j^{\text{KLE}}} \eta_j\}_{j=1}^r$ as in (20) and any \mathcal{Y} -orthonormal basis $\mathbf{V} \in \text{HS}(\mathbb{R}^{d_y}, \mathcal{Y})$:

$$\tilde{\mathcal{G}}(\cdot; \mathbf{w}) := \mathbf{V} \circ \mathbf{f}_{\text{NN}}(\cdot, \mathbf{w}) \circ \widehat{\Psi}_r^{\text{KLE}^*}.$$

The following decomposed upper bound hold for $L^2_\mu(\mathcal{M}; \mathcal{Y})$ approximation error between such a reduced basis operator surrogate and the target mapping \mathcal{G} :

$$\begin{aligned} \|\mathcal{G} - \tilde{\mathcal{G}}(\cdot; \mathbf{w})\|_{L^2_\mu(\mathcal{M}; \mathcal{Y})} &\leq \underbrace{\left\| \mathbf{f}_{\text{NN}} - \mathbf{V}^* \circ \mathcal{G}_r \circ \widehat{\Psi}_r^{\text{KLE}} \right\|_{L^2_{\mathcal{N}(\mathbf{0}, \mathbf{I}_r)}(\mathbb{R}^r; \mathbb{R}^{d_y})}}_{\text{Neural network error}} + c_{\mathcal{G}} \underbrace{\left(\sum_{j=r+1}^\infty (\lambda_j^{\text{KLE}})^2 \right)^{1/2}}_{\text{Basis truncation error}}, \end{aligned}$$

where $\widehat{\Psi}_r^{\text{KLE}} \in \text{HS}(\mathbb{R}^r, \mathcal{M})$ is the linear decoder based on $\{\psi_j^{\text{KLE}}\}_{j=1}^r$ as in (20) and \mathcal{G}_r is the optimal reduced mapping of \mathcal{G} in (26). Additionally, we have

$$\sum_{j=r+1}^\infty \lambda_j^{\text{DIS}} \leq c_{\mathcal{G}}^2 \sum_{j=r+1}^\infty (\lambda_j^{\text{KLE}})^2.$$

where $\{\lambda_j^{\text{DIS}}\}_{j=1}^\infty$ consists of decreasing eigenvalues of the expected ppGNH $\mathbb{E}_{M \sim \mu}[\mathcal{H}(M)]$ in (22).

Furthermore, universal approximation theories of neural networks can help us understand the expressiveness of the neural network architecture (e.g., width, breadth, and activation functions) used in reduced

basis neural operator surrogates. An important question is the neural network size, measured by the size of the weight d_w , needed to achieve a given neural network error tolerance. Schwab and Zech [74, Theorem 4.7] establish exponential convergence in $L^2_{\mathcal{N}(\mathbf{0}, \mathbf{I}_r)}(\mathbb{R}^r; \mathbb{R})$ for approximating certain analytic functions by deep neural networks with the ReLU activation function. Their theoretical results can be directly applied to the neural network error in our setting by stacking \mathbb{R}^{d_y} of these deep neural networks to form an output space of \mathbb{R}^{d_y} , given the optimal reduced mapping \mathcal{G}_r is sufficiently regular. Using this construction, the convergence rate derived by Schwab and Zech is scaled linearly by d_y .

5. Geometric MCMC via reduced basis neural operator

This section derives dimension-independent geometric MCMC methods with proposals entirely generated by a trained reduced basis neural operator. This work focuses on the mMALA method introduced in Section 2.7 and approximates all components in the mMALA proposal using the surrogate. We note that the derivation in this section is similar to the DR- ∞ -mMALA method in [16], except that our derivation (i) does not involve prior covariance factorization⁶, (ii) does not distinguish between KLE and DIS reduced bases, and (iii) involves the reduced basis neural operator introduced in (21).

5.1. Surrogate approximation

Given a trained neural network $\mathbf{f}_{\text{NN}}(\cdot; \mathbf{w}^\dagger)$ as in (21), we can approximate the data misfit in (3) with $\widetilde{\Phi}^y(\cdot; \mathbf{w}^\dagger) \approx \Phi^y$,

$$\widetilde{\Phi}^y(m) \equiv \widetilde{\Phi}_r^y(\Psi_r^* m), \quad (\text{Data misfit}) \quad (27a)$$

$$\widetilde{\Phi}_r^y(\mathbf{m}_r) := \frac{1}{2} \|\mathbf{V}^* \mathbf{y} - \mathbf{f}_{\text{NN}}(\mathbf{m}_r)\|^2, \quad (\text{Reduced data misfit}) \quad (27b)$$

the ppg in (5) with $D_{\mathcal{H}_\mu} \widetilde{\Phi}^y(\cdot; \mathbf{w}^\dagger) \approx D_{\mathcal{H}_\mu} \Phi^y$,

$$D_{\mathcal{H}_\mu} \widetilde{\Phi}^y(m) \equiv \Psi_r \widetilde{\mathbf{g}}_r(\Psi_r^* m). \quad (\text{ppg}) \quad (28a)$$

$$\mathbb{R}^r \ni \widetilde{\mathbf{g}}_r(\mathbf{m}_r) := \partial_{\mathbf{m}_r} \mathbf{f}_{\text{NN}}(\mathbf{m}_r)^T (\mathbf{V}^* \mathbf{y} - \mathbf{f}_{\text{NN}}(\mathbf{m}_r)), \quad (\text{Reduced ppg}) \quad (28b)$$

and the ppGNH in (6) with $\widetilde{\mathcal{H}}(\cdot; \mathbf{w}^\dagger) \approx \mathcal{H}$,

$$\widetilde{\mathcal{H}}(m) \equiv \Psi_r \widetilde{\mathbf{H}}_r(\Psi_r^* m) \Psi_r^* \quad (\text{ppGNH}) \quad (29a)$$

$$\mathbb{R}^{r \times r} \ni \widetilde{\mathbf{H}}_r(\mathbf{m}_r) := (\partial_{\mathbf{m}_r} \mathbf{f}_{\text{NN}}(\mathbf{m}_r))^T \partial_{\mathbf{m}_r} \mathbf{f}_{\text{NN}}(\mathbf{m}_r). \quad (\text{Reduced ppGNH}) \quad (29b)$$

5.2. Surrogate prediction of posterior local geometry

An eigendecomposition of the surrogate reduced ppGNH $\widetilde{\mathbf{H}}_r(\mathbf{m}_r)$ with $\mathbf{m}_r = \Psi_r^* m$ is computed at the beginning of each step in the MH algorithm. Such an eigendecomposition is necessary for fast evaluations of multiple terms in the transition rate ratio (12). We denote the eigendecomposition of the surrogate reduced ppGNH as

$$\widetilde{\mathbf{H}}_r(\mathbf{m}_r) = \widetilde{\mathbf{P}}_r(\mathbf{m}_r) \widetilde{\mathbf{D}}_r(\mathbf{m}_r) \widetilde{\mathbf{P}}_r(\mathbf{m}_r)^T, \quad \begin{cases} \widetilde{\mathbf{P}}_r(\mathbf{m}_r)^T \widetilde{\mathbf{P}}_r(\mathbf{m}_r) = \mathbf{I}_r; \\ \left(\widetilde{\mathbf{D}}_r(\mathbf{m}_r) \right)_{jk} = \widetilde{d}_j(\mathbf{m}_r) \delta_{jk}. \end{cases} \quad (30)$$

where $\widetilde{\mathbf{P}}_r(\mathbf{m}_r) \in \mathbb{R}^{r \times r}$ is a rotation matrix in \mathbb{R}^r with columns consist of eigenvectors and $\widetilde{\mathbf{D}}_r(\mathbf{m}_r) \in \mathbb{R}^{r \times r}$ is a diagonal matrix consists of eigenvalues $\{\widetilde{d}_j(\mathbf{m}_r)\}_{j=1}^r$. The rotation matrix nonlinearly depends on the

⁶We acknowledge that [16] utilizes \mathcal{H}_μ -orthonormal reduced bases, which means that the DR- ∞ -mMALA algorithm can be implemented without using prior factorization.

parameter m through \mathbf{m}_r , thus leading to a pair of position-dependent linear decoder and encoder as follows:

$$\widetilde{\Psi}_r(\mathbf{m}_r) := \Psi_r \widetilde{\mathbf{P}}_r(\mathbf{m}_r) \quad (\text{Position-dependent linear decoder}) \quad (31a)$$

$$\widetilde{\Psi}_r(\mathbf{m}_r)^* := \widetilde{\mathbf{P}}_r(\mathbf{m}_r)^T \Psi_r^* \quad (\text{Position-dependent linear encoder}) \quad (31b)$$

where the adjoint is taken in \mathcal{H}_μ similar to (20).

Remark 3. In the following presentation, we often omit the notation of position dependency for the encoder, decoder, rotation matrix, and eigenvalues of the ppGNH when there is no ambiguity. Moreover, we adopt the index notation of diagonal matrices as in (30) to explicitly reveal its structure.

Now, we may approximate the covariance of the local Gaussian approximation of the posterior in (4) as:

$$\widetilde{\mathcal{C}}_{\text{post}}(m) = \mathcal{C}_{\text{pr}} - \widetilde{\Psi}_r \left(\frac{\tilde{d}_j}{\tilde{d}_j + 1} \delta_{jk} \right) \widetilde{\Psi}_r^* \mathcal{C}_{\text{pr}}, \quad \widetilde{\mathcal{C}}_{\text{post}}(m)^{-1} = \mathcal{C}_{\text{pr}}^{-1} + \mathcal{C}_{\text{pr}}^{-1} \widetilde{\Psi}_r (\tilde{d}_j \delta_{jk}) \widetilde{\Psi}_r^*. \quad (32)$$

5.3. Sampling from the surrogate mMALA proposal

We consider the proposal distribution defined by the reduced basis neural operator with $\mathcal{K}(m) = \widetilde{\mathcal{C}}_{\text{post}}(m; \mathbf{w}^\dagger)$. By substituting the expression in (32) into (11), we arrive at the following form of the surrogate-based mMALA proposal:

$$\begin{aligned} \widetilde{\mathcal{Q}}_{\text{mMALA}}(m, \cdot) &= \mathcal{N} \left(sm + (1-s) \widetilde{\mathcal{A}}(m), (1-s^2) \widetilde{\mathcal{C}}_{\text{post}}(m) \right), \quad s = \frac{4 - \Delta t}{4 + \Delta t}, \\ \widetilde{\mathcal{A}}(m) &= \widetilde{\Psi}_r \left(\frac{\tilde{d}_j}{\tilde{d}_j + 1} \delta_{jk} \right) \widetilde{\Psi}_r^* m - \widetilde{\Psi}_r \left(\frac{1}{\tilde{d}_j + 1} \delta_{jk} \right) \widetilde{\mathbf{P}}_r^T \widetilde{\mathbf{g}}_r. \end{aligned}$$

To sample from the surrogate mMALA proposal, we consider the following lemma:

Lemma 5.1. Let $M \sim \mathcal{N}(0, \mathcal{C}_{\text{pr}})$, $m \in \mathcal{M}$ and $\mathcal{T} \in B(\mathcal{M})$. Then we have $m + \mathcal{T}M \sim \mathcal{N}(m, \mathcal{T}\mathcal{C}\mathcal{T}^*)$. Moreover, if Ψ_r and Ψ_r^* are a set of linear encoder and decoder defined using reduced \mathcal{H}_μ -ONBs of rank r as in (20), then

$$\Psi_r^* M \sim \mathcal{N}(\mathbf{0}, \mathbf{I}_r) \text{ and } (\mathcal{I}_{\mathcal{M}} - \Psi_r \Psi_r^*) M \perp \Psi_r \Psi_r^* M,$$

where \perp denotes pairwise independency of random elements.

Based on Lemma 5.1, the following proposition holds, which allows us to sample the surrogate mMALA proposal via splitting the proposal into two parts: a position-dependent one for the r -dimensional coefficients in the reduced bases and the pCN proposal in the complementary subspace of \mathcal{M} , $\text{Range}(\mathcal{I}_{\mathcal{M}} - \Psi_r \Psi_r^*)$.

Proposition 5.2. Given $m \in \mathcal{M}$ and $\Delta t > 0$, define two conditional distributions with $s := (4 - \Delta t)/(4 + \Delta t)$:

1. $M_\perp^\dagger \sim \mathcal{Q}_{\text{pCN}}(m, \cdot)$ following the pCN proposal distribution in (8a) given by

$$M_\perp^\dagger := sm + \sqrt{1 - s^2} M, \quad M \sim \mu.$$

2. $\mathbf{M}_r^\dagger \sim \pi_r(\cdot | \mathbf{m}_r = \Psi_r^* m)$, a r -dimensional conditional random vector given by

$$\mathbf{M}_r^\dagger := \widetilde{\mathbf{P}}_r \left(\frac{\tilde{d}_j + s}{\tilde{d}_j + 1} \delta_{jk} \right) \widetilde{\mathbf{P}}_r^T \mathbf{m}_r - \widetilde{\mathbf{P}}_r \left(\frac{1 - s}{\tilde{d}_j + 1} \delta_{jk} \right) \widetilde{\mathbf{P}}_r^T \widetilde{\mathbf{g}}_r + \widetilde{\mathbf{P}}_r \left(\left(\frac{1 - s^2}{\tilde{d}_j + 1} \right)^{1/2} \delta_{jk} \right) \mathbf{\Xi}. \quad (33)$$

where $\mathbf{\Xi} \sim \mathcal{N}(\mathbf{0}, \mathbf{I}_r)$ is independent of M . Then, we have

$$(\mathcal{I}_{\mathcal{M}} - \Psi_r \Psi_r^*) M_\perp^\dagger + \Psi_r \mathbf{M}_r^\dagger \sim \widetilde{\mathcal{Q}}_{\text{mMALA}}(m, \cdot).$$

See proofs of Lemma 5.1 and Proposition 5.2 in Appendix D. While using an operator surrogate for the position-dependent proposal sampling is novel, the idea of proposal splitting is common in dimension-independent MCMC methods; see, e.g., [15, 16, 43, 75].

5.4. Evaluating acceptance probabilities

The RN derivative $\tilde{\rho}_0(m_1, m_2; \mathbf{w}^\dagger)$ between the surrogate mMALA proposal $\widetilde{\mathcal{Q}_{\text{mMALA}}}(m_1, dm_2)$ and the pCN proposal $\mathcal{Q}_{\text{pCN}}(m_1, dm_2)$ can be efficiently evaluated using the trained neural network. Due to [Proposition 5.2](#), $\tilde{\rho}_0$ is constant in the complementary space of the reduced bases used in the operator surrogate. As a result, we may reduce the density (12) to a function in \mathbb{R}^r denoted as $\widetilde{\rho}_{0,r}(\cdot, \cdot; \mathbf{w}^\dagger) : \mathbb{R}^r \times \mathbb{R}^r \rightarrow \mathbb{R}_+$:

$$\widetilde{\rho}_0(m_1, m_2; \mathbf{w}^\dagger) \equiv \widetilde{\rho}_{0,r}(\Psi_r^* m_1, \Psi_r^* m_2; \mathbf{w}^\dagger). \quad (\text{Reduced RN derivative w.r.t. pCN})$$

The form of $\widetilde{\rho}_{0,r}$ is given by

$$\begin{aligned} \widetilde{\rho}_{0,r}(\mathbf{m}_1, \mathbf{m}_2) &:= \exp \left(-\frac{\Delta t}{8} \left\| (\tilde{d}_j \delta_{jk}) \widetilde{\mathbf{P}_r}^T \mathbf{m}_1 - \widetilde{\mathbf{P}_r}^T \widetilde{\mathbf{g}_r} \right\|_{(\tilde{d}_{j+1})^{-1} \delta_{jk}}^2 \right. \\ &\quad \left. + \frac{\sqrt{\Delta t}}{2} \widehat{\mathbf{m}}^T (\widetilde{\mathbf{H}_r} \mathbf{m}_1 - \widetilde{\mathbf{g}_r}) - \frac{1}{2} \|\widehat{\mathbf{m}}\|_{\widetilde{\mathbf{H}_r}}^2 \right) + \prod_{j=1}^r (\tilde{d}_j + 1)^{1/2}, \end{aligned}$$

where $\widehat{\mathbf{m}} := (\mathbf{m}_2 - s\mathbf{m}_1)/\sqrt{1-s^2}$. Here, the reduced ppg $\widetilde{\mathbf{g}_r}$, the reduced ppGNH $\widetilde{\mathbf{H}_r}$, and the ppGNH eigendecomposition $(\tilde{d}_j \delta_{jk}, \widetilde{\mathbf{P}_r})$ are defined in (28b), (29b) and (30) and evaluated at $\mathbf{m}_1 = \Psi_r^* m_1$ through the trained neural network.

Now the transition rate ratio for the surrogate mMALA proposal is given by

$$\widetilde{\rho}_{\text{mMALA}}(m_1, m_2) = \exp(\Phi^y(m_1) - \Phi^y(m_2)) \frac{\widetilde{\rho}_{0,r}(\Psi_r^* m_2, \Psi_r^* m_1)}{\widetilde{\rho}_{0,r}(\Psi_r^* m_1, \Psi_r^* m_2)}. \quad (34)$$

Here, the data misfit Φ is evaluated via the PtO map \mathcal{G} instead of the surrogate $\widetilde{\mathcal{G}}$. As a result, the MH algorithm generates Markov chains with the posterior μ^y as the stationary distribution. Such a transition rate ratio is used in one of our numerical examples ([Section 7.5.2](#) for NO-mMALA and DINO-mMALA listed in [Table 3](#)) for examining the quality of the surrogate mMALA proposal.

For the DA MCMC introduced in [Section 2.8](#), only the surrogate data misfit enters the first stage transition rate ratio, and, thus, it can be further reduced to \mathbb{R}^r :

$$\rho^{(1)}(m_1, m_2; \mathbf{w}^\dagger) \equiv \rho_r^{(1)}(\Psi_r^* m_1, \Psi_r^* m_2; \mathbf{w}^\dagger), \quad (35a)$$

$$\rho_r^{(1)}(\mathbf{m}_1, \mathbf{m}_2) := \exp(\widetilde{\Phi}_r^y(\mathbf{m}_1) - \widetilde{\Phi}_r^y(\mathbf{m}_2)) \frac{\widetilde{\rho}_{0,r}(\mathbf{m}_2, \mathbf{m}_1)}{\widetilde{\rho}_{0,r}(\mathbf{m}_1, \mathbf{m}_2)}. \quad (35b)$$

When combined with the proposal splitting in [Proposition 5.2](#), such a reduction allows the first stage in the DA procedure to be performed entirely in reduced coefficient space \mathbb{R}^r , which means that prior sampling can be avoided until entering the second stage due to [Lemma 5.1](#). In the second stage, the true data misfit evaluated at the full proposal is required to maintain the posterior sampling consistency of MCMC:

$$\rho^{(2)}(m_1, m_2; \mathbf{w}^\dagger) = \frac{\exp(-\widetilde{\Phi}_r^y(\Psi_r^* m_j)) \exp(-\Phi^y(m^\dagger))}{\exp(-\widetilde{\Phi}_r^y(\Psi_r^* m^\dagger)) \exp(-\Phi^y(m_j))}. \quad (36)$$

It is noteworthy that (35b) allows for proposal rejection without true data misfit evaluation nor prior sampling. The additional cost reduction in prior sampling due to our choice of reduced basis architecture can be important, for example, when the prior is defined through Whittle–Matérn Gaussian random fields [76] that require solving fractional stochastic PDEs to sample. In [Algorithm 1](#), we summarize the procedure for our DA geometric MCMC method via a reduced basis neural operator surrogate.

Algorithm 1: Markov chain transition rule for the proposed MCMC method at the j -th position

Input: (i) trained neural network $\mathbf{f}_{\text{NN}}(\cdot, \mathbf{w}^\dagger)$, (ii) parameter encoder Ψ_r^* and decoder Ψ_r , (iii) observable basis \mathbf{V} , and (iv) step size Δt .

Known at m_j : (i) data misfit value: $\Phi^y(m_j)$, (ii) surrogate reduced data misfit value: $\widetilde{\Phi}_r^y(\mathbf{m}_r^{(j)})$, (iii) surrogate reduced ppg: $\widetilde{\mathbf{g}}_r(\mathbf{m}_r^{(j)})$, (iv) surrogate reduced ppGNH eigendecomposition: $(\widetilde{\mathbf{D}}_r(\mathbf{m}_r^{(j)}), \widetilde{\mathbf{P}}_r(\mathbf{m}_r^{(j)}))$.

Output: The next position $m_{j+1} \in \mathcal{M}$.

```

1 Sample  $\xi_r \stackrel{\text{i.i.d.}}{\sim} \mathcal{N}(\mathbf{0}, \mathbf{I}_r)$ ;
2 Compute  $\mathbf{m}_r^\dagger$  using  $\xi_r$  via (33);                                ▷ Reduced proposal sampling
3 Evaluate  $\mathbf{f}_{\text{NN}}$  and  $\partial_{\mathbf{m}_r} \mathbf{f}_{\text{NN}}$  at  $\mathbf{m}_r^\dagger$ ;
4 Compute  $\widetilde{\Phi}_r^y(\mathbf{m}_r^\dagger)$ ,  $\widetilde{\mathbf{g}}_r(\mathbf{m}_r^\dagger)$ ,  $\widetilde{\mathbf{D}}_r(\mathbf{m}_r^\dagger)$ , and  $\widetilde{\mathbf{P}}_r(\mathbf{m}_r^\dagger)$ ;      ▷  $\mathbb{R}^{r \times r}$  Hermitian eigenvalue problem
5 Compute  $\alpha^{(1)} = \min\{1, \rho_r^{(1)}(\mathbf{m}_r^{(j)}, \mathbf{m}_r^\dagger)\}$  via (35b);
6 if  $\alpha^{(1)} < \xi_1$  where  $\xi_1 \stackrel{\text{i.i.d.}}{\sim} \text{Uniform}([0, 1])$  then
7   return  $m_j$ ;                                              ▷ First stage rejection
8 else
9   Sample prior  $\mathbf{m}_\perp^\dagger \stackrel{\text{i.i.d.}}{\sim} \mu$ ;          ▷ Prior sampling in second stage
10  Compute  $\mathbf{m}^\dagger = \Psi_r \mathbf{m}_r^\dagger + \mathbf{m}_\perp^\dagger - \Psi_r \Psi_r^* \mathbf{m}_\perp^\dagger$ ;    ▷ Assemble the full proposal sample
11  Evaluate the data misfit  $\Phi^y(\mathbf{m}^\dagger)$ ;          ▷ Model simulation in second stage
12  Compute  $\alpha^{(2)} = \min\{1, \rho_r^{(2)}(m_j, \mathbf{m}^\dagger)\}$  via (36)
13  if  $\alpha^{(2)} < \xi_2$  where  $\xi_2 \stackrel{\text{i.i.d.}}{\sim} \text{Uniform}([0, 1])$  then
14    return  $m_j$ ;                                              ▷ Second stage rejection
15  else
16    return  $\mathbf{m}^\dagger$ ;                                              ▷ Second stage acceptance
17 end
18 end

```

6. Numerical examples: Baseline, chain diagnostics, efficiency metrics, and software

We numerically study our DINO-accelerated geometric MCMC method for two PDE-constrained Bayesian inverse problems in [Sections 7](#) and [8](#). In this section, we briefly introduce baseline MCMC methods to assess the efficiency of our proposed MCMC method. Then, we specify two diagnostics for assessing the quality of Markov chains generated by MCMC for posterior sampling. Next, we introduce two metrics that quantify the relative efficiency of two MCMC methods.

Posterior geometry information	Name	Gauss–Newton Hessian (6) (approximation)	Gradient (5)
None	pCN [24]	✗	✗
	MALA [44]	✗	✓
Fixed	LA-pCN [47, 50]	$\mathcal{H}(m_{\text{MAP}})$ in (6) and (37a)	✗
	DIS-mMALA [16, 43, 45]	$\widehat{\Psi}_r^{\text{DIS}} \widehat{\Lambda}_r^{\text{DIS}} \widehat{\Psi}_r^{\text{DIS}}^*$ in (24)	✓
Position-dependent	mMALA [15, 16]	\mathcal{H} in (6)	✓

Table 2: A list of baseline dimension-independent MCMC methods used in our numerical examples.

Operator learning loss function	Name	Reduced bases	Delayed acceptance	Reference method (38)
Conventional $L_\mu^2(\mathcal{M}; \mathcal{Y})$	NO-mMALA	DIS $r = 200$	✗	r-mMALA
	DA-NO-mMALA		✓	DA-r-mMALA
Derivative-informed $H_\mu^1(\mathcal{M}; \mathcal{Y})$	DINO-mMALA (ours)		✗	r-mMALA
	DA-DINO-mMALA (ours)		✓	DA-r-mMALA

Table 3: A list of operator surrogate-based dimension-independent geometric MCMC methods used in our numerical examples. We additionally introduce two reference methods, r-mMALA and DA-r-mMALA, that isolate the effects of reduced basis architecture in the empirical performance of operator surrogate-accelerated MCMC.

6.1. Baseline and reference MCMC methods

A table of baseline MCMC methods is listed in [Table 2](#). The mMALA method can be deduced from the generic mMALA proposal in [\(11\)](#) with $\mathcal{K}(m) = (\mathcal{I}_{\mathcal{H}_\mu} + \mathcal{H}(m))^{-1}\mathcal{C}_{\text{pr}}$ as in [\(6\)](#). This method is the same as ∞ -mMALA in [\[15, 16\]](#). The DIS-mMALA method uses the DIS approximation of $\mathbb{E}_{M \sim \mu}[\mathcal{H}(m)]$ in [\(24\)](#) as a fixed approximation to \mathcal{H} . This method is the same as DR- ∞ -mMALA in [\[16\]](#) with a fixed DIS reduced basis, similar to gpCN in [\[45\]](#) except that gpCN does not include ppg, similar to LI-Langevin in [\[43\]](#) except that (i) DIS-mMALA do not require prior covariance factorization and (ii) DIS-mMALA has only one step size parameter. The LA-pCN [\[47, 50\]](#) method utilizes the Laplace approximation to the posterior, which requires solving the following deterministic inverse problem for the maximum a posteriori probability (MAP) estimate [\[68, 77\]](#), denoted by $m_{\text{MAP}} \in \mathcal{H}_\mu$, to construct the proposal distribution

$$m_{\text{MAP}} := \arg \min_{m \in \mathcal{M}} \left(\Phi^y(m) + \frac{1}{2} \|m\|_{\mathcal{C}_{\text{pr}}^{-1}}^2 \right), \quad \mu^y \approx \mathcal{N}(m_{\text{MAP}}, \mathcal{C}_{\text{post}}(m_{\text{MAP}})), \quad (37a)$$

$$\mathcal{Q}_{\text{LA-pCN}}(m, \cdot) := \mathcal{N}(m_{\text{MAP}} - sm, (1 - s^2)\mathcal{C}_{\text{post}}(m_{\text{MAP}})). \quad (37b)$$

We note that $\mathcal{Q}_{\text{LA-pCN}}$ is reversible with respect to $\mathcal{N}(m_{\text{MAP}}, \mathcal{C}_{\text{post}}(m_{\text{MAP}}))$, which admits a RN derivative respect to the prior. As a result, the transition rate ratio for LA-pCN is well-defined with a closed form [\[47\]](#).

In [Table 3](#), we provide a list of MCMC methods driven by reduced basis neural operators detailed in [Section 5](#). The mMALA proposal approximated by both the L_μ^2 -trained NO and H_μ^1 -trained DINO with and without the DA procedure is studied in our numerical examples, and their efficiency is compared with the baseline methods.

When computationally feasible, we complement the numerical results of our proposed methods with those of two reference MCMC methods: r-mMALA (reduced-mMALA) and DA-r-MALA (reduced mMALA with delayed acceptance). These reference methods are designed to isolate the effects of the reduced basis architecture of DINO on the performance of DINO-accelerated geometric MCMC methods. They are defined via the following sample average approximation to the optimal reduced mapping [\(26\)](#) of the PtO map and its reduced Jacobian:

$$\mathcal{G}(m) \approx \sum_{j=1}^{n_{\text{rm}}} \mathcal{G}(\Psi_r \Psi_r^* m + (\mathcal{I}_{\mathcal{M}} - \Psi_r \Psi_r^*) m_j), \quad m_j \stackrel{\text{i.i.d.}}{\sim} \mu, \quad (38a)$$

$$\mathbf{J}_r(m) \approx \sum_{j=1}^{n_{\text{rm}}} \mathbf{V}^* D_{\mathcal{H}_\mu} \mathcal{G}(\Psi_r \Psi_r^* m + (\mathcal{I}_{\mathcal{M}} - \Psi_r \Psi_r^*) m_j) \Psi_r^*, \quad m_j \stackrel{\text{i.i.d.}}{\sim} \mu. \quad (38b)$$

The r-mMALA reference method replaces the PtO map and its parametric derivative in the mMALA proposal using [\(38\)](#). The DA-r-mMALA reference method additionally includes the DA procedure using [\(38a\)](#). We take $n_{\text{rm}} = 20$ in [Section 7](#).

6.2. Markov chain diagnostics

We focus on two diagnostics that help us understand the quality of Markov chains generated by MCMC: the multivariate potential scale reduction factor (MPSRF) and the effective sample size percentage (ESS%). In this subsection, we assume access to n_c number of independent Markov chains generated by the same MCMC method targeting the same posterior. Each chain has n_s samples (after burn-in), denoted by $\{\{m_{j,k}\}_{j=1}^{n_s}\}_{k=1}^{n_c}$.

6.2.1. Wasserstein multivariate potential scale reduction factor

The MPSRF [78] is a diagnostic for the convergence of MCMC. It compares the multi-chain mean of the empirical covariance within each chain, denoted as $\widehat{\mathcal{W}}_s \in B(\mathcal{M})$, and the empirical covariance across all chains, denoted as $\widehat{\mathcal{V}}_s \in B(\mathcal{M})$. They are given by

$$\widehat{\mathcal{W}}_s := \frac{1}{n_c(n_s - 1)} \sum_{k=1}^{n_c} \sum_{j=1}^{n_s} \langle m_{j,k} - \bar{m}_k, \cdot \rangle_{\mathcal{M}} (m_{j,k} - \bar{m}_k), \quad (39a)$$

$$\widehat{\mathcal{V}}_s := \frac{n_s - 1}{n_s} \widehat{\mathcal{W}}_s + \frac{n_c + 1}{n_c(n_s - 1)} \sum_{k=1}^{n_c} \langle \bar{m}_k - \bar{m}, \cdot \rangle_{\mathcal{M}} (\bar{m}_k - \bar{m}), \quad (39b)$$

where \bar{m}_k is the mean of samples in each chain labeled by $k = 1, \dots, n_{\text{chain}}$ and \bar{m} is the mean of samples in all chains. We expect the difference in $\widehat{\mathcal{W}}_s$ and $\widehat{\mathcal{V}}_s \in B(\mathcal{M})$ to be small as the chains become longer.

The MPSRF is typically defined as follows:

$$\widehat{R} = \sqrt{\max_{\substack{m \in \mathcal{M} \text{ s.t.} \\ \|m\|_{\mathcal{M}}=1}} \frac{\langle m, \widehat{\mathcal{W}}_s m \rangle_{\mathcal{M}}}{\langle m, \widehat{\mathcal{V}}_s m \rangle_{\mathcal{M}}}}. \quad (\text{Conventional MPSRF})$$

However, this quantity is not well-defined since the two empirical covariance operators are singular for a finite sample size n_s . During computation on a discretized parameter space, a pool of long MCMC chains is often needed to estimate this quantity. Moreover, the MPSRF characterizes Markov chains along a single slice of the parameter space, which is sufficient for monitoring convergence but insufficient for comparing the quality of Markov chains generated by different MCMC methods. In this work, we propose to use the 2-Wasserstein distance for Gaussian measures [79] to compare the distance between the two covariance operators. We refer to this diagnostic as Wasserstein MPSRF:

$$\begin{aligned} \widehat{R}_w &= \text{Wass}_2 \left(\mathcal{N}(0, \widehat{\mathcal{W}}_s), \mathcal{N}(0, \widehat{\mathcal{V}}_s) \right) \\ &= \text{Tr}_{\mathcal{M}} \left(\widehat{\mathcal{W}}_s + \widehat{\mathcal{V}}_s - 2(\widehat{\mathcal{W}}_s^{1/2} \widehat{\mathcal{V}}_s \widehat{\mathcal{W}}_s^{1/2})^{1/2} \right). \end{aligned} \quad (\text{Wasserstein MPSRF})$$

The faster \widehat{R}_w decays as the number of samples within each chain grows, the faster the pool of chains converges to their target distribution (i.e., faster mixing time).

6.2.2. Effective sample size percentage distribution

The ESS% [80] is the estimated percentage of independent samples from a pool of Markov chains. When each sample resides in 1D, such a metric is estimated using the autocorrelation function, denoted by $\text{AC}(t, k)$, of samples that are t positions apart within the k -th Markov chain:

$$\text{ESS\%} = \frac{1}{1 + 2 \sum_{t=1}^{2n'+1} \text{MAC}(t)}, \quad (\text{Effective sample size percentage}) \quad (40a)$$

$$\text{MAC}(t) = 1 - \frac{\widehat{w}_s - \frac{1}{n_c} \sum_{k=1}^{n_c} \text{AC}(t, k)}{\widehat{v}_s}, \quad (\text{Multichain autocorrelation time}) \quad (40b)$$

where MACT is the multi-chain AC estimate, \widehat{w}_s and \widehat{v}_s is the 1D version of (39). The index $n' \in \mathbb{Z}_+$ is chosen to be the largest integer so that the sum of MACT evaluated at neighboring positions is positive.

The simulated MCMC samples $m_{j,k}^h$ belong to a discretized function space \mathcal{M}^h of dimension d_m . Following [15, 16], we estimate such a 1D diagnostic metric for each degree of freedom (DoF) in the discretized space. This leads to a distribution of d_m ESS% estimates which will be visualized using violin plots.

6.3. Comparing efficiency of MCMC methods

In this subsection, we introduce two metrics that measure the relative efficiency of a pair of MCMC methods: effective sampling speedup and total effective sampling speedup.

6.3.1. Effective sampling speedup

The effective sampling speed quantifies the efficiency of an MCMC method regarding its speed of effective sample generation:

$$\text{Effective sampling speed} = \frac{\text{Median(ESS\%)}}{\text{Cost of 100 Markov chain samples}}. \quad (41)$$

Instead of directly computing this quantity, we use it to compare the relative efficiency of posterior sampling for different pairs of MCMC methods. The relative efficiency is measured by *the effective sampling speedup*, or speedup for short. It is given by the ratio between the effective sampling speed of the two methods.

6.3.2. Total effective sampling speedup

Training sample generation is an important part of the total computational cost for DINO-accelerated geometric MCMC methods, especially when the PtO map is expensive to evaluate. The cost of training sample generation is a fixed offline cost while the cost of posterior sampling scales with the number of MCMC samples. To incorporate both the offline training cost and the online MCMC cost, we introduce an efficiency metric called *the total effective sampling speed* as a function of the effective sample size n_{ess} required for an MCMC run:

$$\text{Total effective sampling speed}(n_{\text{ess}}) = \frac{n_{\text{ess}}}{\text{Total cost}(n_{\text{ess}})}, \quad (42)$$

$$\text{Total cost}(n_{\text{ess}}) = \text{Offline cost} + \text{Cost of 100 Markov chain samples} \times \frac{n_{\text{ess}}}{\text{Median(ESS\%)}}.$$

For DINO-mMALA and DA-DINO-mMALA, the offline cost is the sum of training sample generation and neural network training cost. Notice that the total effective sampling speed converges to the effective sampling speed when the offline cost is negligible compared to the cost of the MCMC run, i.e., $n_{\text{ess}} \rightarrow \infty$. Again, instead of directly computing this quantity, we use it to compare the relative efficiency of posterior sampling for different pairs of MCMC methods. The relative efficiency is measured by *the total effective sampling speed*, or total speedup for short. It is given by the ratio between the total effective sampling speed of the two methods at a given n_{ess} .

Remark 4. *In our numerical examples, we do not include the computational cost of step size tuning and burn-in in the total cost. We found that these costs can be significantly reduced if the Markov chain initial position is sampled from the Laplace approximation of the posterior instead of the prior. See Appendix E for our step size tuning and chain initialization procedure.*

6.4. Software

Our numerical examples are implemented through (i) **FEniCS** [81, 82] for finite element discretization, solves, and symbolic differentiation of PDE problem, (ii) **hIPPYlib** [68, 83] for all components related to inverse problems, e.g. the prior, adjoint solves, Laplace approximation, and some baseline MCMC methods (LA-pCN, MALA, and pCN), (iii) **hIPPYflow** [84] for reduced basis estimation and training sample

generation, and (iv) `dino` [85] for derivative-informed operator learning. The implementation and data are shared upon request.⁷.

7. Numerical example: Coefficient inversion for nonlinear diffusion–reaction PDE

We consider the following steady-state nonlinear diffusion–reaction equation in the unit square:

$$\begin{aligned} -\nabla \cdot \exp(m(\mathbf{x})) \nabla u(\mathbf{x}) + u(\mathbf{x})^3 &= 0, & \mathbf{x} \in (0, 1)^2; \\ u(\mathbf{x}) &= 0, & \mathbf{x} \in \Gamma_{\text{bottom}}; \\ u(\mathbf{x}) &= 1, & \mathbf{x} \in \Gamma_{\text{top}}; \\ \nabla u(\mathbf{x}) \cdot \mathbf{n} &= 0, & \mathbf{x} \in \Gamma_{\text{left}} \cup \Gamma_{\text{right}}; \end{aligned}$$

where Γ_{bottom} , Γ_{top} , Γ_{left} , and Γ_{right} are the boundaries the unit square. We seek to invert for the log-coefficient field m given noise-corrupted discrete observations of the PDE state variable u at a set of spatial positions.

This section is organized as follows. We introduce the prior, the PtO map, and the setting for Bayesian inversion in [Sections 7.1](#) to [7.3](#). Then, we present the specifications and results on training operator surrogates with conventional L^2_μ operator learning and the derivative-informed H^1_μ operator learning in [Section 7.4](#). Next, we showcase and analyze MCMC results in [Section 7.5](#). In [Section 7.5.1](#), we discuss results on the baseline methods listed in [Table 2](#). In [Section 7.5.2](#), we discuss results on NO-mMALA and DINO-mMALA listed in [Table 3](#) to understand the quality of surrogate mMALA proposals. In [Section 7.5.3](#), we discuss results on DA-NO-mMALA and DA-DINO-mMALA listed in [Table 3](#).

7.1. The prior distribution

We consider the following parameter space and prior distribution

$$\begin{aligned} \mathcal{M} &:= L^2((0, 1)^2), & \text{(Parameter space)} \\ \mu &:= \mathcal{N}(0, (-\gamma\Delta + \delta\mathcal{I}_{\mathcal{M}})^{-2}), & \text{(The prior distribution)} \end{aligned}$$

where $-\Delta : H^1((0, 1)^2) \rightarrow H^1((0, 1)^2)'$ is the weak Laplace operator with a Robin boundary condition for eliminating boundary effects [68, Equation 37]. The constants $\gamma, \delta \in \mathbb{R}_+$ are set to $\gamma = 0.03$ and $\delta = 3.33$, which approximately leads to a pointwise variance of 9 and spatial correlation length of 0.1. For numerical computation, we approximate \mathcal{M} using a finite element space \mathcal{M}^h constructed by linear triangular elements with 1,681 DoFs. We provide a visualization of prior samples in [Figure 3](#).

7.2. The parameter-to-observable map

We consider a symmetric variational formulation of the PDE problem. We define the following Hilbert spaces following the notation in [Section 4.3](#):

$$\begin{aligned} \mathcal{U} &:= \left\{ u \in H^1((0, 1)^2) \mid u|_{\Gamma_t} = 0 \wedge u|_{\Gamma_b} = 0 \right\}; & \text{(State space)} \\ \mathcal{V} &:= \mathcal{U}', & \text{(Residual space)} \end{aligned}$$

where \mathcal{U}' denotes the dual space of \mathcal{U} . To enforce the inhomogeneous Dirichlet boundary condition, we decompose the PDE solution u into $u = u_0 + \mathbf{x}^T \mathbf{e}_2$, where $\mathbf{e}_2 = [0 \ 1]^T$ and $u_0 \in \mathcal{U}$ is the PDE state with the homogenous Dirichlet boundary condition.

The residual operator for this PDE problem, denoted as $\mathcal{R} : \mathcal{U} \times \mathcal{M} \rightarrow \mathcal{V}$, can be defined by its action on an arbitrary test function $p \in \mathcal{U}$

$$\langle \mathcal{R}(u_0, m), p \rangle_{\mathcal{U}' \times \mathcal{U}} := \int_{(0, 1)^2} \left(\exp(m(\mathbf{x})) (\nabla u_0(\mathbf{x}) + \mathbf{e}_2) \cdot \nabla p(\mathbf{x}) + (u_0(\mathbf{x}) + \mathbf{x}^T \mathbf{e}_2)^3 p(\mathbf{x}) \right) d\mathbf{x}. \quad (44)$$

⁷Public release of the code and data is contingent on acceptance for journal publication.

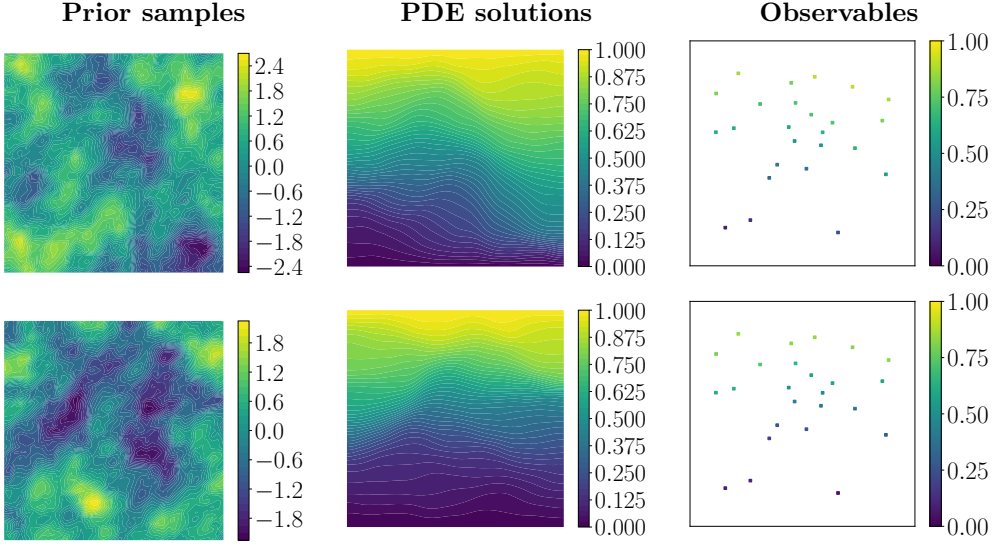


Figure 3: Visualizations of prior samples (1681 DoFs), PDE solutions (3362 DoFs), and predicted observables (in \mathbb{R}^{25}) for coefficient inversion in a nonlinear diffusion–reaction PDE.

We thus define the effective PDE solution operator as a nonlinear parameter-to-state map $\mathcal{F} : \mathcal{M} \ni m \mapsto u_0 \in \mathcal{U}$ where $\mathcal{R}(u_0, m) = 0$. For numerical computation, we approximate \mathcal{U} using a finite element space \mathcal{U}^h constructed by quadratic triangular elements with 3,362 DoFs. Evaluating the discretized PDE solution operator involves solving the discretized residual norm minimization problem via the Newton–Raphson method in \mathcal{U}^h .

We define the observation operator \mathcal{O} using 25 randomly-sampled discrete interior points $\{\mathbf{x}_{\text{obs}}^{(j)}\}_{j=1}^{d_y}$ with $d_y = 25$:

$$\mathcal{O}(u_0) = \left[\int_{\mathbf{B}_\epsilon(\mathbf{x}_{\text{obs}}^{(1)})} u(\mathbf{x}) \, d\mathbf{x} \quad \dots \quad \int_{\mathbf{B}_\epsilon(\mathbf{x}_{\text{obs}}^{(25)})} u(\mathbf{x}) \, d\mathbf{x} \right]^T, \quad (\text{Observation operator}) \quad (45)$$

where $\mathbf{B}_\epsilon(\mathbf{x}) \subset (0, 1)^2$ is a ball around \mathbf{x} with a small radius $\epsilon > 0$. The PtO map is thus defined as $\mathcal{G} := \mathcal{O} \circ \mathcal{F}$. We visualize the output of the PtO map in Figure 3.

7.3. Bayesian inversion settings

We generate synthetic data for our Bayesian inverse problem using an out-of-distribution piecewise-constant parameter field, following the examples in [16, 43]. The model-predicted observable at the synthetic parameter field is then corrupted with 2% additive white noise, which leads to a noise covariance matrix of identity scaled by $v_n = 1.7 \times 10^{-4}$:

$$\pi_n = \mathcal{N}(\mathbf{0}, v_n \mathbf{I}). \quad (\text{Noise distribution})$$

We visualize the synthetic data, its generating parameter, and the MAP estimate in Figure 4.

7.4. Neural operator surrogates

We follow the procedure described in Section 4.3 for generating samples for neural network training and testing. Recall that each sample consists of an i.i.d. random parameter field, a model-predicted observable coefficient vector, and a reduced Jacobian matrix. We compute DIS reduced bases of dimension $r = 200$ using $n_{\text{DIS}} = 1,000$ of the generated samples as specified in (23). In particular, we generate the full Jacobian matrix instead of the reduced Jacobian matrix for the first 1,000 generated samples. Then, a generalized eigenvalue problem is solved to compute the DIS reduced bases [68, 84]. We visualize selected DIS basis

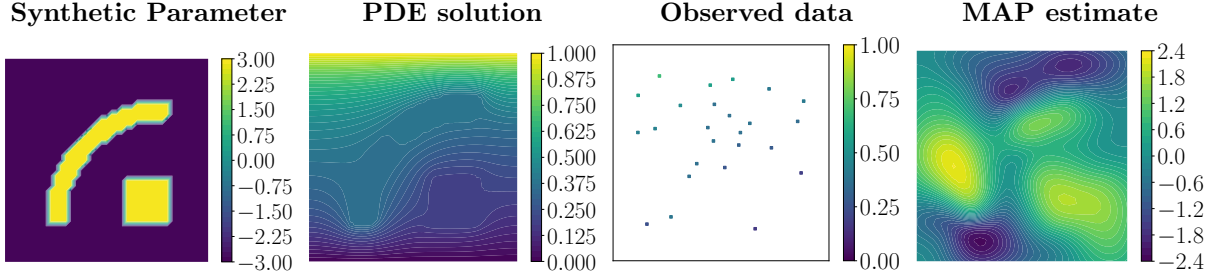


Figure 4: Visualization of the Bayesian inverse problem setting and the MAP estimate for coefficient inversion in a nonlinear diffusion-reaction PDE.

functions in [Figure F.19](#). Forming reduced Jacobian matrices via columns using a direct solver with reused factorization takes 25% of the computing time for solving the nonlinear PDEs using a direct solver, estimated on average over sample generation.

We use a dense neural network architecture with six hidden layers, each with 400 hidden neurons and a GELU activation function. We optimize for neural network weights (i) using either the conventional L^2_μ or derivative-informed H^1_μ operator learning objective specified in [\(15\)](#) and [\(17\)](#) and (ii) a varying number of training samples n_t for loss estimation specified in [\(16\)](#) and [\(18\)](#), with $n_t = 125, 250, \dots, 16,000$. We compute the generalization error of the trained operator surrogates based on their observable predictions and reduced Jacobian predictions. The two types of errors are measured using the relative L^2_μ error defined as follows:

$$\mathcal{E}_{\text{Obs}}(\mathcal{G}, \tilde{\mathcal{G}}) := \sqrt{\mathbb{E}_{M \sim \mu} \left[\frac{\|\mathcal{G}(M) - \tilde{\mathcal{G}}(M)\|_{C_n^{-1}}^2}{\|\mathcal{G}(M)\|_{C_n^{-1}}^2} \right]}, \quad \mathcal{E}_{\text{Jac}}(\mathbf{J}_r, \tilde{\mathbf{J}}_r) := \sqrt{\mathbb{E}_{M \sim \mu} \left[\frac{\|\mathbf{J}_r(M) - \tilde{\mathbf{J}}_r(M)\|_F^2}{\|\mathbf{J}_r(M)\|_F^2} \right]}. \quad (46)$$

The generalization accuracy is defined by $(1 - \mathcal{E}) \times 100\%$.

We estimate the generalization errors using 5,000 testing samples. In [Figure 5](#), we plot the estimated errors as a function of training sample generation cost, measured relative to the averaged cost of one nonlinear PDE solve. For L^2_μ -trained neural operators (NOs), we discount the cost of forming reduced Jacobian matrices; thus, its relative cost is the same as the number of training samples used for loss estimation. The error plot includes the relative cost of forming reduced Jacobian matrices for derivative-informed H^1_μ operator learning. Additionally, we provide generalization accuracy values on the error plot.

The plot shows that the derivative-informed H^1_μ operator learning significantly improves the quality of the surrogate at the same training sample generation cost compared to the conventional L^2_μ operator learning. Here is a list of important takeaways from this plot:

- To achieve the same generalization accuracy for either observable or reduced Jacobian prediction, the derivative-informed H^1_μ operator learning is at least 25 times more efficient than the conventional L^2_μ operator learning measured by training sample generation cost.
- In the small training sample size regime, e.g., $n_t < 1,000$, we find that derivative-informed H^1_μ operator learning leads to a much higher generalization error reduction rate for both observable prediction and reduced Jacobian prediction.
- To achieve a similar efficiency in posterior sampling compared to mMALA, the operator surrogate needs an estimated 90% generalization accuracy in reduced Jacobian prediction (see [Figure 10](#)). The conventional L^2_μ operator learning may at least (estimated via extrapolation) demand the cost of around 116,000 nonlinear PDE solves, while derivative-informed H^1_μ operator learning requires the cost of around 700 nonlinear PDE solves—two orders of magnitude difference in computational cost.

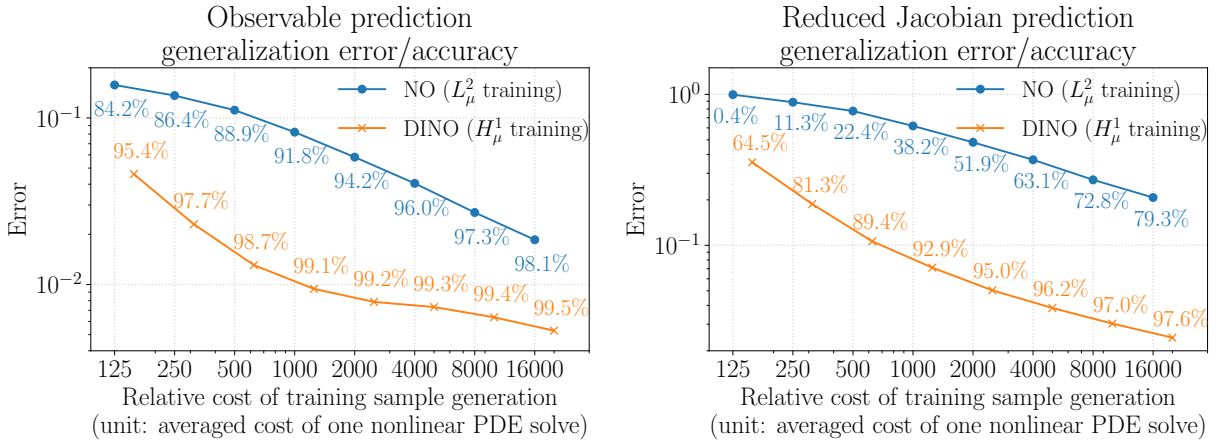


Figure 5: The generalization error and accuracy (46) of observable prediction and reduced Jacobian prediction made by L_μ^2 -trained neural operators and H_μ^1 -trained DINOs for coefficient inversion in a nonlinear diffusion–reaction PDE. The error is plotted as a function of training sample generation cost, measured relative to the averaged cost of one nonlinear PDE solve.

These numerical results indicate that the derivative-informed H_μ^1 operator learning provides a much superior cost-accuracy trade-off compared to the conventional L_μ^2 operator learning. The superiority of derivative-informed learning is more pronounced for large-scale PDE systems since one typically cannot afford to solve these systems at a large number of parameter samples. The superiority of derivative-informed H_μ^1 operator learning is decisive when one expects the trained operator to possess an accurate derivative with respect to a high or infinite-dimensional input.

7.5. MCMC Results

We present numerical results related to the efficiency of DINO-mMALA and DA-DINO-mMALA methods compared to the baseline and reference MCMC methods. For each method, we collect $n_c = 10$ Markov chains with different initialization, each with $n_s = 19,000$ samples (after burn-in). The step size parameter Δt and initialization are chosen carefully according to the procedure detailed in [Appendix E](#). We provide the statistics of the MCMC runs and posterior visualization in [Appendix F](#).

7.5.1. The baseline MCMC methods

In [Figure 6](#), we visualize the diagnostics for the baseline MCMC methods in [Table 2](#). The diagnostics show that mMALA produces Markov chains with the most effective posterior samples and the fastest mixing speed among the baseline methods. When comparing methods utilizing the same type of posterior geometry information (see [Table 2](#)), MALA is inferior to pCN, and DIS-mMALA is inferior to LA-pCN, even though both MALA and DIS-mMALA include gradient information in their proposal distributions. This result suggests the importance of accurate posterior local geometry information (i.e., data misfit Hessian approximation), without which including the gradient alone may lead to deteriorated Markov chain quality.

Comparing the median of ESS%, mMALA produced 15.7 and 2.3 times more effective samples than pCN and LA-pCN. However, each MCMC sample generated by mMALA is around 2.3 times⁸ more computationally costly than pCN and LA-pCN, which means that LA-pCN and mMALA generate effective posterior samples equally fast. We also provide the effective sampling speedups (41) of mMALA against other baseline methods in [Table 4](#).

⁸Major contributing factors to the extra cost at each sample m can be roughly decomposed into (1) forming a discretized Jacobian matrix $\mathbf{J}^h(m)$ via adjoint solves, (2) solving the eigenvalue problem for the operator $\mathbf{J}(m)\mathbf{J}(m)^T \in \mathbb{R}^{25 \times 25}$, and (3) forming the decoder via actions of the prior covariance operator on the encoder.

Speedup Baseline \	mMALA	DINO-mMALA $n_t = 2000$	DINO-mMALA $n_t = 16000$	DA-DINO-mMALA $n_t = 2000$	DA-DINO-mMALA $n_t = 16000$
pCN	6.8	11.9	14.3	26.5	59.8
MALA	9.4	16.5	19.6	30.6	82.7
LA-pCN	1	1.8	2.1	3.9	8.8
DIS-mMALA	5.1	8.9	10.7	19.9	44.9
NO-mMALA $n_t = 16000$	4.8	8.4	10.1	18.7	42.2
DA-NO-mMALA $n_t = 16000$	5	9	10.5	19.5	44

Table 4: The effective sampling speedup of mMALA, DINO-mMALA, and DA-DINO-mMALA against other baseline MCMC methods for coefficient inversion in a nonlinear diffusion–reaction PDE. The speedup measures the relative speed of generating effective samples for an MCMC method compared against another MCMC method; see (41).

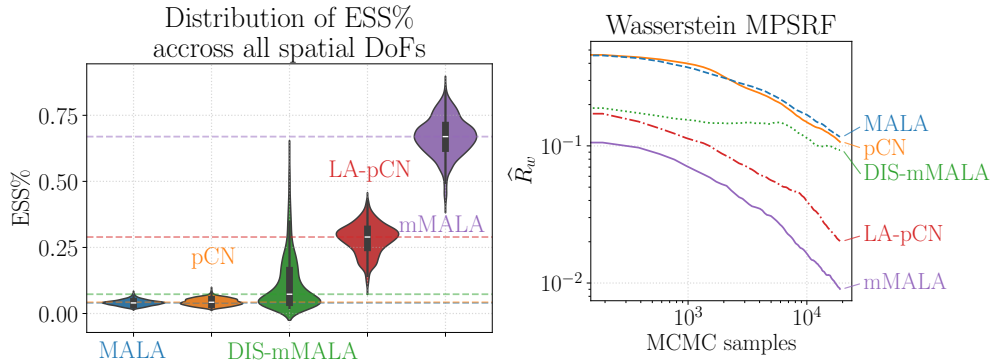


Figure 6: Visualization of the diagnostics (see Section 6.2) of MCMC chains generated by baseline methods listed in Table 2 for coefficient inversion in a nonlinear diffusion–reaction PDE. (left) The violin plot of the ESS% distributions over 1,681 spatial DoFs for the discretized parameter space. (left) The Wasserstein MPSRF as a function of the Markov chain position.

7.5.2. Geometric MCMC with operator surrogate proposal

For this part of the numerical results, we focus on the quality of the operator surrogate proposal by switching off the delayed acceptance and using the model-predicted data misfit to compute acceptance probability during MCMC; see (34). In Figure 7, we visualize the diagnostics of Markov chains generated by NO-mMALA, DINO-mMALA, r-mMALA, and baseline methods.

The diagnostics show that DINO-mMALA at $n_t = 2,000$ and beyond outperforms LA-pCN regarding the effective sample size and mixing speed of MCMC chains. At $n_t = 16,000$, the ESS% of DINO-mMALA is close to the baseline mMALA. Measured by the median ESS%, DINO-mMALA retains 91% of mMALA's effective sample size despite the presence of errors specified in Proposition 4.1. Estimated by the median ESS% of r-mMALA, the basis truncation and sampling error accounts for 13% of this drop in ESS%. After including the extra computational cost of mMALA at each MCMC sample, we observe that DINO-mMALA at $n_t = 16,000$ generates effective samples more than twice as fast as mMALA. See the speedups of DINO-mMALA against other methods in Table 4. These results suggest that DINO-predicted posterior local geometry is sufficiently accurate for improving the quality–cost trade-off of geometric MCMC.

The diagnostics of chains generated by NO-mMALA at $n_t = 16,000$ implies that MCMC driven by L_μ^2 -trained NOs lead to low posterior sampling efficiency. While the median ESS% of NO-mMALA at $n_t = 16,000$ is 1.4 times that of pCN, it is merely 11% of the median ESS% of DINO-mMALA at $n_t = 16,000$. Recall that L_μ^2 -trained NO at $n_t = 16,000$ has an estimated 98.1% and 79.3% generalization accuracy in observable and reduced Jacobian prediction; see Figure 5. However, to outperform LA-pCN in terms of ESS%

for solving this Bayesian inverse problem, the reduced Jacobian prediction accuracy needs to be around 90% (i.e., $n_t \approx 1000$ for H_μ^1 -trained DINO), which would require L_μ^2 -trained NO at least $n_t = 116,000$ to achieve; see comments in [Section 7.4](#).

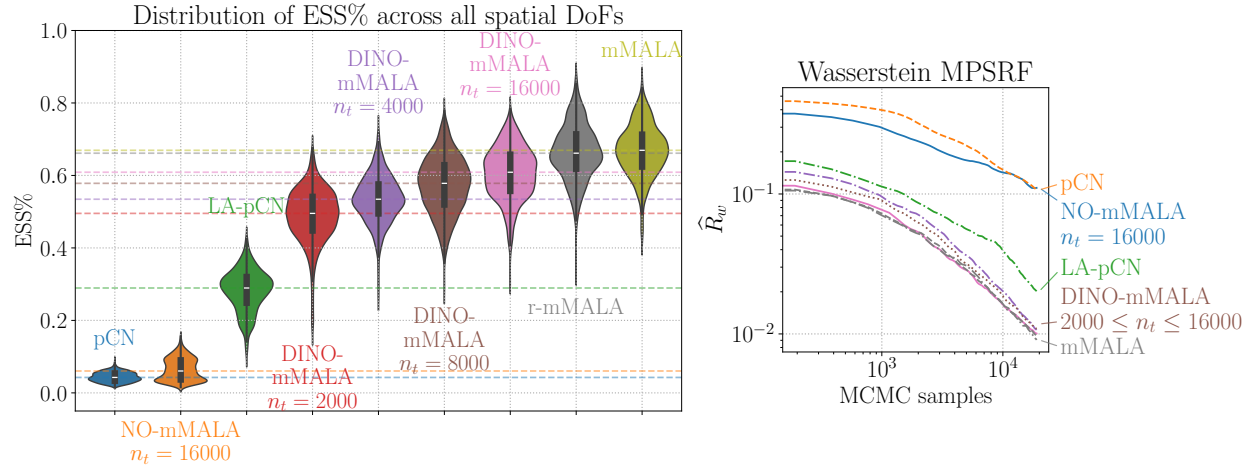


Figure 7: The diagnostics (see [Section 6.2](#)) of Markov chains generated by DINO-mMALA (H_μ^1 -trained surrogate proposal), NO-mMALA method (L_μ^2 -trained surrogate proposal), and other baseline and reference MCMC methods in [Tables 2](#) and [3](#) for coefficient inversion in a nonlinear diffusion-reaction PDE. The symbol n_t denotes the training sample size for operator learning. (left) The ESS% diagnostic. (right) The Wasserstein MPSRF diagnostic.

7.5.3. Delayed acceptance geometric MCMC with operator surrogate proposal

In [Figure 8 \(left\)](#) and [Figure 9](#), we visualize the diagnostics of the Markov chains generated by delayed acceptance geometric MCMC with operator surrogate proposal; see [Algorithm 1](#). The diagnostics show that DA-DINO-mMALA at $n_t = 2,000$ and beyond outperforms LA-pCN regarding the effective sample size and mixing speed. Measured by the median ESS%, DINO-mMALA retains 73% of mMALA's effective sample size. Estimated by the ESS% of DA-r-mMALA, the basis truncation error accounts for approximately 36% of this drop in ESS%. After including the extra computational cost of mMALA at each MCMC sample and the cost reduction of the DA procedure, we observe that DA-DINO-mMALA at $n_t = 16,000$ generates effective samples around 9 times faster than mMALA.

When a L_μ^2 -trained operator surrogate is used, DA-NO-mMALA at $n_t = 16,000$ leads to effective sample size and mixing speed similar to pCN. After including the cost reduction of the DA procedure, DA-NO-mMALA at $n_t = 16,000$ generates effective samples 1.4 times faster than pCN. However, it is still 5 times slower than LA-pCN and mMALA. Furthermore, it is 19.5 and 44 times slower than DA-DINO-mMALA at $n_t = 2,000$ and 16,000. See the speedups of DA-DINO-mMALA and DA-NO-mMALA against other methods in [Table 4](#).

In [Figure 8 \(right\)](#), we visualize the proposal acceptance rate in the first and second stages of the DA procedure for both DA-DINO-mMALA and DA-NO-mMALA. Recall that a low proposal acceptance rate in the first stage leads to a low computational cost and a high proposal acceptance rate in the second stage is related to the accuracy of the surrogate approximation. The plot shows that DA-DINO-mMALA has a high second-stage acceptance rate, improving consistently as the training sample size grows. When comparing between L_μ^2 -trained NO and H_μ^1 -trained DINO, the second-stage acceptance rate for DA-NO-mMALA is half of the rate for DA-DINO-mMALA, and the first-stage acceptance rate for DA-NO-mMALA is around 3 times the rate for DA-DINO-mMALA.

In [Figure 10](#), we plot the total effective sampling speedups of DA-DINO-mMALA against DA-NO-mMALA at $n_t = 16,000$, pCN, LA-pCN and mMALA. Recall from [\(42\)](#) that the total speedups include the offline cost of operator surrogate training, and it is a function of the effective sample size requested for an MCMC run. The total speedups against LA-pCN and mMALA show that if one aims to collect more

than merely 10 effective posterior samples, then it is more cost-efficient to use DA-DINO-mMALA with $n_t = 1,000$. On the other hand, the asymptotic speedup as $n_{\text{ess}} \rightarrow \infty$ (i.e., the effective sampling speedup in Table 4) at $n_t = 1,000$ is relatively small. A better asymptotic speedup requires a better operator surrogate trained with more samples. At $n_t = 16,000$, we achieve an asymptotic speedup of 8.8 against LA-pCN and mMALA and one needs to collect merely 66 effective posterior samples to break even the offline cost.

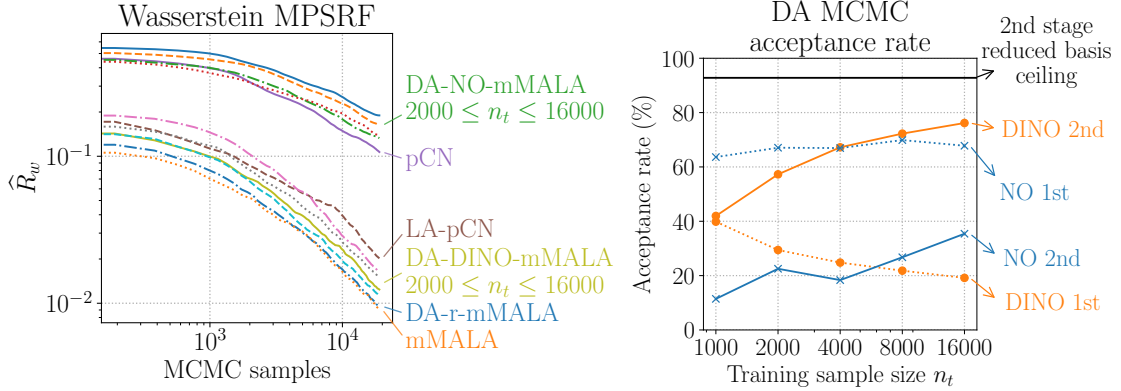


Figure 8: (left) The Wasserstein MPSRF diagnostic (see Section 6.2.1) of Markov chains generated by DA-DINO-mMALA (H_μ^1 -trained surrogate proposal with delayed acceptance), DA-NO-mMALA (L_μ^2 -trained surrogate proposal with delayed acceptance), and other baseline and reference MCMC methods for coefficient inversion in a nonlinear diffusion–reaction PDE. (right) The proposal acceptance rate in the first and second stages of the DA procedure as a function of training sample size. The reduced basis ceiling indicates the estimated (via DA-r-mMALA in Table 3) optimal second-stage acceptance rate for the reduced basis architecture with $r = 200$ DIS reduced bases.

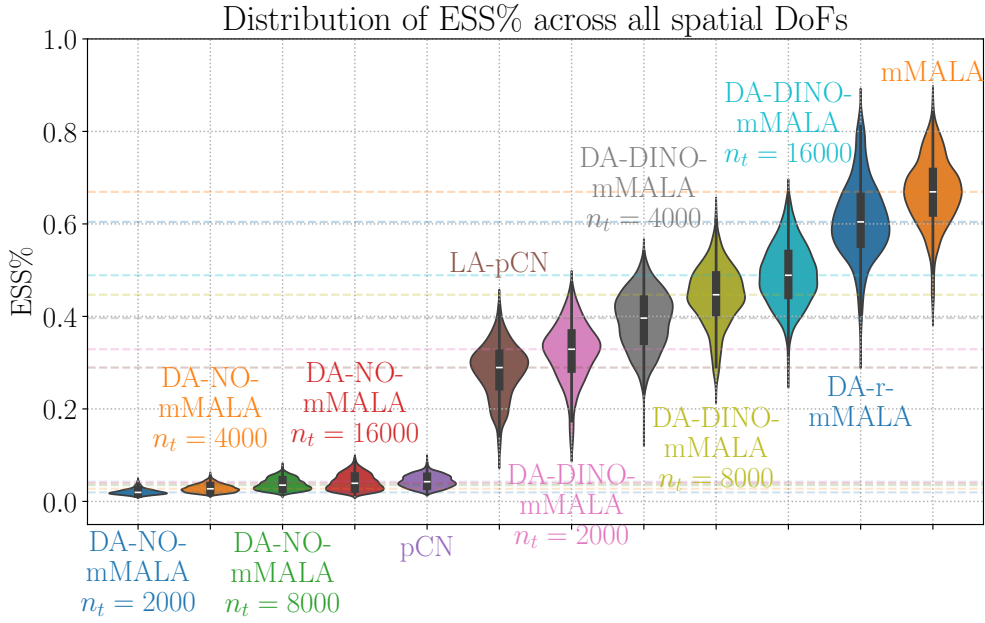


Figure 9: The ESS% diagnostic (see Section 6.2.2) of Markov chains generated by DA-DINO-mMALA (H_μ^1 -trained surrogate proposal with delayed acceptance), DA-NO-mMALA (L_μ^2 -trained surrogate proposal with delayed acceptance), and other baseline and reference MCMC methods for coefficient inversion in a nonlinear diffusion–reaction PDE. The symbol n_t denotes the training sample size for operator learning.

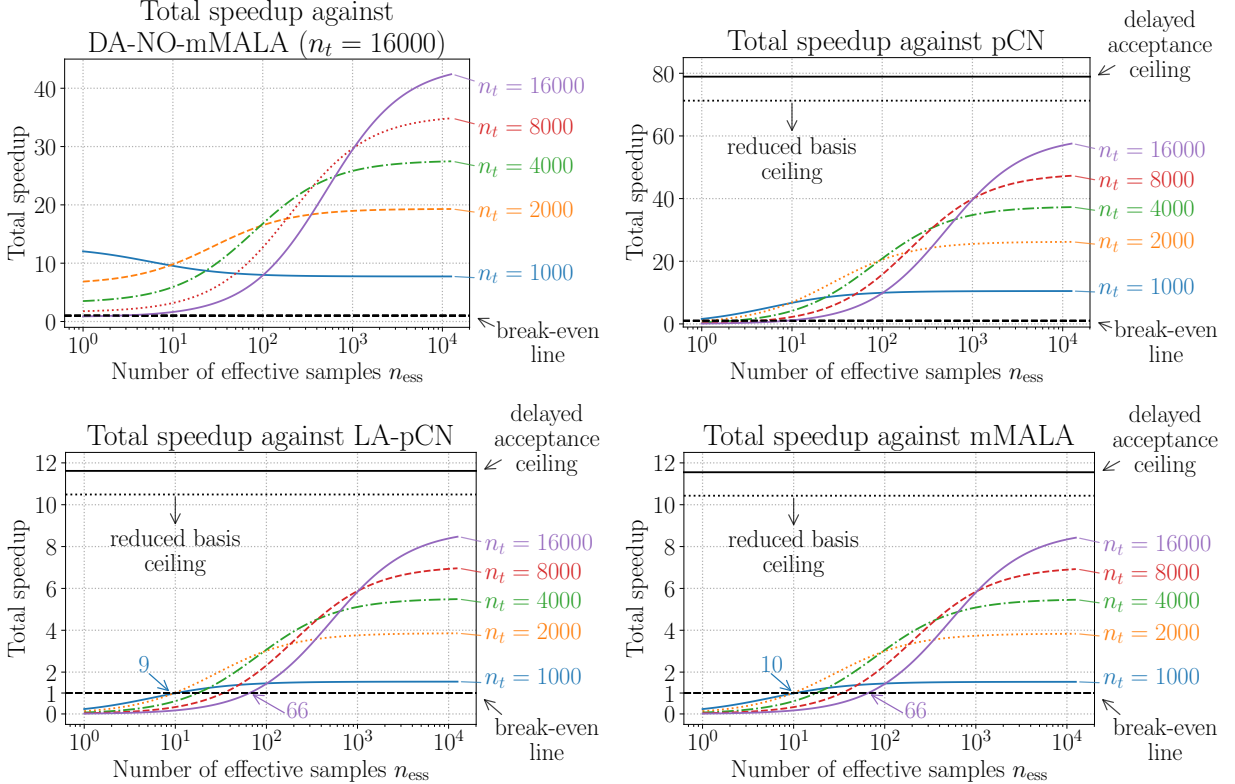


Figure 10: Total effective sampling speedups of DA-DINO-mMALA against DA-NO-mMALA, pCN, LA-pCN, mMALA as a function of effective sample size collected in an MCMC run for coefficient inversion in a nonlinear diffusion-reaction PDE. The total speedup in (42) compares the relative speed of an MCMC method for generating effective samples when including all computational costs, offline (e.g., training and MAP estimate) and online (MCMC). The break-even line indicates an equal total effective sampling speed of the two MCMC methods. The reduced basis ceiling indicates the estimated (via DA-r-mMALA in Table 3) optimal speedup for the reduced basis architecture with $r = 200$ DIS reduced bases. The delayed acceptance ceiling indicates the estimated asymptotic total speedup when the operator surrogate has no error (i.e., model-evaluated PtO map and reduced Jacobian), which leads to 100% second stage acceptance rate. The symbol n_t denotes the training sample size for operator learning.

8. Numerical example: Hyperelastic material property discovery

We consider an experimental scenario where a rectangular thin film of hyperelastic material is stretched on two opposite edges. The inverse problem aims to recover Young's modulus field characterizing spatially varying material strength from measurements of the material deformation.

This section is organized as follows. We introduce the material deformation model, the prior, the PtO map, and the setting for Bayesian inversion in Sections 8.1 to 8.4. Then, we showcase and analyze MCMC results in Section 8.6. In Section 8.6.1, we discuss results on the baseline MCMC methods listed in Table 2. In Section 8.6.2, we discuss results on DA-NO-mMALA and DA-DINO-mMALA listed in Table 3.

8.1. The neo-Hookean model for hyperelastic material deformation

Let $\Omega = (0, 1) \times (0, 2)$ be a normalized reference configuration for the hyperelastic material under the thin film approximation. The material coordinates $\mathbf{x} \in \Omega$ of the reference configuration are mapped to the spatial coordinates $\mathbf{x} + \mathbf{u}(\mathbf{x})$ of the deformed configuration, where $\mathbf{u} : \Omega \rightarrow \mathbb{R}^2$ is the material displacement. Internal forces are developed as the material deforms. These internal forces depend on the underlying stored internal energy; for a hyperelastic material, the strain energy \mathcal{W}_e depends on the deformation gradient, i.e.,

$\mathcal{W}_e = \mathcal{W}_e(\mathbf{F})$ where $\mathbf{F} = \mathbf{I} + \nabla \mathbf{u}$ and $\mathbf{I} \in \mathbb{R}^{2 \times 2}$ is the identity matrix. We consider the neo-Hookean model for the strain energy density [86–88]:

$$\mathcal{W}_e(\mathbf{F}) = \frac{\mu}{2}(\text{tr}(\mathbf{F}^T \mathbf{F}) - 3) + \frac{\lambda}{2}(\ln \det(\mathbf{F}))^2 - \mu \ln \det(\mathbf{F}). \quad (47)$$

Here, λ and μ are the Lamé parameters which we assume to be related to Young's modulus of elasticity, E , and Poisson ratio, ν , as follows:

$$\lambda = \frac{E\nu}{(1+\nu)(1-2\nu)}, \quad \mu = \frac{E}{2(1+\nu)}. \quad (48)$$

We assume prior knowledge of Poisson ratio $\nu = 0.4$, and an epistemically-uncertain and spatially-varying Young's modulus, $E : \Omega \rightarrow (E_{\min}, E_{\max})$ with $0 < E_{\min} < E_{\max}$. We represent E through a parameter field $m : \Omega \rightarrow \mathbb{R}$ as follows

$$E(m(\mathbf{x})) = \frac{1}{2}(E_{\max} - E_{\min})(\text{erf}(m(\mathbf{x})) + 1) + E_{\min},$$

where $\text{erf} : \mathbb{R} \rightarrow (-1, 1)$ is the error function.

The first Piola–Kirchhoff stress tensor is given by

$$\mathbf{P}_e(m, \mathbf{F}) = 2 \frac{\partial \mathcal{W}_e(m, \mathbf{F})}{\partial \mathbf{F}}. \quad (49)$$

Assuming a quasi-static model with negligible body forces, the balance of linear momentum leads to the following nonlinear PDE:

$$\nabla \cdot \mathbf{P}_e(m(\mathbf{x}), \mathbf{F}(\mathbf{x})) = \mathbf{0}, \quad \mathbf{x} \in \Omega; \quad (50a)$$

$$\mathbf{u}(\mathbf{x}) = \mathbf{0}, \quad \mathbf{x} \in \Gamma_{\text{left}}; \quad (50b)$$

$$\mathbf{u}(\mathbf{x}) = 3/2, \quad \mathbf{x} \in \Gamma_{\text{right}}; \quad (50c)$$

$$\mathbf{P}_e(m(\mathbf{x}), \mathbf{F}(\mathbf{x})) \cdot \mathbf{n} = \mathbf{0}, \quad \mathbf{x} \in \Gamma_{\text{top}} \cup \Gamma_{\text{bottom}}; \quad (50d)$$

where Γ_t , Γ_r , Γ_b , and Γ_l denote the material domain's top, right, bottom, and left boundary. Notice that the stretching is enforced as a Dirichlet boundary and the strain specified on the Γ_{right} is 0.75.

8.2. The prior distribution

The normalized Young's modulus follows a prior distribution defined through a Gaussian random field $M \sim \mu$ with $E_{\min} = 1$ and $E_{\max} = 7$:

$$\begin{aligned} \mathcal{M} &:= L^2(\Omega), & & \text{(Parameter space)} \\ \mu &:= \mathcal{N}(0, (-\gamma \nabla \cdot \mathbf{A} \nabla + \delta \mathcal{I}_{\mathcal{M}})^{-2}), & & \text{(The prior distribution)} \end{aligned}$$

where $\mathbf{A} \in \mathbb{R}^{2 \times 2}$ is a symmetric positive definite anisotropic tensor given by

$$\theta_1 = 2, \quad \theta_2 = 1/2, \quad \alpha = \arctan(2), \quad \mathbf{A} = \begin{bmatrix} \theta_1 \sin(\alpha)^2 & (\theta_1 - \theta_2) \sin(\alpha) \cos(\alpha) \\ (\theta_1 - \theta_2) \sin(\alpha) \cos(\alpha) & \theta_2 \cos(\alpha)^2 \end{bmatrix},$$

and the differential operator is equipped with a Robin boundary for eliminating boundary effects. The constants $\gamma, \delta \in \mathbb{R}_+$ are set to $\gamma = 0.3$ and $\delta = 3.3$. Such a prior distribution approximately leads to a pointwise variance of 1 and a spatial correlation of 2 and 1/2 perpendicular and along the left bottom to right top diagonal of the spatial domain. For numerical computation, we approximate \mathcal{M} using a finite element space \mathcal{M}^h constructed by linear triangular finite elements with 2,145 DoFs. We provide a visualization of prior samples in Figure 11.

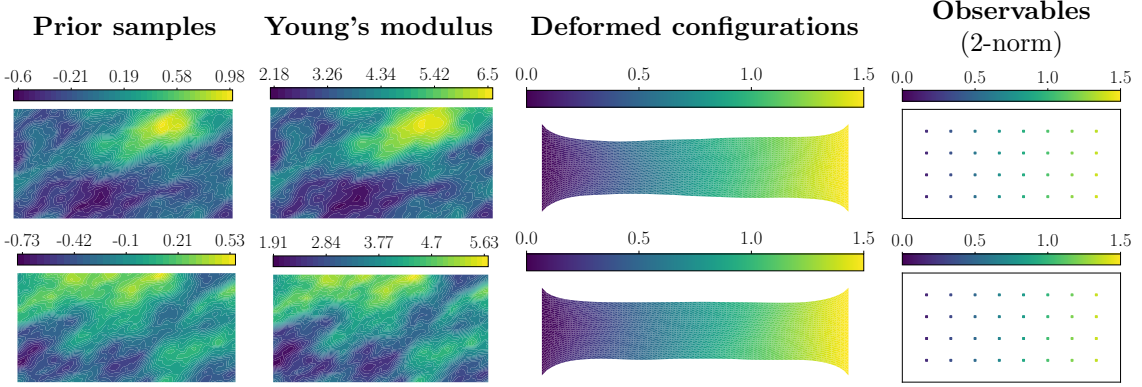


Figure 11: Visualizations of prior samples (2,145 DoFs), deformed configuration (16,770 DoFs), and predicted observables (in \mathbb{R}^{64}) for hyperelastic material property discovery.

8.3. The parameter-to-observable map

We consider a symmetric variational formulation for hyperelastic material deformation. We define the following Hilbert spaces following the notation in [Section 4.3](#):

$$\begin{aligned} \mathcal{U} &:= \left\{ \mathbf{u} \in H^1(\Omega; \mathbb{R}^2) \mid \mathbf{u}|_{\Gamma_l} = \mathbf{0} \wedge \mathbf{u}|_{\Gamma_r} = \mathbf{0} \right\}; & \text{(State space)} \\ \mathcal{V} &:= \mathcal{U}', & \text{(Residual space)} \end{aligned}$$

where \mathcal{U}' denotes the dual space of \mathcal{U} . To enforce the inhomogeneous Dirichlet boundary condition, we decompose the displacement \mathbf{u} into $\mathbf{u} = \mathbf{u}_0 + \mathbf{B}\mathbf{x}$, where $\mathbf{B} = \begin{bmatrix} 3/4 & 0 \\ 0 & 1 \end{bmatrix}$ and $\mathbf{u}_0 \in \mathcal{U}$ is the PDE state with the homogenous Dirichlet boundary condition.

The residual operator for this PDE problem, denoted as $\mathcal{R} : \mathcal{U} \times \mathcal{M} \rightarrow \mathcal{V}$, can be defined by its action on an arbitrary test function $\mathbf{p} \in \mathcal{U}$

$$\langle \mathcal{R}(\mathbf{u}_0, m), \mathbf{p} \rangle_{\mathcal{U}' \times \mathcal{U}} := \int_{\Omega} \mathbf{P}_e(m(\mathbf{x}), \mathbf{I} + \nabla \mathbf{u}_0(\mathbf{x}) + \mathbf{B}) \nabla \mathbf{p}(\mathbf{x}) \, d\mathbf{x}. \quad (51)$$

We thus define the effective parameter-to-solution map as a nonlinear parameter-to-state map $\mathcal{F} : \mathcal{M} \ni m \mapsto \mathbf{u}_0 \in \mathcal{U}$ where $\mathcal{R}(\mathbf{u}_0, m) = 0$. We approximate \mathcal{U} using a finite element space \mathcal{U}^h constructed by quadratic triangular elements with 16,770 DoFs. Evaluating the discretized PDE solution operator involves solving the discretized residual norm minimization problem via the Newton–Raphson method in \mathcal{U}^h .

We define the observation operator \mathcal{O} using 32 equally spaced discrete interior points $\{\mathbf{x}_{\text{obs}}^{(j)}\}_{j=1}^{32}$, which leads to a $d_y = 64$ for the observable space dimension:

$$\mathcal{O}(\mathbf{u}_0) = \left[\int_{\mathbf{B}_e(\mathbf{x}_{\text{obs}}^{(1)})} \mathbf{e}_1^T \mathbf{u}(\mathbf{x}) \, d\mathbf{x} \dots \int_{\mathbf{B}_e(\mathbf{x}_{\text{obs}}^{(1)})} \mathbf{e}_2^T \mathbf{u}(\mathbf{x}) \, d\mathbf{x} \dots \dots \int_{\mathbf{B}_e(\mathbf{x}_{\text{obs}}^{(32)})} \mathbf{e}_2^T \mathbf{u}(\mathbf{x}) \, d\mathbf{x} \right]^T. \quad (52)$$

The PtO map is thus defined as $\mathcal{G} := \mathcal{O} \circ \mathcal{F}$. We visualize the output of the PtO map in [Figure 11](#).

8.4. Bayesian inversion settings

We generate synthetic data for our Bayesian inverse problem using a prior sample. The model-predicted observable at the synthetic parameter field is then corrupted with 1% additive white noise, which leads to a noise covariance matrix of identity scaled by $v_n = 1.8 \times 10^{-4}$:

$$\pi_n = \mathcal{N}(\mathbf{0}, v_n \mathbf{I}). \quad (\text{Noise distribution})$$

We visualize the synthetic data, its generating parameter, and the MAP estimate in [Figure 12](#).

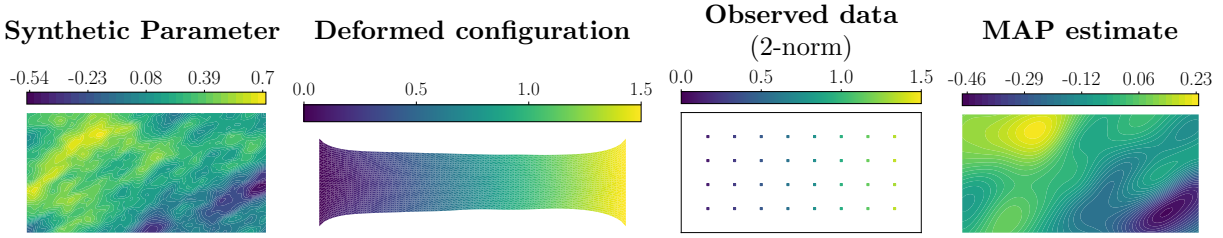


Figure 12: Visualization of the Bayesian inverse problem setting and the MAP estimate for hyperelastic material property discovery.

8.5. Neural operator surrogate

We follow the procedure described in [Section 4.3](#) for generating samples for neural network training and testing. We compute DIS reduced bases of dimension $r = 200$ using $n_{\text{DIS}} = 500$ of the generated samples as specified in [\(23\)](#). We visualize selected DIS basis functions in [Figure F.21](#). Forming reduced Jacobian matrices via columns using a direct solver with reused factorization takes 10% of the computing time for solving the nonlinear PDEs using a direct solver, estimated on average over sample generation. Note that the relative cost of forming reduced Jacobian is low mainly because a large number of Newton–Raphson iterations are required to solve the PDE.

We use a dense neural network architecture with six hidden layers, each with 400 hidden neurons and a GELU activation function, trained using $n_t = 125, 250, \dots, 8,000$ samples. We estimate the generalization errors of the trained neural networks using 2,500 testing samples. In [Figure 13](#), we plot the estimated errors as a function of training sample generation cost, measured relative to the averaged cost of one nonlinear PDE solve.

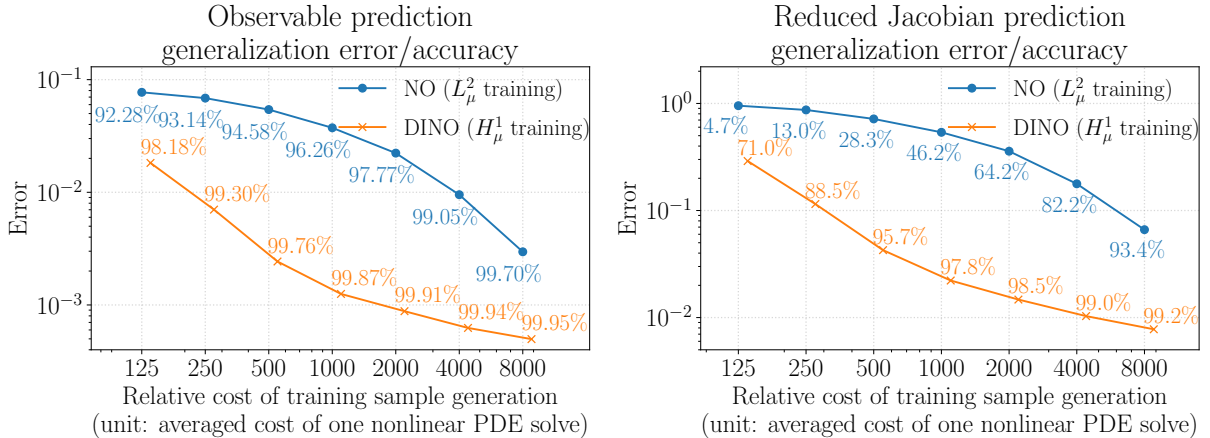


Figure 13: The generalization error and accuracy [\(46\)](#) of observable prediction and reduced Jacobian prediction made by L^2_μ -trained neural operators and H^1_μ -trained DINOs for hyperelastic material property discovery. The error is plotted as a function of training sample generation cost, measured relative to the averaged cost of one nonlinear PDE solve.

The plot leads us to similar conclusions detailed in [Section 7.4](#). It shows that the derivative-informed H^1_μ operator learning significantly improves the quality of the neural operator surrogate at the same training sample generation cost compared to the conventional L^2_μ operator learning. In particular, it takes around 16 times less training sample generation cost for H^1_μ training to achieve the same observable and reduced Jacobian prediction generalization accuracy.

8.6. MCMC results

We present numerical results related to the efficiency of DA-DINO-mMALA methods compared to the baseline MCMC methods. For each method, we collect $n_c = 10$ Markov chains with different initialization, each with $n_s = 19,000$ samples (after burn-in). The step size parameter Δt and initialization are chosen carefully according to the procedure detailed in [Appendix E](#). We provide the settings and statistics of the MCMC runs as well as posterior visualization in [Appendix F](#).

8.6.1. The baseline MCMC methods

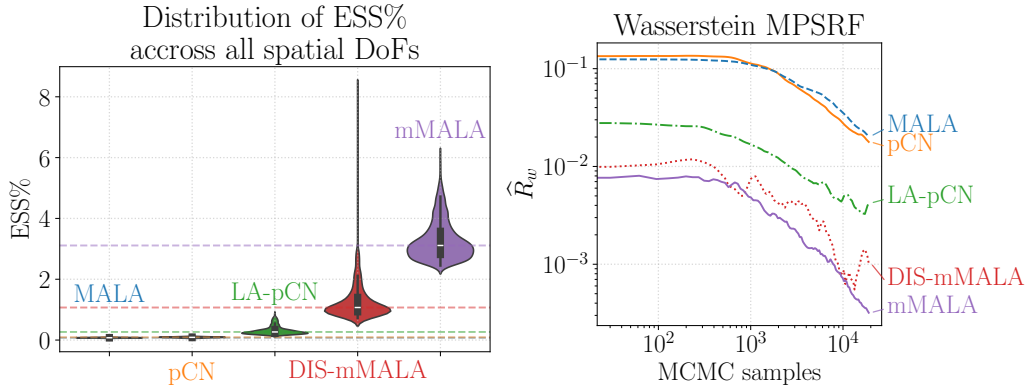


Figure 14: Visualization of the diagnostics (see [Section 6.2](#)) of MCMC chains generated by baseline MCMC methods listed in [Table 2](#) for hyperelastic material property discovery. (left) The violin plot of the ESS% distributions over 2,145 spatial DoFs for the discretized parameter space. We note that the ESS% of DIS-mMALA is larger than that of mMALA at only 5 spatial DoFs. (left) The Wasserstein MPSRF as a function of the Markov chain position.

Baseline \ Speedup	mMALA	DA-DINO-mMALA $n_t = 500$	DA-DINO-mMALA $n_t = 4000$
pCN	29.6	72.7	96.2
MALA	38.8	93.2	126.4
LA-pCN	9.9	24.4	32.3
DIS-mMALA	2.8	6.8	9
mMALA	1	2.5	3.3
DA-NO-mMALA $n_t = 4000$	5.5	13.5	17.9

Table 5: The effective sampling speedup of mMALA, DINO-mMALA, and DA-DINO-mMALA against other baseline MCMC methods for hyperelastic material property discovery. The speedup measures the relative speed of generating effective samples for an MCMC method compared against another MCMC method; see (41).

In [Figure 14](#), we visualize the diagnostics for the baseline MCMC methods in [Table 2](#). The diagnostics show that mMALA produces Markov chains with the most effective samples and fastest mixing time among the baseline methods. When comparing within the class of methods with the same type of posterior geometry information (see [Table 2](#)), MALA is slightly inferior to pCN, and LA-pCN is much inferior to DIS-mMALA.

Comparing the median of ESS%, mMALA produced 35 and 3 times more effective samples than pCN and DIS-mMALA. We note that the ESS% of DIS-mMALA is larger than that of mMALA at merely 5 DoFs out of 2,145. Moreover, due to the large number of iterative solves required for each PtO map evaluation, each Markov chain sample generated by mMALA is only around 1.18 and 1.05 times more computationally costly than pCN and DIS-mMALA. We provide the effective sampling speedups (41) of mMALA against other baseline MCMC methods in [Table 5](#).

8.6.2. Delayed acceptance geometric MCMC with operator surrogate proposal

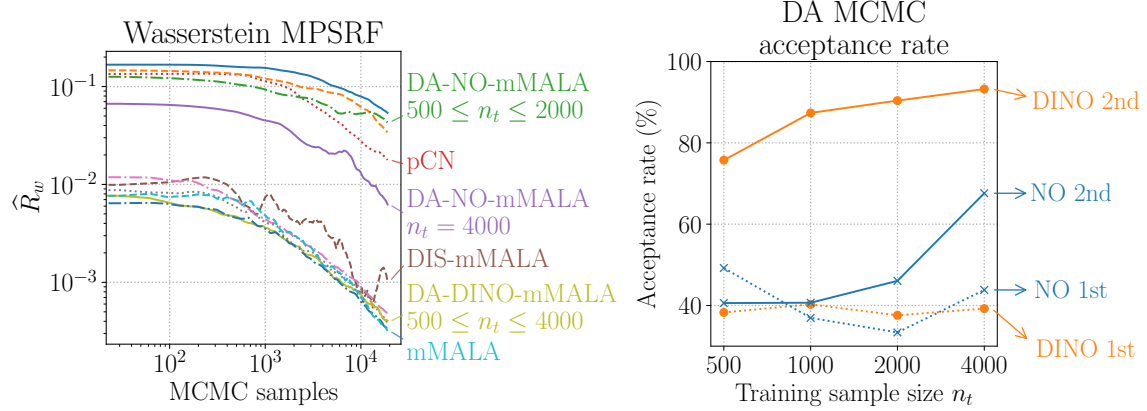


Figure 15: (left) The Wasserstein MPSRF diagnostic (see Section 6.2.1) of Markov chains generated by DA-DINO-mMALA (H_μ^1 -trained surrogate proposal with delayed acceptance), DA-NO-mMALA (L_μ^2 -trained surrogate proposal with delayed acceptance), and other baseline MCMC methods for hyperelastic material property discovery. (right) The proposal acceptance rate in the first and second stages of the DA procedure as a function of training sample size.

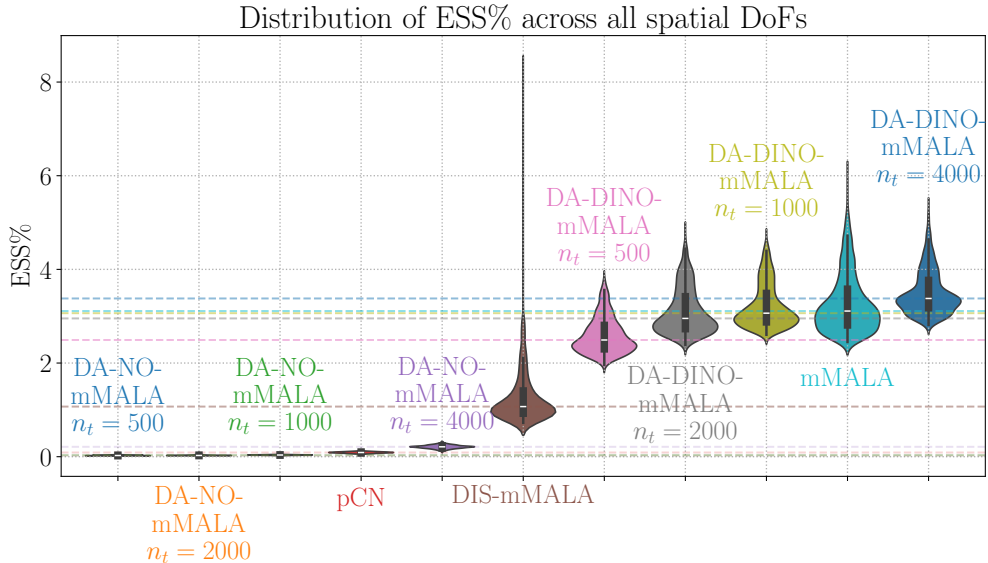


Figure 16: The ESS% diagnostic (see Section 6.2.2) of Markov chains generated by DA-DINO-mMALA (H_μ^1 -trained surrogate proposal with delayed acceptance), DA-NO-mMALA (L_μ^2 -trained surrogate proposal with delayed acceptance), and other baseline MCMC methods for hyperelastic material property discovery. The symbol n_t denotes the training sample size for operator learning.

In Figure 15 (left) and Figure 16, we visualize the diagnostics of the Markov chains generated by the surrogate-driven delayed acceptance geometric MCMC. The diagnostics show that DA-DINO-mMALA at $n_t = 500$ and beyond outperforms DIS-mMALA regarding the effective sample size and mixing speed of MCMC chains. Furthermore, the ESS% of DA-DINO-mMALA plateaued at around $n_t = 1,000$, meaning the error due to (i) imperfect step size tuning, (ii) finite chain length, and (iii) finite Markov chain pool sizes is dominating the ESS% fluctuation. After including the extra computational cost of mMALA at each MCMC sample and the cost reduction of the DA procedure, we observe that DA-DINO-mMALA at $n_t = 4,000$ generates effective samples around 3.3 times faster than mMALA.

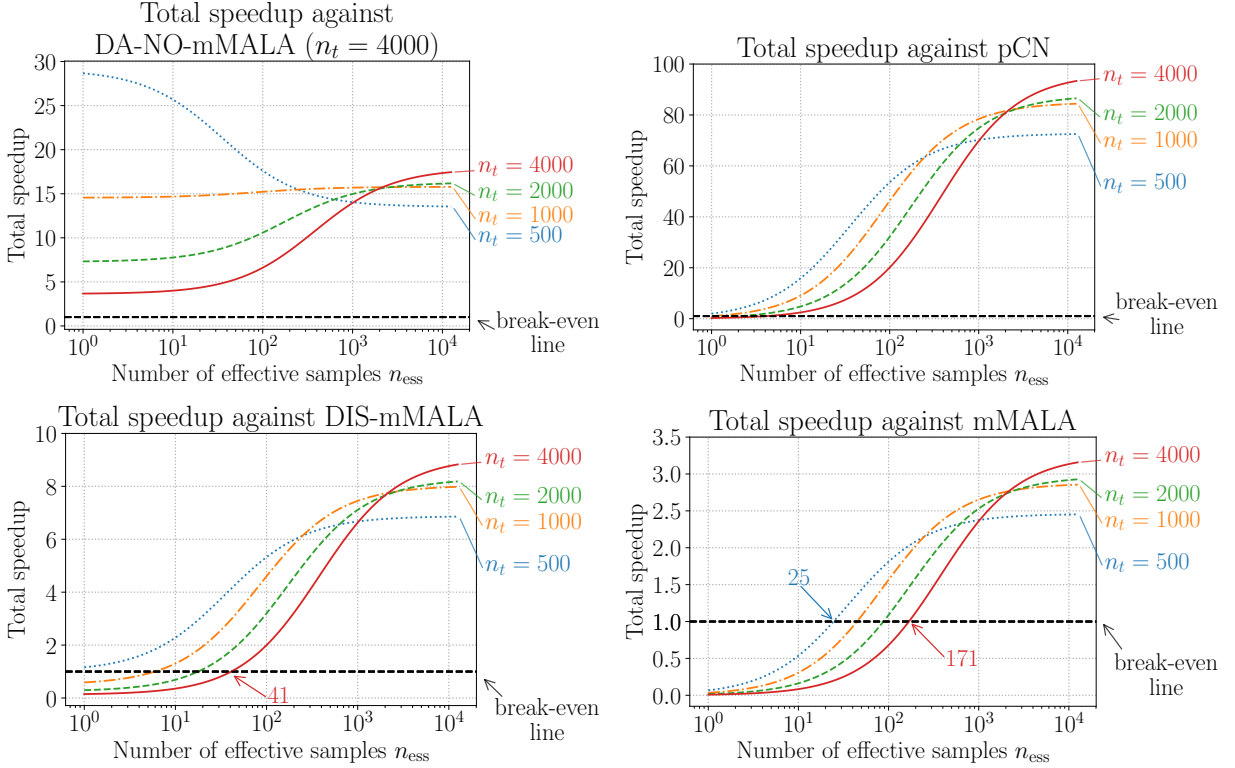


Figure 17: Total effective sampling speedups of DA-DINO-mMALA against DA-NO-mMALA, pCN, DIS-mMALA, mMALA as a function of effective sample size collected in an MCMC run for hyperelastic material property discovery. The total speedup in (42) compares the relative speed of an MCMC method for generating effective samples when considering all computational costs, offline (e.g., training and MAP estimate) and online (MCMC). The break-even line indicates an equal total effective sampling speed of the two MCMC methods. The symbol n_t denotes the training sample size for operator learning.

Driven by L_μ^2 -trained operator surrogate, DA-NO-mMALA at $n_t = 4,000$ outperforms pCN regarding the effective sample size and mixing speed. After including the cost reduction of the DA procedure, DA-NO-mMALA at $n_t = 4,000$ generates effective samples 5 and 2 times faster than pCN and LA-pCN. However, it is still 2 and 5.5 times slower than DIS-mMALA and mMALA. Furthermore, it is 13.5 and 17.9 times slower than DA-DINO-mMALA at $n_t = 500$ and 4,000. See the speedups of DA-DINO-mMALA and DA-NO-mMALA against other methods in Table 4.

In Figure 15 (right), we visualize the proposal acceptance rate in the first and second stages of the DA procedure for both DA-DINO-mMALA and DA-NO-mMALA. The plot shows that DA-DINO-mMALA has a high second-stage acceptance rate, improving consistently as the training sample size grows. When comparing between L_μ^2 -trained NO and H_μ^1 -trained DINO, the second-stage acceptance rate for DA-NO-mMALA is 1.3–2.3 times the rate for DA-DINO-mMALA. These results affirm that H_μ^1 -trained DINO leads to higher quality Markov chains for posterior sampling.

In Figure 17, we plot the total effective sampling speedups of DA-DINO-mMALA against DA-NO-mMALA at $n_t = 4,000$, pCN, LA-pCN and mMALA. The total speedups against LA-pCN and mMALA show that if one wants to collect more than 25 effective posterior samples, then it is more efficient to switch to DA-DINO-mMALA with $n_t = 500$ rather than using mMALA. On the other hand, the asymptotic speedup at $n_t = 500$ is relatively small. We achieve an asymptotic speedup of 3.3 against mMALA, one needs to collect 171 effective posterior samples to break even the offline cost of training.

9. Conclusion

In this work, we propose deploying a neural operator surrogate of the PtO map to accelerate geometric MCMC and obtain fast and consistent solutions to infinite-dimensional Bayesian inverse problems. The method synergizes reduced basis DINO, DA MCMC, and dimension-independent geometric MCMC to design an MCMC proposal that adapts to DINO-predicted posterior local geometry within a delayed acceptance procedure. Compared to conventional geometric MCMC, such a surrogate-driven geometric MCMC method leads to significant cost reduction, as it requires no online forward or adjoint sensitivity solves, fewer model quanries, and fewer instances of prior sampling. Our numerical results show that our proposed method is capable of producing high-quality Markov chains typical for a geometric MCMC method at a much lower cost, leading to substantial speedups in posterior sample generation. In particular, our numerical examples show that DA-DINO-mMALA generates effective posterior samples 60–97 times faster than pCN and 3–9 times faster than mMALA. Moreover, the training cost of DINO surrogates breaks even after collecting merely 10–25 effective posterior samples when compared to mMALA.

The key to enabling a surrogate acceleration of geometric MCMC is our derivative-informed operator learning formulation. We present an operator learning objective in H_μ^1 Sobolev space with Gaussian measure that exerts error control in the stochastic derivative of the PtO map. Such a formulation is naturally equipped with the Poincaré inequality for nonlinear mappings on function spaces, which is used to derive a L_μ^2 approximation error bound for the reduced basis neural operator surrogate consisting of three sources of error: (i) neural network approximation of the optimal reduced mapping, (ii) basis truncation error, (iii) sampling error when applicable. Our numerical examples show that derivative-informed H_μ^1 operator learning achieves similar generalization accuracy in predicting the observable and its parametric derivative with at least 16–25 times less training sample generation cost than the conventional L_μ^2 operator learning. For coefficient inversion in nonlinear diffusion–reaction PDE, we observe an estimated 166 times difference in training sample generation cost between derivative-informed H_μ^1 and conventional L_μ^2 operator learning for reaching a meaningful speedup compared to mMALA.

Acknowledgments

This work was partially supported by the National Science Foundation under the award OAC-2313033, and the U.S. Department of Energy, Office of Science, Office of Advanced Scientific Computing Research under awards DE-SC0021239 and DE-SC0023171. The work of Lianghao Cao was partially supported by a Department of Defense Vannevar Bush Faculty Fellowship held by Andrew M. Stuart, and by the SciAI Center, funded by the Office of Naval Research (ONR), under Grant Number N00014-23-1-2729. The work benefited from discussions with Dingcheng Luo and Jakob Zech.

References

- [1] L. Biegler, G. Biros, O. Ghattas, M. Heinkenschloss, D. Keyes, B. Mallick, Y. Marzouk, L. Tenorio, B. van Bloemen Waanders, K. Willcox (Eds.), *Large-Scale Inverse Problems and Quantification of Uncertainty*, John Wiley & Sons, Ltd, 2010.
- [2] J. T. Oden, I. Babuška, D. Faghihi, Predictive computational science: Computer predictions in the presence of uncertainty, in: *Encyclopedia of Computational Mechanics*, John Wiley & Sons, Ltd, 2nd edition, 2017, pp. 1–26.
- [3] D. P. Kouri, A. Shapiro, Optimization of pdes with uncertain inputs, *Frontiers in PDE-constrained optimization* (2018) 41–81.
- [4] O. Ghattas, K. Willcox, Learning physics-based models from data: Perspectives from inverse problems and model reduction, *Acta Numerica* 30 (2021) 445–554.
- [5] A. Alexanderian, Optimal experimental design for infinite-dimensional bayesian inverse problems governed by pdes: a review, *Inverse Problems* 37 (2021) 043001.
- [6] N. Metropolis, A. W. Rosenbluth, M. N. Rosenbluth, A. H. Teller, E. Teller, Equation of state calculations by fast computing machines, *The Journal of Chemical Physics* 21 (1953) 1087–1092.
- [7] W. K. Hastings, Monte Carlo sampling methods using Markov chains and their applications, *Biometrika* 57 (1970) 97–109.
- [8] C. P. Robert, G. Casella, *Monte Carlo Statistical Methods*, Springer texts in statistics, Springer, New York, New York, 2nd edition, 2004.
- [9] G. O. Roberts, J. S. Rosenthal, General state space Markov chains and MCMC algorithms, *Probability Surveys* 1 (2004) 20–71.

[10] M. Girolami, B. Calderhead, Riemann manifold Langevin and Hamiltonian Monte Carlo methods, *Journal of the Royal Statistical Society: Series B (Statistical Methodology)* 73 (2011) 123–214.

[11] J. Martin, L. C. Wilcox, C. Burstedde, O. Ghattas, A stochastic Newton MCMC method for large-scale statistical inverse problems with application to seismic inversion, *SIAM Journal on Scientific Computing* 34 (2012) A1460–A1487.

[12] K. Law, Proposals which speed up function-space MCMC, *Journal of Computational and Applied Mathematics* 262 (2014) 127–138. Selected Papers from NUMDIFF-13.

[13] T. Bui-Thanh, M. Girolami, Solving large-scale PDE-constrained Bayesian inverse problems with Riemann manifold Hamiltonian Monte Carlo, *Inverse Problems* 30 (2014) 114014.

[14] S. Lan, T. Bui-Thanh, M. Christie, M. Girolami, Emulation of higher-order tensors in manifold Monte Carlo methods for Bayesian inverse problems, *Journal of Computational Physics* 308 (2016) 81–101.

[15] A. Beskos, M. Girolami, S. Lan, P. E. Farrell, A. M. Stuart, Geometric MCMC for infinite-dimensional inverse problems, *Journal of Computational Physics* 335 (2017) 327–351.

[16] S. Lan, Adaptive dimension reduction to accelerate infinite-dimensional geometric Markov chain Monte Carlo, *Journal of Computational Physics* 392 (2019) 71–95.

[17] J. A. Christen, C. Fox, Markov chain Monte Carlo using an approximation, *Journal of Computational and Graphical Statistics* 14 (2005) 795–810.

[18] Y. Efendiev, T. Hou, W. Luo, Preconditioning Markov chain Monte Carlo simulations using coarse-scale models, *SIAM Journal on Scientific Computing* 28 (2006) 776–803.

[19] M. B. Lykkegaard, T. J. Dodwell, C. Fox, G. Mingas, R. Scheichl, Multilevel delayed acceptance MCMC, *SIAM/ASA Journal on Uncertainty Quantification* 11 (2023) 1–30.

[20] N. Kovachki, Z. Li, B. Liu, K. Azizzadenesheli, K. Bhattacharya, A. Stuart, A. Anandkumar, Neural operator: Learning maps between function spaces with applications to PDEs, *Journal of Machine Learning Research* 24 (2023) 1–97.

[21] N. B. Kovachki, S. Lanthaler, A. M. Stuart, Operator learning: Algorithms and analysis, *arXiv preprint, arXiv.2402.15715* (2024).

[22] D. Luo, T. O’Leary-Roseberry, P. Chen, O. Ghattas, Efficient PDE-constrained optimization under high-dimensional uncertainty using derivative-informed neural operators, *arXiv preprint arXiv.2305.20053* (2023).

[23] T. O’Leary-Roseberry, P. Chen, U. Villa, O. Ghattas, Derivative-Informed Neural Operator: An efficient framework for high-dimensional parametric derivative learning, *Journal of Computational Physics* 496 (2024) 112555.

[24] S. L. Cotter, G. O. Roberts, A. M. Stuart, D. White, MCMC methods for functions: Modifying old algorithms to make them faster, *Statistical Science* 28 (2013) 424–446.

[25] J. Hesthaven, S. Ubbiali, Non-intrusive reduced order modeling of nonlinear problems using neural networks, *Journal of Computational Physics* 363 (2018) 55–78.

[26] S. Fresca, A. Manzoni, POD-DL-ROM: Enhancing deep learning-based reduced order models for nonlinear parametrized PDEs by proper orthogonal decomposition, *Computer Methods in Applied Mechanics and Engineering* 388 (2022) 114181.

[27] K. Bhattacharya, B. Hosseini, N. B. Kovachki, A. M. Stuart, Model reduction and neural network for parametric PDEs, *The SMAI Journal of computational mathematics* 7 (2021) 121–157.

[28] T. O’Leary-Roseberry, X. Du, A. Chaudhuri, J. R. Martins, K. Willcox, O. Ghattas, Learning high-dimensional parametric maps via reduced basis adaptive residual networks, *Computer Methods in Applied Mechanics and Engineering* 402 (2022) 115730.

[29] T. O’Leary-Roseberry, U. Villa, P. Chen, O. Ghattas, Derivative-informed projected neural networks for high-dimensional parametric maps governed by PDEs, *Computer Methods in Applied Mechanics and Engineering* 388 (2022) 114199.

[30] L. Lu, P. Jin, G. Pang, G. E. Karniadakis, DeepONet: Learning nonlinear operators for identifying differential equations based on the universal approximation theorem of operators, *Nature Machine Intelligence* (2021).

[31] J. H. Seidman, G. Kissas, G. J. Pappas, P. Perdikaris, Variational autoencoding neural operators, *arXiv preprint, arXiv.2302.10351* (2023).

[32] Z. Li, N. Kovachki, K. Azizzadenesheli, B. Liu, K. Bhattacharya, A. Stuart, A. Anandkumar, Fourier neural operator for parametric partial differential equations, *arXiv preprint, arXiv.2010.08895* (2021).

[33] Q. Cao, S. Goswami, G. E. Karniadakis, LNO: Laplace neural operator for solving differential equations, *arXiv preprint, arXiv.2303.10528* (2023).

[34] S. Lanthaler, Z. Li, A. M. Stuart, The nonlocal neural operator: Universal approximation, *arXiv preprint, arXiv.2304.13221* (2023).

[35] Z. Li, N. Kovachki, K. Azizzadenesheli, B. Liu, K. Bhattacharya, A. Stuart, A. Anandkumar, Neural operator: Graph kernel network for partial differential equations, *arXiv preprint, arXiv.2003.03485* (2020).

[36] Z. Li, N. Kovachki, K. Azizzadenesheli, B. Liu, A. Stuart, K. Bhattacharya, A. Anandkumar, Multipole graph neural operator for parametric partial differential equations, in: H. Larochelle, M. Ranzato, R. Hadsell, M. Balcan, H. Lin (Eds.), *Advances in Neural Information Processing Systems*, volume 33, Curran Associates, Inc., 2020, pp. 6755–6766.

[37] M. De Hoop, D. Z. Huang, E. Qian, A. M. Stuart, The cost-accuracy trade-off in operator learning with neural networks, *arXiv preprint, arXiv:2203.13181* (2022).

[38] L. Lu, X. Meng, S. Cai, Z. Mao, S. Goswami, Z. Zhang, G. E. Karniadakis, A comprehensive and fair comparison of two neural operators (with practical extensions) based on fair data, *Computer Methods in Applied Mechanics and Engineering* 393 (2022) 114778.

[39] Z. Li, H. Zheng, N. Kovachki, D. Jin, H. Chen, B. Liu, K. Azizzadenesheli, A. Anandkumar, Physics-informed neural operator for learning partial differential equations, *ACM / IMS Journal of Data Science* (2024).

[40] S. Wang, H. Wang, P. Perdikaris, Learning the solution operator of parametric partial differential equations with physics-informed DeepONets, *Science Advances* 7 (2021) eabi8605.

[41] J. Go, P. Chen, Accelerating Bayesian optimal experimental design with derivative-informed neural operators, arXiv preprint arXiv:2312.14810 (2023).

[42] M. Hairer, A. M. Stuart, S. J. Vollmer, Spectral gaps for a Metropolis–Hastings algorithm in infinite dimensions, *The Annals of Applied Probability* 24 (2014) 2455–2490.

[43] T. Cui, K. J. Law, Y. M. Marzouk, Dimension-independent likelihood-informed MCMC, *Journal of Computational Physics* 304 (2016) 109–137.

[44] T. Bui-Thanh, Q. P. Nguyen, FEM-based discretization-invariant MCMC methods for PDE-constrained Bayesian inverse problems, *Inverse Problems and Imaging* 10 (2016) 943–975.

[45] D. Rudolf, B. Sprungk, On a generalization of the preconditioned Crank–Nicolson Metropolis algorithm, *Foundations of Computational Mathematics* 18 (2018) 309–343.

[46] N. Petra, J. Martin, G. Stadler, O. Ghattas, A computational framework for infinite-dimensional Bayesian inverse problems, Part II: Stochastic Newton MCMC with application to ice sheet flow inverse problems, *SIAM Journal on Scientific Computing* 36 (2014) A1525–A1555.

[47] F. J. Pinski, G. Simpson, A. M. Stuart, H. Weber, Algorithms for Kullback–Leibler approximation of probability measures in infinite dimensions, *SIAM Journal on Scientific Computing* 37 (2015) A2733–A2757.

[48] P. G. Constantine, E. Dow, Q. Wang, Active subspace methods in theory and practice: Applications to kriging surfaces, *SIAM Journal on Scientific Computing* 36 (2014) A1500–A1524.

[49] P. G. Constantine, C. Kent, T. Bui-Thanh, Accelerating Markov chain Monte Carlo with active subspaces, *SIAM Journal on Scientific Computing* 38 (2016) A2779–A2805.

[50] K.-T. Kim, U. Villa, M. Parno, Y. Marzouk, O. Ghattas, N. Petra, hIPPYlib-MUQ: A Bayesian inference software framework for integration of data with complex predictive models under uncertainty, *ACM Trans. Math. Softw.* 49 (2023).

[51] N. S. P. Patrick R. Conrad, Youssef M. Marzouk, A. Smith, Accelerating asymptotically exact MCMC for computationally intensive models via local approximations, *Journal of the American Statistical Association* 111 (2016) 1591–1607.

[52] B. Peherstorfer, Y. Marzouk, A transport-based multifidelity preconditioner for Markov chain Monte Carlo, *Advances in Computational Mathematics* 45 (2019) 2321–2348.

[53] V. H. Hoang, C. Schwab, A. M. Stuart, Complexity analysis of accelerated MCMC methods for Bayesian inversion, *Inverse Problems* 29 (2013) 085010.

[54] J. Latz, I. Papaioannou, E. Ullmann, Multilevel sequential2 Monte Carlo for Bayesian inverse problems, *Journal of Computational Physics* 368 (2018) 154–178.

[55] T. J. Dodwell, C. Ketelsen, R. Scheichl, A. L. Teckentrup, Multilevel Markov chain Monte Carlo, *SIAM Review* 61 (2019) 509–545.

[56] T. Cui, G. Detommaso, R. Scheichl, Multilevel dimension-independent likelihood-informed MCMC for large-scale inverse problems, *Inverse Problems* 40 (2024) 035005.

[57] A. M. Stuart, Inverse problems: A Bayesian perspective, *Acta Numerica* 19 (2010) 451–459.

[58] T. J. Sullivan, *Introduction to Uncertainty Quantification*, Texts in Applied Mathematics, Springer Cham, 2015.

[59] V. I. Bogachev, Gaussian measures, volume 62 of *Mathematical Surveys and Monographs*, American Mathematical Society, 1998.

[60] D. Nualart, E. Nualart, *Introduction to Malliavin Calculus*, volume 9 of *Institute of Mathematical Statistics Textbooks*, Cambridge University Press, 2018.

[61] V. Kac, P. Cheung, *Quantum Calculus*, volume 113 of *Universitext*, Springer New York, NY, 2002.

[62] L. Tierney, A note on Metropolis–Hastings kernels for general state spaces, *The Annals of Applied Probability* 8 (1998) 1–9.

[63] I. Gohberg, S. Goldberg, N. Krupnik, *Traces and Determinants of Linear Operators*, volume 116 of *Operator Theory: Advances and Applications*, Birkhäuser Basel, 2012.

[64] R. Baptista, Y. Marzouk, O. Zahm, Gradient-based data and parameter dimension reduction for Bayesian models: An information theoretic perspective, arXiv preprint, arXiv:2207.08670 (2022).

[65] O. Zahm, P. G. Constantine, C. Prieur, Y. M. Marzouk, Gradient-based dimension reduction of multivariate vector-valued functions, *SIAM Journal on Scientific Computing* 42 (2020) A534–A558.

[66] T. Cui, O. Zahm, Data-free likelihood-informed dimension reduction of Bayesian inverse problems, *Inverse Problems* 37 (2021) 045009.

[67] T. Bui-Thanh, O. Ghattas, J. Martin, G. Stadler, A computational framework for infinite-dimensional Bayesian inverse problems part I: The linearized case, with application to global seismic inversion, *SIAM Journal on Scientific Computing* 35 (2013) A2494–A2523.

[68] U. Villa, N. Petra, O. Ghattas, hIPPYlib: An extensible software framework for large-scale inverse problems governed by PDEs: Part I: Deterministic inversion and linearized Bayesian inference, *ACM Transactions on Mathematical Software* 47 (2021).

[69] A. Manzoni, A. Quarteroni, S. Salsa, *Optimal control of partial differential equations*, Applied Mathematical Sciences, Springer Cham, 2021.

[70] F. Tröltzsch, *Optimal control of partial differential equations: Theory, methods, and applications*, volume 112, American Mathematical Society, 2010.

[71] P. G. Ciarlet, *Linear and Nonlinear Functional Analysis with Applications*, the Society for Industrial and Applied Mathematics, 2013.

[72] T. A. Davis, S. Rajamanickam, W. M. Sid-Lakhdar, A survey of direct methods for sparse linear systems, *Acta Numerica* 25 (2016) 383–566.

[73] L. Cao, T. O’Leary-Roseberry, P. K. Jha, J. T. Oden, O. Ghattas, Residual-based error correction for neural operator

accelerated infinite-dimensional Bayesian inverse problems, *Journal of Computational Physics* 486 (2023) 112104.

[74] C. Schwab, J. Zech, Deep learning in high dimension: Neural network expression rates for analytic functions in $L^2(\mathbb{R}^d, \gamma_d)$, *SIAM/ASA Journal on Uncertainty Quantification* 11 (2023) 199–234.

[75] T. Cui, Y. M. Marzouk, K. E. Willcox, Data-driven model reduction for the Bayesian solution of inverse problems, *International Journal for Numerical Methods in Engineering* 102 (2015) 966–990.

[76] P. Whittle, On stationary processes in the plane, *Biometrika* 41 (1954) 434–449.

[77] M. Dashti, K. J. H. Law, A. M. Stuart, J. Voss, MAP estimators and their consistency in Bayesian nonparametric inverse problems, *Inverse Problems* 29 (2013) 095017.

[78] S. P. Brooks, A. Gelman, General methods for monitoring convergence of iterative simulations, *Journal of Computational and Graphical Statistics* 7 (1998) 434–455.

[79] D. Dowson, B. Landau, The Fréchet distance between multivariate normal distributions, *Journal of Multivariate Analysis* 12 (1982) 450–455.

[80] A. Gelman, J. B. Carlin, H. S. Stern, D. B. Dunson, A. Vehtari, D. B. Rubin, *Bayesian Data Analysis*, Chapman & Hall/CRC texts in statistical science, CRC Press, Boca Raton, Florida, 3rd edition, 2014.

[81] M. Alnæs, J. Blechta, J. Hake, A. Johansson, B. Kehlet, A. Logg, C. Richardson, J. Ring, M. E. Rognes, G. N. Wells, The FEniCS project version 1.5, *Archive of Numerical Software* 3 (2015).

[82] A. Logg, K.-A. Mardal, G. Wells, *Automated solution of differential equations by the finite element method: The FEniCS book*, volume 84, Springer Science & Business Media, 2012.

[83] U. Villa, N. Petra, O. Ghattas, hIPPYlib: An extensible software framework for large-scale inverse problems, *The Journal of Open Source Software* 3 (2018) 940.

[84] T. O’Leary-Roseberry, U. Villa, hIPPYflow: Dimension reduced surrogate construction for parametric PDE maps in Python, 2021.

[85] T. O’Leary-Roseberry, dino: Derivative-informed neural operator, an efficient framework for high-dimensional parametric derivative learning, v0.2.0 edition, 2023.

[86] J. E. Marsden, T. J. Hughes, *Mathematical foundations of elasticity*, Courier Corporation, 1994.

[87] R. Ogden, *Non-linear Elastic Deformations*, Dover Civil and Mechanical Engineering, Dover Publications, 1997.

[88] O. Gonzalez, A. M. Stuart, *A first course in continuum mechanics*, volume 42, Cambridge University Press, 2008.

[89] R. R. Lam, O. Zahm, Y. M. Marzouk, K. E. Willcox, Multifidelity dimension reduction via active subspaces, *SIAM Journal on Scientific Computing* 42 (2020) A929–A956.

[90] G. Da Prato, J. Zabczyk, *Second order partial differential equations in Hilbert spaces*, volume 293, Cambridge University Press, 2002.

Appendix A. Stochastic Gâteaux differentiability

From [Assumption 4](#) and [Definition 1](#), it is clear that μ -a.e. Gâteaux differentiability implies stochastic Gâteaux differentiability. Here, we provide a specific case where the reverse cannot be true. The following lemma uses the Cameron–Martin and Feldman–Hájek theorem [\[58, Theorem 2.51\]](#) to establish that μ -a.e. Gâteaux differentiability requires a more regular forward operator \mathcal{G} than the μ -a.e. well-definedness specified in [Assumption 3](#).

Lemma Appendix A.1. *Assume \mathcal{G} is well-defined μ -a.e. and ill-defined on all sets $\mathcal{A} \subset \mathcal{M}$ with $\mu(\mathcal{A}) = 0$. Then, stochastic Gâteaux differentiability does not imply μ -a.e. Gâteaux differentiability. In particular, \mathcal{G} is not Gâteaux differentiable μ -a.e.*

Proof. We focus on the term $\mathcal{G}(M + t\hat{m})$ for $t > 0$ and $M \sim \mu$ in the definition of the Gâteaux $(\hat{m} \in \mathcal{M})$ and stochastic Gâteaux $(\hat{m} \in \mathcal{H}_\mu)$ derivative. Let $\mathcal{N}_\mu := \{\mathcal{A} \subset \mathcal{M} \mid \mu(\mathcal{A}) = 0\}$ be the null set of μ and $M + t\hat{m} \sim \nu(\cdot; t\hat{m})$. We have two scenarios listed as follows.

- (i) $\mathcal{N}_\mu = \mathcal{N}_{\nu(\cdot; t\hat{m})}$ for all $t > 0$ if and only if $\hat{m} \in \mathcal{H}_\mu$, i.e., the null sets are shift invariant.
- (ii) There exists a set $\mathcal{E}_t \subset \mathcal{M}$ such that $\mu(\mathcal{E}_t) = 0$ and $\nu(\mathcal{E}_t; t\hat{m}) = 1$ for all $t > 0$ and $\hat{m} \in \mathcal{M} \setminus \mathcal{H}_\mu$, i.e., the shifted distributions have disjoint probability concentration.

Due to (1), the term $\mathcal{G}(M + t\hat{m})$ is well-defined a.s. for all $t > 0$ and $\hat{m} \in \mathcal{H}_\mu$, thus the limiting sequence within the stochastic derivative definition is well-defined. Due to (2), $M + t\hat{m} \in \mathcal{E}_t$ a.s. for $\hat{m} \in \mathcal{M} \setminus \mathcal{H}_\mu$, in which case $\mathcal{G}(M + t\hat{m})$ is ill-defined and the limiting sequence within the Gâteaux derivative definition is ill-defined. \square

Appendix B. The gradient and the Gauss–Newton Hessian of the data misfit

In this section, we show the connection of our definition of the ppGNH \mathcal{H} defined in (6) and the ppg $D_{\mathcal{H}_\mu}\Phi^y(m)$ in (5) to the conventional definitions. Assume the Gâteaux derivative $D\mathcal{G}(m)$ exists, then the following relation holds μ -a.e.

$$D_{\mathcal{H}_\mu}\mathcal{G}(m) = D\mathcal{G}(m)|_{\mathcal{H}_\mu}, \quad D_{\mathcal{H}_\mu}\mathcal{G}(m)^* = \mathcal{C}_{\text{pr}} D\mathcal{G}(m)^* \mathbf{C}_n^{-1}. \quad (\text{B.1})$$

We have the following \mathcal{M} -Riesz representation of the gradient, i.e., Gâteaux derivative of the data misfit:

$$D\Phi^y(m) := D\mathcal{G}(m)^* \mathbf{C}_n^{-1}(\mathcal{G}(m) - \mathbf{y}).$$

By the definition of the ppg and (B.1)

$$D_{\mathcal{H}_\mu}\Phi^y(m) := \mathcal{C}_{\text{pr}} D\Phi^y(m) \implies D_{\mathcal{H}_\mu}\Phi^y(m) := D_{\mathcal{H}_\mu}\mathcal{G}(m)^*(\mathcal{G}(m) - \mathbf{y}).$$

We now show that $D_{\mathcal{H}_\mu}\Phi^y(m)$ is indeed the \mathcal{H}_μ -Riesz representation of the data misfit stochastic derivative. Suppose the stochastic derivative of the data misfit is given by $\mathcal{T} \in \mathcal{H}'_\mu$, where \mathcal{H}'_μ is the dual space of \mathcal{H}_μ . By the chain rule, for all $\delta m \in \mathcal{H}_\mu$ we have

$$\begin{aligned} \mathcal{T}(m)\delta m &= (D_{\mathcal{H}_\mu}\mathcal{G}(m)\delta m)^T \mathbf{C}_n^{-1}(\mathcal{G}(m) - \mathbf{y}) && \text{(Chain rule)} \\ &= \langle D_{\mathcal{H}_\mu}\mathcal{G}(m)^*(\mathcal{G}(m) - \mathbf{y}), \delta m \rangle_{\mathcal{C}_{\text{pr}}^{-1}} && \text{(Definition of adjoint on } \text{HS}(\mathcal{H}_\mu, \mathcal{Y})\text{)} \\ &= \langle D_{\mathcal{H}_\mu}\Phi^y(m), \delta m \rangle_{\mathcal{C}_{\text{pr}}^{-1}}. \end{aligned}$$

Therefore, our definition of the ppg is identical to the conventional definition. Similarly, we have the following definition of the Gauss–Newton Hessian using the Gâteaux derivative:

$$\mathcal{H}_{\text{GN}}(m) := D\mathcal{G}(m) \mathbf{C}_n^{-1} D\mathcal{G}(m). \quad (\text{Gauss–Newton Hessian})$$

By the definition of the ppGNH and (B.1), we have

$$\mathcal{H}(m) := \mathcal{C}_{\text{pr}} \mathcal{H}_{\text{GN}}(m) \implies \mathcal{H}(m) := D_{\mathcal{H}_\mu}\mathcal{G}(m)^* D_{\mathcal{H}_\mu}\mathcal{G}(m).$$

To see that $\mathcal{H}(m)$ is the Gauss–Newton Hessian under the stochastic derivative assumption, notice that the stochastic Hessian of the data misfit $D_{\mathcal{H}_\mu}^2\Phi^y(m) \in \text{HS}(\mathcal{H}_\mu)$ is given by

$$D_{\mathcal{H}_\mu}^2\Phi^y(m)\delta m := \left(D_{\mathcal{H}_\mu}^2\mathcal{G}(m)\delta m \right)^* (\mathcal{G}(m) - \mathbf{y}) + \mathcal{H}(m)\delta m \quad \forall \delta m \in \mathcal{H}_\mu, \quad (\text{B.2})$$

where $D_{\mathcal{H}_\mu}^2\mathcal{G}(m) \in \text{HS}(\mathcal{H}_\mu, \text{HS}(\mathcal{H}_\mu, \mathcal{Y}))$ is the stochastic Hessian of the forward operator. Assuming the data misfit term is relatively small in regions with high posterior probability, one may drop the term involving the Hessian of the PtO map and still retain a reasonable approximation to the data misfit Hessian. This makes the ppGNH \mathcal{H} an approximation to the stochastic Hessian of the data misfit.

Appendix C. Bounding constant and proofs of [Propositions 4.1 and 4.2](#)

The bounding constant in (25) is given by

$$c_{\text{misfit}}(\mathcal{G}, \tilde{\mathcal{G}}, \mathbf{y}, \mathbf{C}_n^{-1}\mu) = \left\| \exp(-\widetilde{\Phi^y}(\cdot)) \right\|_{L_\mu^\infty(\mathcal{M})} \left\| \frac{1}{2} (\mathcal{G}(\cdot) + \tilde{\mathcal{G}}(\cdot)) - \mathbf{y} \right\|_{L_\mu^2(\mathcal{M}; \mathcal{Y})}.$$

Proof of Proposition 4.1. We may decompose the operator surrogate approximation error into two parts using a triangle inequality:

$$\|\mathcal{G} - \tilde{\mathcal{G}}\|_{L^2_\mu(\mathcal{M}; \mathcal{Y})} \leq \|\mathcal{G} - \mathcal{G}_r\|_{L^2_\mu(\mathcal{M}; \mathcal{Y})} + \|\mathcal{G}_r - \tilde{\mathcal{G}}\|_{L^2_\mu(\mathcal{M}; \mathcal{Y})}.$$

We examine the second term on the right-hand side of the inequality. First, we have $\Psi_r^* M \sim \mathcal{N}(\mathbf{0}, \mathbf{I}_r)$ for any linear encoder Ψ_r^* defined as in (20); see (D.1). Second, notice that $\mathcal{G}_r(m) = \mathcal{G}_r(\widehat{\Psi_r^*} \widehat{\Psi_r^*}^* m)$. Consequently, the neural network error is given by

$$\begin{aligned} \|\tilde{\mathcal{G}} - \mathcal{G}_r\|_{L^2_\mu(\mathcal{M}; \mathcal{Y})}^2 &= \mathbb{E}_{\mathbf{M}_r \sim \mathcal{N}(\mathbf{0}, \mathbf{I}_r)} \left[\left\| \mathbf{V} \mathbf{f}_{\text{NN}}(\mathbf{M}_r) - \mathcal{G}_r \left(\widehat{\Psi_r^*} \mathbf{M}_r \right) \right\|_{\mathbf{C}_n^{-1}}^2 \right] \\ &= \mathbb{E}_{\mathbf{M}_r \sim \mathcal{N}(\mathbf{0}, \mathbf{I}_r)} \left[\left\| \mathbf{f}_{\text{NN}}(\mathbf{M}_r) - \mathbf{V}^* \mathcal{G}_r \left(\widehat{\Psi_r^*} \mathbf{M}_r \right) \right\|^2 \right]. \end{aligned}$$

We further decompose the first term on the right-hand side of the triangle inequality.

- **Part I: Subspace Poincaré inequality.** We apply [65, Propositions 2.4] to our setting. Due to the Poincaré inequality for H_μ^1 (Theorem 3.2 and [59, 5.5.6]), for any $\mathcal{S} \in H_\mu^1(\mathcal{M}) := H_\mu^1(\mathcal{M}; \mathbb{R})$ and any pair of encoder Ψ_r^* and decoder Ψ_r as defined in (20), we have:

$$\|\mathcal{S} - \mathcal{S}_r\|_{L^2_\mu(\mathcal{M})}^2 \leq \|(\mathcal{I}_{\mathcal{H}_\mu} - \Psi_r \Psi_r^*) D_{\mathcal{H}_\mu} \mathcal{S}\|_{L^2_\mu(\mathcal{M}; \mathcal{H}_\mu)}^2,$$

where \mathcal{S}_r is the $L^2_\mu(\mathcal{M})$ -optimal reduced mapping of \mathcal{S} for the given encoder and decoder, $D_{\mathcal{H}_\mu} \mathcal{S} \in L^2_\mu(\mathcal{M}; \mathcal{H}_\mu)$ is the \mathcal{H}_μ -representation of the stochastic derivative of \mathcal{S} . The key to extend [65, Propositions 2.4] is to show that the mapping for any $m' \in \mathcal{M}$

$$f : m \mapsto \mathcal{S}(\Psi_r \Psi_r^* m' + (\mathcal{I}_{\mathcal{M}} - \Psi_r \Psi_r^*) m)$$

has a stochastic derivative of the following form via the chain rule:

$$D_{\mathcal{H}_\mu} f(m) = (\mathcal{I}_{\mathcal{H}_\mu} - \Psi_r \Psi_r^*) D_{\mathcal{H}_\mu} \mathcal{S}(\Psi_r \Psi_r^* m' + (\mathcal{I}_{\mathcal{M}} - \Psi_r \Psi_r^*) m).$$

The $H_\mu^1(\mathcal{M})$ -Poincaré inequality is applied to f , which leads to the subspace Poincaré inequality

- **Part II: Error upper bound** We apply [65, Proposition 2.5] to our setting. Due to the subspace Poincaré inequality, for any pair of encoder Ψ_r^* and decoder Ψ_r as defined by (20), we have

$$\|\mathcal{G} - \mathcal{G}_r\|_{L^2_\mu(\mathcal{M}; \mathcal{Y})}^2 \leq \text{Tr}_{\mathcal{H}_\mu}(\mathcal{H}_A) - \text{Tr}(\Psi_r^* \mathcal{H}_A \Psi_r).$$

where \mathcal{G}_r is the $L^2_\mu(\mathcal{M}; \mathcal{Y})$ -optimal reduced mapping for the given Ψ_r^* and Ψ_r . The key to extend [65, Proposition 2.5] is to define $\mathcal{S}^{(j)} := \mathbf{v}_j^T \mathbf{C}_n^{-1} \mathcal{G}$ where $\{\mathbf{v}_j\}_{j=1}^{d_y}$ is a \mathcal{Y} -ONB.

$$\|\mathcal{G} - \mathcal{G}_r\|_{L^2_\mu(\mathcal{M}; \mathcal{Y})}^2 = \sum_{j=1}^{d_y} \left\| \mathcal{S}^{(j)} - \mathcal{S}_r^{(j)} \right\|_{L^2_\mu(\mathcal{M})}^2.$$

Applying the subspace inequality to \mathcal{S}^j and the transformation between trace and HS norm [63, Theorem 7.4], we have

$$\begin{aligned} \|\mathcal{G} - \mathcal{G}_r\|_{L^2_\mu(\mathcal{M}; \mathcal{Y})}^2 &\leq \sum_{j=1}^{d_y} \text{Tr}_{\mathcal{H}_\mu} \left((\mathcal{I}_{\mathcal{H}_\mu} - \Psi_r \Psi_r^*) \mathbb{E}_{M \sim \mu} \left[D_{\mathcal{H}_\mu} \mathcal{G}^* \mathbf{v}_j \mathbf{v}_j^T \mathbf{C}_n^{-1} D_{\mathcal{H}_\mu} \mathcal{G} \right] (\mathcal{I}_{\mathcal{H}_\mu} - \Psi_r \Psi_r^*) \right) \\ &= \text{Tr}_{\mathcal{H}_\mu} \left((\mathcal{I}_{\mathcal{H}_\mu} - \Psi_r \Psi_r^*) \mathcal{H}_A (\mathcal{I}_{\mathcal{H}_\mu} - \Psi_r \Psi_r^*) \right). \end{aligned} \tag{C.1}$$

- **Part III: Sampling error.** We follow a line of arguments presented in [89]. Let $\{\lambda_j^{\text{DIS}} \in \mathbb{R}_+, \psi_j^{\text{DIS}} \in \mathcal{H}_\mu\}_{j=1}^\infty$ and $\{\widehat{\lambda}_j^{\text{DIS}} \in \mathbb{R}_+, \widehat{\psi}_j^{\text{DIS}} \in \mathcal{H}_\mu\}_{j=1}^\infty$ denote the eigendecompositions of $\mathcal{H}_A := \mathbb{E}_{M \sim \mu}[\mathcal{H}(m)]$ and $\widehat{\mathcal{H}}$ with decreasing eigenvalues and \mathcal{H}_μ -orthonormal basis. Let $\Psi_r^{\text{DIS}}, \widehat{\Psi}_r^{\text{DIS}} \in \text{HS}(\mathbb{R}^r, \mathcal{H}_\mu)$ be the linear decoder defined using the first r eigenbases. Then, we can deduce the optimal low-rank approximation of \mathcal{H}_A and $\widehat{\mathcal{H}}$ using the Courant min–max principle:

$$\Psi_r^{\text{DIS}} \in \arg \max_{\substack{\mathcal{U}_r \in \text{HS}(\mathbb{R}^r, \mathcal{H}_\mu) \\ \mathcal{U}_r^* \mathcal{U}_r = \mathbf{I}_r}} \text{Tr}(\mathcal{U}_r^* \mathcal{H}_A \mathcal{U}_r), \quad \widehat{\Psi}_r^{\text{DIS}} \in \arg \max_{\substack{\mathcal{U}_r \in \text{HS}(\mathbb{R}^r, \mathcal{H}_\mu) \\ \mathcal{U}_r^* \mathcal{U}_r = \mathbf{I}_r}} \text{Tr}(\mathcal{U}_r^* \widehat{\mathcal{H}} \mathcal{U}_r).$$

Assume $\widehat{\mathcal{H}} - \mathcal{H}$ can be decomposed to $\mathcal{V} \mathcal{D} \mathcal{V}^*$, where $\mathcal{V} \in \text{HS}(\mathbb{R}^r, \mathcal{H}_\mu)$ has columns consisting of \mathcal{H}_μ -orthonormal eigenbases and $\mathcal{D} \in \mathbb{R}^r$ consists of eigenvalues, the cyclic property of trace leads to

$$\text{Tr}(\mathcal{U}_r^* (\widehat{\mathcal{H}} - \mathcal{H}_A) \mathcal{U}_r) = \text{Tr}(\mathcal{U}_r^* \mathcal{V} \mathcal{D} \mathcal{V}^* \mathcal{U}_r) \leq \left\| \mathcal{H} - \widehat{\mathcal{H}} \right\|_{B(\mathcal{H}_\mu)} \text{Tr}_{\mathcal{H}_\mu}(\mathcal{V}^* \mathcal{U}_r \mathcal{U}_r^* \mathcal{V}) = r \left\| \mathcal{H}_A - \widehat{\mathcal{H}} \right\|_{B(\mathcal{H}_\mu)},$$

where $\mathcal{U}_r \in \text{HS}(\mathbb{R}^r, \mathcal{H}_\mu)$ is arbitrary and has columns consisting of \mathcal{H}_μ -orthonormal reduced bases. Applying the inequality above twice, we have the following upper bound of the approximation error to the optimal reduced mapping given the pair of decoder and encoder $\widehat{\Psi}_r^{\text{DIS}}$ and $\widehat{\Psi}_r^{\text{DIS}}{}^*$:

$$\begin{aligned} \|\mathcal{G} - \mathcal{G}_r\|_{L_\mu^2(\mathcal{M}; \mathcal{Y})}^2 &\leq \text{Tr}_{\mathcal{H}_\mu}(\mathcal{H}_A) - \text{Tr}(\widehat{\Psi}_r^{\text{DIS}}{}^* \mathcal{H}_A \widehat{\Psi}_r^{\text{DIS}}) \\ &\leq \text{Tr}_{\mathcal{H}_\mu}(\mathcal{H}_A) - \text{Tr}(\Psi_r^{\text{DIS}} \mathcal{H}_A (\Psi_r^{\text{DIS}})^*) + 2r \left\| \mathcal{H}_A - \widehat{\mathcal{H}} \right\|_{B(\mathcal{H}_\mu)} \\ &= \sum_{j=r+1}^{\infty} \lambda_j^{\text{DIS}} + 2r \left\| \mathcal{H}_A - \widehat{\mathcal{H}} \right\|_{B(\mathcal{H}_\mu)}. \end{aligned}$$

□

Proof of Proposition 4.2. We follow the same arguments in [65, Porposition 3.1]. From (C.1) and the definition of KLE, the approximation error for the optimal reduced mapping defined by the KLE reduced bases $\Psi_r^{\text{KLE}} \in \text{HS}(\mathbb{R}^r, \mathcal{H}_\mu)$ is given by

$$\begin{aligned} \|\mathcal{G} - \mathcal{G}_r\|_{L_\mu^2(\mathcal{M}; \mathcal{Y})}^2 &\leq \text{Tr}_{\mathcal{H}_\mu} \left((\mathcal{I}_{\mathcal{H}_\mu} - \Psi_r^{\text{KLE}} \Psi_r^{\text{KLE}}{}^*) \mathcal{H}_A (\mathcal{I}_{\mathcal{H}_\mu} - \Psi_r^{\text{KLE}} \Psi_r^{\text{KLE}}{}^*) \right) \\ &\leq \|\mathcal{H}_A\|_{B(\mathcal{H}_\mu)} \mathbb{E}_{M \sim \mu} \left[\left\| (\mathcal{I}_{\mathcal{M}} - \Psi_r^{\text{KLE}} \Psi_r^{\text{KLE}}{}^*) M \right\|_{\mathcal{M}}^2 \right] \\ &= \|\mathcal{H}_A\|_{B(\mathcal{H}_\mu)} \sum_{j=r+1}^{\infty} (\lambda_j^{\text{KLE}})^2. \end{aligned}$$

By Assumption 4, we have the following bound μ -a.e.

$$\|D_{\mathcal{H}_\mu} \mathcal{G}(m)\|_{B(\mathcal{H}, \mathcal{Y})} \leq \sup_{\substack{\delta m \in \mathcal{H}_\mu \\ \|\delta m\|_{\mathcal{H}_\mu} = 1}} \lim_{t \rightarrow 0} \|t^{-1} (\mathcal{G}(m + t\delta m) - \mathcal{G}(m))\|_{C_n^{-1}} \leq c_{\mathcal{G}}.$$

Thus we have

$$\|\mathcal{H}_A\|_{B(\mathcal{H}_\mu)} = \sup_{\substack{\delta m \in \mathcal{H}_\mu \\ \|\delta m\|_{\mathcal{H}_\mu} = 1}} \mathbb{E}_{M \sim \mu} \left[\|D_{\mathcal{H}_\mu} \mathcal{G}(M) \delta m\|_{C_n^{-1}}^2 \right] \leq c_{\mathcal{G}}^2.$$

Due to (C.1), the minimized upper bound is achieved when $\Psi_r = \Psi_r^{\text{DIS}}$. Therefore, we have

$$\sum_{j=r+1}^{\infty} \lambda_j^{\text{DIS}} \leq \|\mathcal{H}_A\|_{B(\mathcal{H}_\mu)} \sum_{j=r+1}^{\infty} (\lambda_j^{\text{KLE}})^2 \leq c_{\mathcal{G}}^2 \sum_{j=r+1}^{\infty} (\lambda_j^{\text{KLE}})^2.$$

□

Appendix D. Proofs of Lemma 5.1 and Proposition 5.2

Proof of Lemma 5.1. The statement on the transformation of Gaussian random elements is standard; see [90, Proposition 1.2.3]. Since the \mathcal{M} -adjoint of Ψ_r^* is $\mathcal{C}_{\text{pr}}^{-1}\Psi_r$, we have

$$\Psi^*M \sim \mathcal{N}(0, \Psi^*\mathcal{C}_{\text{pr}}\mathcal{C}_{\text{pr}}^{-1}\Psi_r) = \mathcal{N}(0, \mathbf{I}_r). \quad (\text{D.1})$$

We focus on the statement on the independence of two random elements $M_r \perp M_\perp$ given by:

$$\begin{cases} M_r = \Psi_r\Psi_r^*M \\ M_\perp := (\mathcal{I}_{\mathcal{M}} - \Psi_r\Psi_r^*)M \end{cases}, \quad M \sim \mu.$$

We examine the characteristic function for the joint random element $X = (M_r, M_\perp)$ and equip the product space $\mathcal{M} \times \mathcal{M}$ with an extended inner product:

$$\langle (t_r, t_\perp), (s_r, s_\perp) \rangle_{\mathcal{M} \times \mathcal{M}} = \langle t_r, s_r \rangle_{\mathcal{M}} + \langle t_\perp, s_\perp \rangle_{\mathcal{M}}.$$

We have the following form for the characteristic function of X :

$$\begin{aligned} \phi_X(t) &= \mathbb{E}_{M \sim \mu} [\exp(i \langle \Psi_r\Psi_r^*M, t_r \rangle_{\mathcal{M}}) \exp(i \langle (\mathcal{I}_{\mathcal{M}} - \Psi_r\Psi_r^*)M, t_\perp \rangle_{\mathcal{M}})] \\ &= \mathbb{E}_{M \sim \mu} [\exp(i \langle M, (\Psi_r\Psi_r^*)^*(t_r - t_\perp) + t_\perp \rangle_{\mathcal{M}})] \quad (\text{Def. of } \mathcal{M}\text{-adjoint}) \\ &= \exp(\langle \mathcal{C}_{\text{pr}}((\Psi_r\Psi_r^*)^*(t_r - t_\perp) + t_\perp), (\Psi_r\Psi_r^*)^*(t_r - t_\perp) + t_\perp \rangle_{\mathcal{M}}) \quad (\text{Def. of } \phi_M) \\ &= \exp(\langle \Psi_r\Psi_r^*\mathcal{C}_{\text{pr}}(t_r - t_\perp) + \mathcal{C}_{\text{pr}}t_\perp, (\Psi_r\Psi_r^*)^*(t_r - t_\perp) + t_\perp \rangle_{\mathcal{M}}) \quad (\text{Explicit } \mathcal{M}\text{-adjoint}) \\ &= \exp(\langle \Psi_r\Psi_r^*\mathcal{C}_{\text{pr}}t_r, t_r \rangle_{\mathcal{M}}) \exp(\langle (\mathcal{I}_{\mathcal{M}} - \Psi_r\Psi_r^*)\mathcal{C}_{\text{pr}}t_\perp, t_\perp \rangle_{\mathcal{M}}) \quad (\text{Cancel cross terms}) \end{aligned}$$

Therefore, by the definition of the characteristic function for Gaussian measures we have

$$X \sim \mathcal{N}\left(\mathbf{0}, \begin{bmatrix} \Psi_r\Psi_r^*\mathcal{C}_{\text{pr}} & 0 \\ 0 & (\mathcal{I}_{\mathcal{M}} - \Psi_r\Psi_r^*)\mathcal{C}_{\text{pr}} \end{bmatrix}\right),$$

and thus M_r and M_\perp are independently distributed. \square

Proof of Proposition 5.2. We show that the surrogate mMALA proposal $\widetilde{\mathcal{Q}_{\text{mMALA}}}(m, \cdot)$ at a given m can be defined through deterministic transformation of the prior following Lemma 5.1. Consider $\widetilde{\mathcal{T}}(m) \in B(\mathcal{M})$ given by

$$\widetilde{\mathcal{T}}(m) = \mathcal{I}_{\mathcal{M}} + \widetilde{\Psi}_r \left(\left((\widetilde{d}_j + 1)^{1/2} - 1 \right) \delta_{jk} \right) \widetilde{\Psi}_r^*,$$

where $\widetilde{\Psi}_r$, $\widetilde{\Psi}_r^*$, and \widetilde{d}_j are defined in Section 5.2. The covariance of the local Gaussian approximation of the posterior in (32) can be expressed as

$$\widetilde{\mathcal{C}_{\text{post}}}(m) = \widetilde{\mathcal{T}}(m)\mathcal{C}_{\text{pr}}\widetilde{\mathcal{T}}(m)^*. \quad (\text{D.2})$$

The key to validating (D.2) is to take the adjoint of $\widetilde{\Psi}_r$ and $\widetilde{\Psi}_r^*$ in \mathcal{M} when taking the adjoint of $\mathcal{T}(m)$. In particular, the \mathcal{M} -adjoint of $\widetilde{\mathcal{T}}(m)$ is given by

$$\widetilde{\mathcal{T}}(m)^* = \mathcal{I}_{\mathcal{M}} + \mathcal{C}_{\text{pr}}^{-1}\widetilde{\Psi}_r \left(\left((\widetilde{d}_j + 1)^{1/2} - 1 \right) \delta_{jk} \right) \widetilde{\Psi}_r^* \mathcal{C}_{\text{pr}}.$$

The covariance transformation given by $\widetilde{\mathcal{T}}(m)$ leads to

$$M^\dagger \sim \widetilde{\mathcal{Q}_{\text{mMALA}}}(m, \cdot) \quad \text{and} \quad M^\dagger = sm + (1 - s)\widetilde{\mathcal{A}}(m) + \sqrt{1 - s^2}\widetilde{\mathcal{T}}(m)M, \quad M \sim \mu.$$

Since the M can be independently decomposed into two parts using the encoder Ψ_r^* and decoder Ψ_r due to Lemma 5.1, the proposal distribution can also be decomposed into two parts independently. \square

Appendix E. Step size tuning and chain initialization

We provide the procedure for determining the step size parameter Δt for a given Bayesian inverse problem. The procedure is consistent across all MCMC algorithms in [Tables 2](#) and [3](#) and is designed to maximize the sampling performance of MCMC methods while maintaining uniform behaviors of the MCMC chain across different regions of the parameter space.

First, we choose a list of candidate values for Δt . Then, we generate an MCMC chain $\{m_j\}_{j=1}^{n_s}$ with $n_s = 5000$ samples (after burn-in) for each candidate value. Using these samples, we compute the acceptance rate (AR) and the mean square jump (MSJ) given by

$$\text{AR} := \frac{n_{\text{accept}}}{n_s} \times 100\%, \quad \text{MSJ} := \frac{1}{n_s - 1} \sum_{j=1}^{n_s-1} \|m_{j+1} - m_j\|_{\mathcal{M}}^2,$$

where n_{accept} is the number of accepted proposal samples in the MCMC chain. We down-select the candidate values by choosing a maximum step size $\Delta t_{\max} > 0$ such that AR monotonically decreases and MSJ monotonically increases as a function of $\Delta t \in [0, \Delta t_{\max}]$. Finally, we choose a tuned step size value from the remaining candidates that maximize the median of the single chain version of the ESS% in [\(40\)](#).

To make the step size tuning more efficient, we initialize the chains with samples from the Laplace approximation to reduce the number of burn-in samples. Once the step size tuning is complete, we initialize the subsequent MCMC runs using samples obtained from step size tuning.

Remark 5. *Due to the high non-linearity of Bayesian inversion in our numerical examples, the step size tuning procedure introduced above is often ineffective for MALA and LA-pCN. In particular, the ARs for MCMC chains initialized at different positions have large variations when the tuned step size is employed. In such cases, the MCMC chains are often stuck in local regions with low ARs; see [Figure E.18](#). We reduce the step size to eliminate this behavior until the AR variations are within $\pm 5\%$ of the averaged value.*

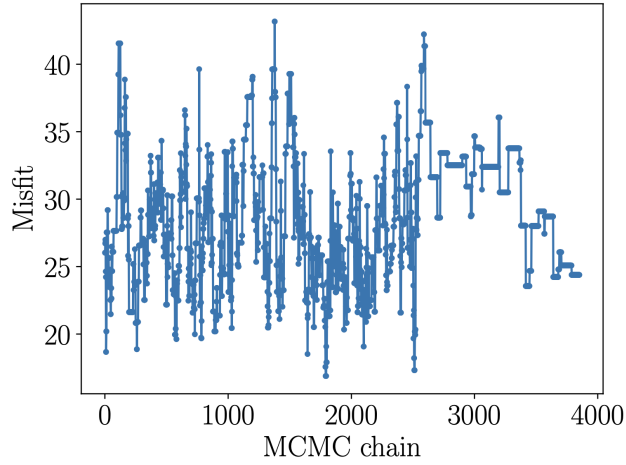


Figure E.18: The trace plot of data misfit values along a Markov chain generated by LA-pCN at large step size for inferring log-diffusivity in nonlinear diffusion–reaction PDE. The Markov chain behaves drastically differently in different parts of the chain, leading to a large bias in posterior estimation.

Appendix F. Supplementary materials for the numerical examples

In [Figure F.19](#), we visualize selected DIS and KLE basis functions for coefficient inversion in nonlinear diffusion–reaction PDE. In [Table F.6](#), we list the statistics for the MCMC runs. In [Figure F.20](#), we visualize

the posterior samples, mean estimate via MCMC using mMALA, the absolute error between MAP estimate and mean estimate, pointwise variance estimate via MCMC using mMALA, and the absolute error of pointwise variance estimate from LA and MCMC. The same visualization and statistics for hyperelastic material deformation is provided in [Figures F.21](#) and [F.22](#) and [Table F.7](#). We emphasize that the large error between the MCMC mean estimate and the MAP estimate indicates a non-Gaussian posterior distribution.

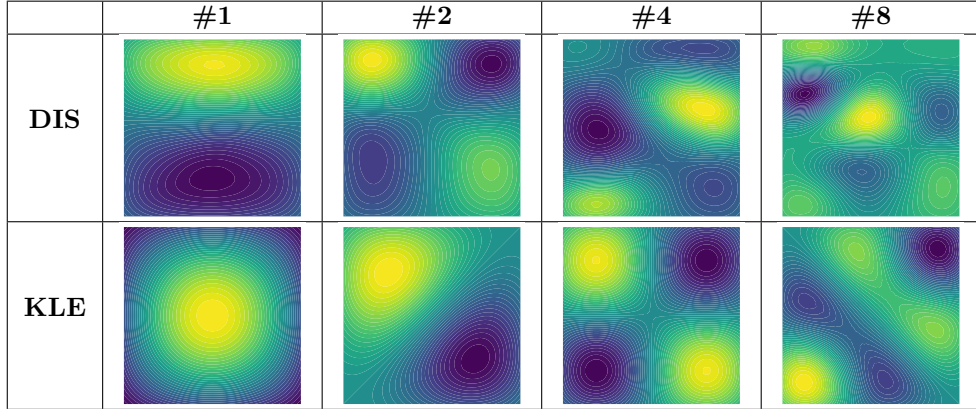


Figure F.19: Visualization of selected DIS and KLE basis functions for coefficient inversion in nonlinear diffusion–reaction PDE in [Section 7](#)

Name	Step size $\Delta t \times 10^{-2}$	Acceptance rate %	Mean square jump $\times 10^{-3}$
pCN	1	16	1
MALA	0.36	39	0.96
LA-pCN	2.3	60	6.0
DIS-mMALA	11	44	11
mMALA	15	20	12
NO-mMALA $n_t = 16 \times 10^3$	1.8	26	2.1
DINO-mMALA $n_t = (2, 4, 8, 16) \times 10^3$	(12, 12, 13, 15)	(19, 20, 20, 17)	(9.9, 10, 11, 11)
DA-NO-mMALA $n_t = (1, 2, 4, 8, 16) \times 10^3$	(1, 1, 1.3, 1.5, 1.5, 1.8)	1st: (63, 67, 67, 70, 68) 2nd: (11, 23, 28, 27, 35)	(0.23, 0.45, 0.61, 0.87, 1.1)
DA-DINO-mMALA $n_t = (1, 2, 4, 8, 16) \times 10^3$	(11, 11, 12, 13, 14)	1st: (40, 29, 25, 22, 19) 2nd: (42, 57, 67, 72, 76)	(4.6, 6.8, 7.9, 8.7, 9.2)

Table F.6: The statistics of MCMC runs for coefficient inversion in nonlinear diffusion–reaction PDE.

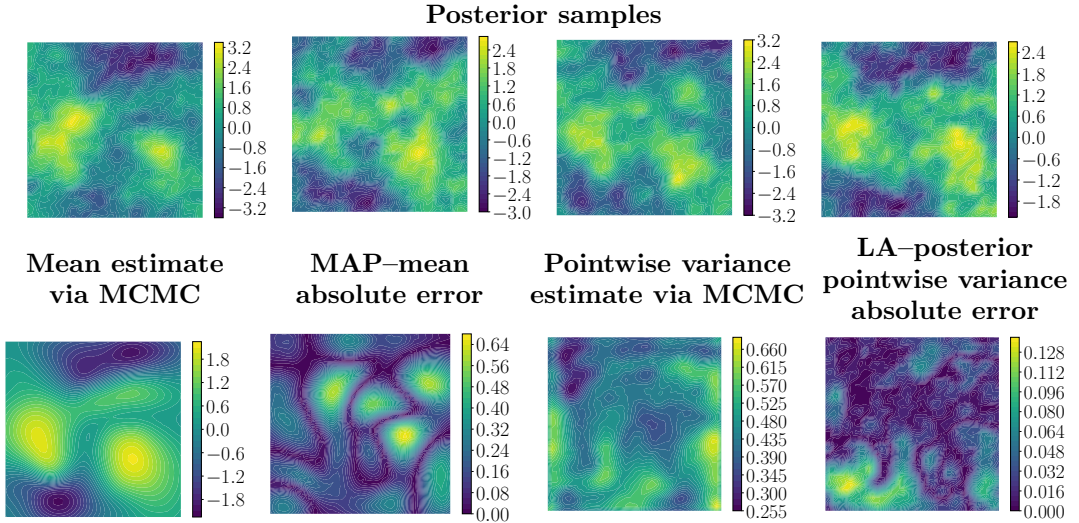


Figure F.20: Visualization of relevant statistics from Markov chains collected using mMALA for coefficient inversion in nonlinear diffusion–reaction PDE. We provide posterior samples, mean estimate via MCMC, the absolute error between MAP estimate and mean estimate via MCMC, pointwise variance estimate via MCMC, the absolute error of pointwise variance estimates from LA and MCMC.

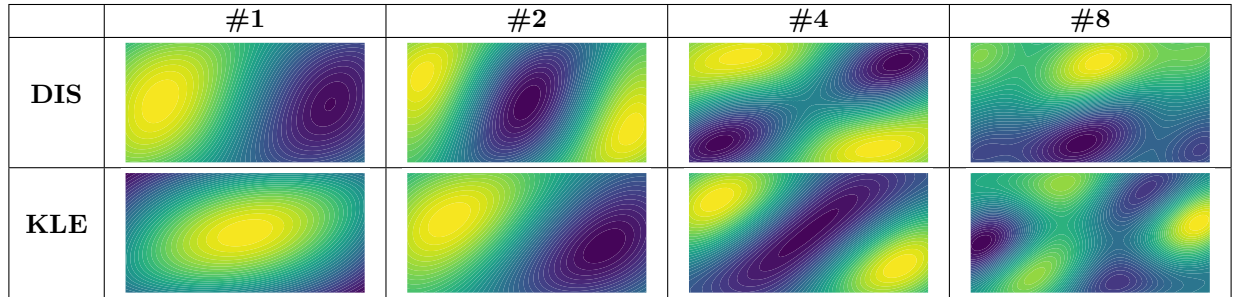


Figure F.21: Visualization of selected DIS and KLE basis functions for hyperelastic material property discovery in [Section 8](#)

Name	Step size $\Delta t \times 10^{-2}$	Acceptance rate %	Mean square jump $\times 10^{-3}$
pCN	1.0	30	0.43
MALA	0.075	78	0.40
LA-pCN	5.0	75	2.6
DIS-mMALA	150	64	26
mMALA	100	34	14
DA-NO-mMALA $n_t = (5, 10, 20, 40) \times 10^2$	(0.5, 1, 2, 4)	1st: (49, 37, 33, 44) 2nd: (41, 41, 46, 68)	(0.12, 0.16, 0.27, 0.90)
DA-DINO-mMALA $n_t = (5, 10, 20, 40) \times 10^2$	(65, 65, 70, 70)	1st: (38, 40, 38, 39) 2nd: (76, 87, 90, 93)	(9.4, 11, 11, 12)

Table F.7: The statistics of MCMC runs for hyperelastic material property discovery.

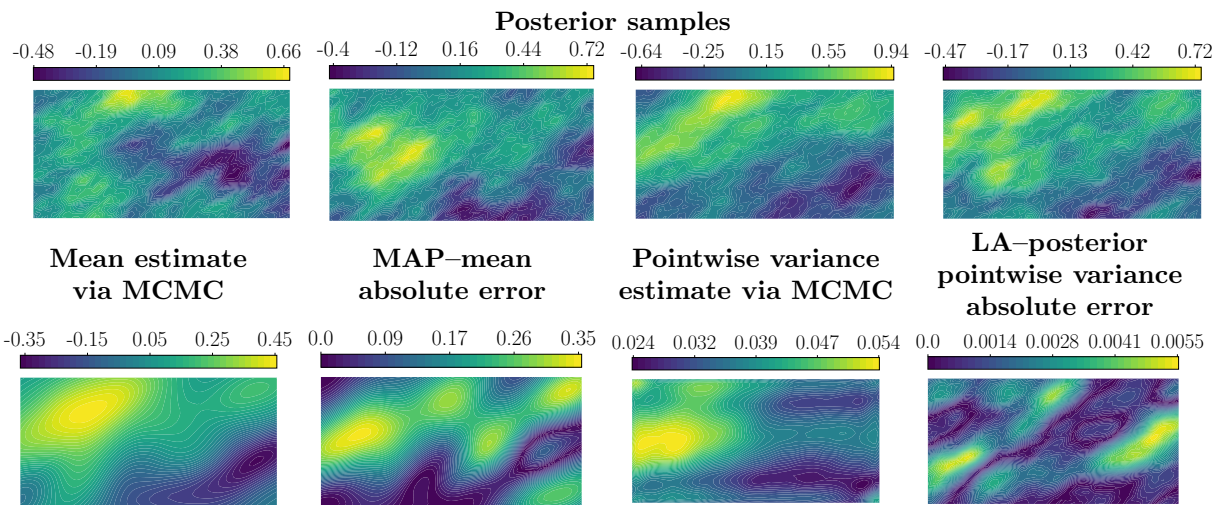


Figure F.22: Visualization of relevant statistics from Markov chains collected using mMALA for hyperelastic material property discovery. We provide posterior samples, mean estimate via MCMC, the absolute error between MAP estimate (37a) and mean estimate via MCMC, pointwise variance estimate via MCMC, the absolute error of pointwise variance estimates from LA (37a) and MCMC.